

---

# Terahertz Electromodulation Spectroscopy on Organic Semiconductors

Philipp Riederer

---



München 2023



---

# Terahertz Electromodulation Spectroscopy on Organic Semiconductors

Philipp Riederer

---

Dissertation  
der Fakultät für Physik  
der Ludwig-Maximilians-Universität  
München

vorgelegt von  
Philipp Riederer  
aus München

München, den 01.08.2023

Erstgutachter: Prof. Dr. Roland Kersting  
Zweitgutachter: Priv.-Doz. Dr. Bert Nickel  
Tag der mündlichen Prüfung: 18.10.2023

*"Physics is not the most important thing. Love is."*

- Richard P. Feynman -



# Zusammenfassung

Die Entdeckung von halbleitenden organischen Materialien eröffnete ein faszinierendes Forschungsgebiet und ebnete den Weg für heute nicht mehr wegzudenkende Entwicklungen. Trotz der Vorteile hinsichtlich günstiger Produktion und vielfältiger Herstellungsmöglichkeiten, sind organische Halbleiter ihren kristallinen Gegenspielern in ihrer Leitfähigkeit unterlegen. Auf die Fragen warum das so ist und welche Mechanismen den Ladungsträgertransport maßgeblich hemmen, können keine eindeutigen Antworten gegeben werden.

Diese Arbeit versucht den Antworten mithilfe der Terahertz (THz) Elektromodulations-Spektroskopie näher zu kommen, denn diese Methode erlaubt einen Einblick in die intrinsischen Transport-Phänomene von molekularen Halbleitern. Hierfür wird zu Beginn der Arbeit der experimentelle Aufbau des THz Spektrometers, die untersuchten Dünnschicht-Strukturen, die Analyse der Elektromodulations-Daten sowie die Vorteile und Grenzen der Technik im Detail erklärt. Es stellt sich heraus, dass sich diese Technik hervorragend dafür eignet, alle heutzutage relevanten organischen Halbleiter-Materialien mit Mobilitäten bis hinab zu  $1 \text{ cm}^2/\text{Vs}$  zu untersuchen. Ein besonderer Fokus dieser Arbeit liegt auf den Einflüssen der Grenzschichten innerhalb der Bauelemente. Wie die Rauigkeit der Isolator-Halbleiter Grenzfläche die Ladungsträgerverteilung im Bauelement bestimmt wird mithilfe von Berechnungen der selbstkonsistenten Poisson Gleichung ermittelt. Schon Rauigkeiten in der Größenordnung von einer molekularen Schicht resultieren in einer drastischen Verringerungen der Leitfähigkeit in dem Halbleiter. Bei der Untersuchung des Einflusses von Gold als Elektrodenmaterial wurde festgestellt, dass Gold-Ionen in Gegenwart eines elektrischen Feldes in den organischen Halbleiter migrieren. Dort agieren die Gold-Ionen als effiziente Loch-Fallen, was die Stabilität des Bauteils drastisch reduziert. Der Migrationsprozess ist thermisch aktiviert, teilweise umkehrbar und kann komplett umgangen werden, wenn man anstatt Gold Molybdänoxid verwendet. Die daraus resultierende verbesserte Stabilität der Bauelemente ist eine absolut notwendige Voraussetzung für aussagekräftige frequenz aufgelöste THz Spektroskopie. Temperaturabhängige und frequenz aufgelöste Messungen an DBTTT Strukturen zeigen, dass weder Phonon-Streuung noch dynamische Lokalisierung die limitierenden Mechanismen der Leitfähigkeit sind. Es stellt sich heraus, dass nur ein Teil der injizierten Ladungsträger zum Bandtransport beiträgt. Der Großteil der Ladungsträger ist nicht mobil oder bewegt sich mit dem langsamen Hüpf-Transport.

Insgesamt zeigt diese Arbeit, dass die THz Elektromodulations-Spektroskopie ein einzigartiges und fähiges Werkzeug ist, um organische Dünnschichten zu untersuchen. Außerdem unterstreicht sie, wie wichtig der Einfluss von Grenzflächenphänomenen innerhalb organischer Bauelemente auf den Ladungsträgertransport ist.



# Abstract

The discovery of semiconducting organic materials opened a new fascinating field of research and paved the way for exciting developments. Besides the benefits of cheap fabrication and variable processing possibilities, organic semiconductors still exhibit worse performance in comparison to their crystalline counterparts. The corresponding questions "Why?" and "What mechanisms limit charge transport within organic electronic devices?" cannot be answered unambiguously.

Within this work, the technique of terahertz (THz) electromodulation spectroscopy is used to gather unprecedented insight into the intrinsic charge transport mechanisms of molecular semiconducting thin-film devices. Therefore, the experimental THz spectroscopy setup, the investigated thin-film devices, the electromodulation data analysis methodology as well as advantages and limitations of the technique are presented in detail. It is shown, that this method is a powerful tool for most of today's relevant organic materials as its sensitivity allows the detection of mobilities as low as  $1 \text{ cm}^2/\text{Vs}$ . Furthermore, relevant interfaces within the field-effect devices are systematically investigated. The impact of the roughness of the insulator-semiconductor interface on the charge carrier distribution is inspected by combining two-dimensional atomic force microscopy scans with three-dimensional self-consistent Poisson calculations as this cannot be solely addressed by experimental means. It is found that the majority of charge carriers accumulates near the insulator interface. Thus, roughness in the order of already one molecular monolayer leads to a severe reduction in conductivity. Additionally, it is shown that charge carriers rarely undergo thermally activated hopping but travel within two-dimensional percolation pathways. Moreover, the influence of gold as top contact material is examined by THz spectroscopy. In presence of an applied bias, gold ions migrate into the devices accumulation channel and act as efficient hole traps. This phenomenon is found to be thermally-activated, partially reversible and can be circumvented by exchanging the gold with molybdenum oxide. The resulting devices exhibit long-term stability, which is crucial for frequency-resolved THz spectroscopy investigations. Field-effect devices with the small molecule semiconductor DBTTT are investigated using temperature-dependent and frequency-resolved THz electromodulation spectroscopy. Results show that neither phonon scattering nor dynamic localization are the main limiting mechanisms. It is found, that only a fraction of the injected charge carriers contribute to band transport while the vast majority is immobile or performs hopping transport.

This work highlights the applicability of THz electromodulation spectroscopy as a unique and powerful tool for the investigation of organic thin-film devices and emphasizes the importance of interface phenomena on the intrinsic charge transport within molecular semiconductors.



# Publications

- P. Riederer, M. Bouraoui and R. Kersting: Impact of surface roughness on conduction in molecular semiconductors. *Appl. Phys. Lett.* **120**, 112103 (2022).  
DOI: 10.1063/5.0085778
- P. Riederer, M. Bouraoui and R. Kersting: Field-induced migration of gold in molecular semiconductors. *Appl. Phys. Lett.* **120**, 243503 (2022).  
DOI: 10.1063/5.0092224
- P. Riederer and R. Kersting: Terahertz Electromodulation Spectroscopy for Characterizing Electronic Transport in Organic Semiconductor Thin Films. *J. Infrared Millim. Terahertz Waves* (2022).  
DOI: 10.1007/s10762-022-00893-z
- P. Riederer, F. Devaux, G. Schweicher, Y. H. Geerts and R. Kersting: Molecular semiconductors and the Ioffe–Regel criterion: A terahertz study on band transport in DBTTT. *Appl. Phys. Lett.* **123**, 032103 (2023).  
DOI: 10.1063/5.0153710



# Contents

<b>Zusammenfassung</b>	<b>vii</b>
<b>Abstract</b>	<b>ix</b>
<b>Publications</b>	<b>xi</b>
<b>1 Introduction</b>	<b>1</b>
<b>2 Theoretical Background</b>	<b>3</b>
2.1 Introduction to Terahertz Spectroscopy . . . . .	3
2.1.1 Generation of Terahertz-Pulses . . . . .	4
2.1.2 Detection of Terahertz-Pulses . . . . .	6
2.2 Charge Transport in Organic Semiconductors . . . . .	8
2.2.1 Molecular Organic Semiconductors . . . . .	9
2.2.2 Charge Transport Mechanisms . . . . .	11
2.2.3 Charge Transport Models . . . . .	12
2.3 Charge Distribution Calculation . . . . .	16
2.3.1 Poisson Equation & Fermi-Dirac Statistics . . . . .	17
2.3.2 Sparse Matrix Formulation of the Poisson problem . . . . .	19
2.3.3 Newton's Method . . . . .	20
2.3.4 Successive Over-Relaxation Method . . . . .	22
2.3.5 Poisson Solver Algorithm . . . . .	22
<b>3 Experimental Methods</b>	<b>25</b>
3.1 Sample Fabrication . . . . .	25
3.1.1 Physical Vapor Deposition . . . . .	25
3.1.2 Chemical Vapor Deposition . . . . .	28
3.1.3 Spin Coating . . . . .	30
3.1.4 Device Architecture . . . . .	31
3.2 Device Characterization . . . . .	33
3.2.1 Atomic Force Microscopy . . . . .	34
3.2.2 Electrical Characterization . . . . .	36

---

<b>4 Results</b>	<b>39</b>
4.1 THz Electromodulation Spectroscopy for Organic Semiconductor Characterization . . . . .	39
4.2 Effects of Insulator Surface Roughness on Charge Transport in Organic Field-Effect Devices . . . . .	57
4.3 Degradation of Molecular Semiconductor Devices due to Field-Induced Gold Migration . . . . .	64
4.4 THz Spectroscopy of Band Transport in DBTTT Thin-Films . . . . .	71
<b>5 Summary and Outlook</b>	<b>89</b>
<b>Appendix</b>	<b>91</b>
<b>Bibliography</b>	<b>97</b>
<b>Acknowledgement</b>	<b>107</b>

# 1 Introduction

*"The interface is the device."*

- Herbert Kroemer, Nobel Lecture, 2000 -

In the year 2000, the Nobel Prize in Physics was awarded to Zhores I. Laferov and Herbert Kroemer for the development of semiconductor heterostructures and to Jack S. Kilby for the invention of integrated circuits. In his Nobel Lecture Herbert Kroemer said the famous words: "the interface is the device", as transition regions or interfaces play an essential role in any device [1]. More than 20 years later, this statement still holds true, especially for organic semiconductor devices, as will be shown in the course of this work.

In the same year, the Nobel Prize in Chemistry was jointly awarded to Alan J. Heeger, Alan G. MacDiarmid and Hideki Shirakawa for the discovery and development of conductive polymers, based on their work on polacetylene in 1977 [2, 3, 4]. The first organic field-effect transistor based on polythiophene was presented by Tsumura et al. in 1986 [5]. Since then, the research in organic electronics has expanded. The achieved mobility values increased from  $10^{-5}$  cm<sup>2</sup>/Vs to  $10^1$  cm<sup>2</sup>/Vs within the next 20 years [6]. It is therefore not surprising, that organic electronics soon found its first commercial applications, such as in organic light-emitting diodes for display technologies [7], sensors [8] or identification tags [9]. Despite the successful history of organic electronics over the last decades, organic semiconductors still exhibit inferior performance compared to their crystalline counterparts such as silicon or gallium-nitride, which can achieve mobilities exceeding 1000 cm<sup>2</sup>/Vs. Furthermore, research is often focused on the development of new materials and devices with higher mobilities, while the study of fundamental physical principles within such materials is lacking in new insights. The never-ending race to push the maximum mobility of organic field-effect devices higher and higher also leads to a loss of confidence in published values, as mobility over-estimations often occur [10]. In particular, transistor-curve measurements, the standard method for mobility determination, are susceptible to a variety of influences such as to the device architecture, to the contact geometry as well as to the scanning routine [11]. Therefore, refocusing on the fundamental physics within organic field-effect devices, critical assessment of conductivity data extraction as well as using new investigation methods or spectroscopic tools is essential to continue the successful progress in the research of organic electronic materials.

One promising method that could lead to novel insights within the field of organic thin-film devices is terahertz (THz) electromodulation spectroscopy. Its ability to access intrinsic charge transport properties has already been demonstrated on silicon [12] as well as

gallium-nitride [13]. Some first principle measurements on the molecular semiconductors pentacene and C12-BTBT-C12 confirmed its applicability to such low-mobility organic materials [14, 15].

The aim of this work is to identify dominating phenomena limiting charge carrier transport within thin films of molecular semiconductors using THz electromodulation spectroscopy. Some relevant questions within this thesis are: How can THz electromodulation be used to gain insight into the intrinsic transport physics and what are advantages of this technique? How do interface properties within the device influence charge transport? Why do molecular field-effect devices suffer from performance degradation during operation? Why do organic thin-film devices exhibit such small mobilities?

To answer these questions, the performance stability over time of the investigated devices needs to be assessed. Some THz measurements require accumulation times of up to 24 hours, which is often a time range in which the devices suffer from significant degradation. Moreover, the influence of interfaces, such as the insulator-semiconductor interface as well as the semiconductor-contact interface, is investigated by combining experimental atomic-force microscopy scans with numerical calculations. Additionally, the choice of contact materials is thoroughly examined by THz spectroscopic methods. Temperature-dependent and frequency resolved THz spectroscopy is used to gain insight into intrinsic limiting factors of molecular field-effect devices.

This thesis is structured as follows: Chapter 2 provides the theoretical background necessary for this work. It begins with an introduction to the physics of terahertz spectroscopy, its generation and its detection. The basic concepts of organic semiconductors, relevant charge transport mechanisms as well as corresponding theoretical models are treated afterwards. At the end of the chapter, the basics for the calculation of the charge distribution in a large volume are covered.

Chapter 3 introduces into the experimental methods used throughout this work. It begins with an introduction to the required procedures for sample fabrication and a depiction of the basic architecture of the investigated samples. This is followed by an outline of the methods used to characterize organic thin-film devices.

The results of this work are discussed in Chapter 4. The findings are presented as four peer-reviewed publications. The THz electromodulation technique, its applicability for organic semiconductor characterization and its limitations are presented in Section 4.1. In Section 4.2, the influence of the insulator surface roughness on the charge carrier distribution is addressed by combining two-dimensional atomic force microscopy scans with the solution of the three-dimensional, self-consistent Poisson equation. The phenomenon of device degradation upon the migration of gold into the accumulation channel and how this can be circumvented is discussed in Section 4.3. At the end of this chapter, in Section 4.4, THz spectroscopy investigations on band transport in DBTTT thin-film devices are examined.

In Chapter 5, a concluding summary of the results of this thesis and a brief outlook on future investigations in the field of organic thin-film devices is given.

## 2 Theoretical Background

This chapter deals with the theoretical concepts necessary for the understanding this work on terahertz (THz) spectroscopy of organic semiconductors. Section 2.1 covers the fundamentals of THz spectroscopy including the generation of THz pulses and its detection. Section 2.2 introduces into the field of organic semiconductors and gives a brief overview of the basic charge transport mechanisms and outlines established charge transport models. General principles relevant for the calculation of the charge carrier distribution inside field-effect devices such as the Poisson equation, sparse matrix formulation and numerical methods for solving large systems of equations are treated within Section 2.3.

### 2.1 Introduction to Terahertz Spectroscopy

The electromagnetic spectrum is composed of several different energy bands as schematically shown in Figure 2.1. The most known one is the visible light within the wavelengths range of 380 nm to 780 nm. Wavelengths smaller than 380 nm are covered by ultraviolet radiation and x-rays. The infrared, microwave and the radiowave frequency regime is governed for wavelengths larger than 780 nm. Between the infrared and microwave regime lies the terahertz (THz) radiation. Its frequency band is not precisely determined but is often given by the frequency interval of 0.3 THz to 10 THz (1 mm to 30  $\mu\text{m}$  wavelength). [16]

For a long period of time, the THz frequency band was difficult to access, because there

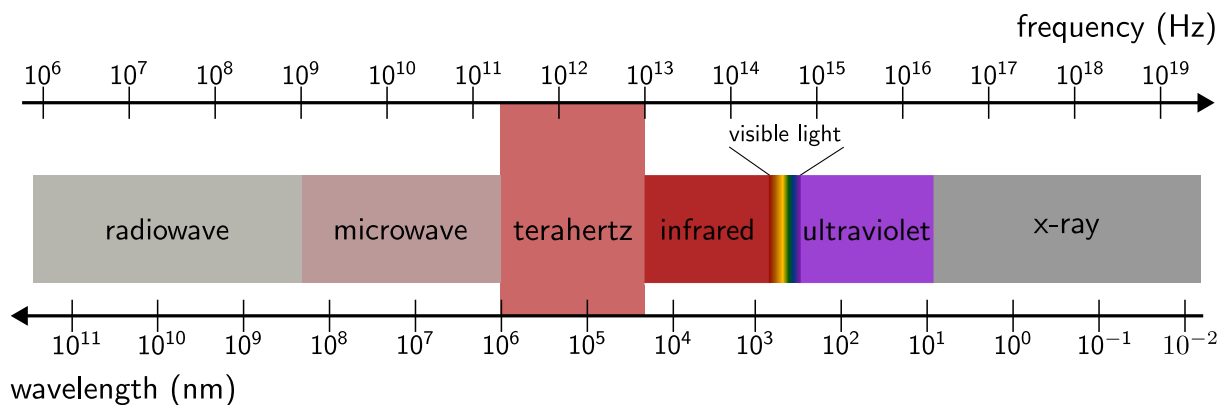


**Fig. 2.1** Spectrum of electromagnetic radiation. The THz band lies within the frequency interval of 0.3 THz to 10 THz (1 mm to 30  $\mu\text{m}$  wavelength).

the so-called optical spectrum ends and the radio wave region begins. On the one side, a few hundred GHz is the upper limit for oscillating electronic circuits [17]. On the other side, semiconductor lasers have lower limits of approximately 30 THz [18]. Although, several methods for THz generation and detection established, this frequency regime is still often referred to as the “THz gap“ and is still the least explored region of the electromagnetic spectrum.

The THz regime corresponds to photon energies of approximately 1 meV to 40 meV which is an interesting spectral range for imaging. THz radiation penetrates deep into nonpolar and nonmetallic materials such as plastic, paper, clothes, ceramics, and many more. Thus, nondestructive testing of sealed packages is feasible [19]. Furthermore, in contrast to x-rays, THz waves do not lead to photoionization in biological tissue. They are efficiently absorbed by water and penetrate only a few mm into the human body. This makes it a valuable tool for non-invasive medical imaging of the skin [20].

Another important application is THz spectroscopy. Several physical phenomena occur within the energetic range of the THz regime, such as low-energy excitations in electronic materials, collective vibrational or torsional modes in condensed-phase media, and rotational and vibrational transitions in molecules [21]. Thus, it can be used in agricultural applications for water content measurements, detection of pesticides, soil and seed inspection, detection of genetically modified crops and many more [22]. Also, THz spectroscopy can be utilized in the field of security as it allows the detection of drugs and explosives [23]. One of the most prominent applications is the investigation of intrinsic properties of semiconductors. THz spectroscopy facilitates probing high-frequency charge carrier dynamics as well as impurity states [24]. By examining the optical properties during the modulation of the free charge carrier density inside the semiconductor, information on the AC conductivity can be obtained. One key strength is the simultaneous acquisition of the real and imaginary part of the conductivity without the need of applying Kramers-Kronig relation. By fitting its frequency dependence important parameters can be extracted such as the scattering rate or the plasma frequency. [25]

Throughout this work, a novel THz spectroscopy technique is utilized for the investigation of organic semiconductor materials. In contrast to the widely applied method of probing optically excited charge carriers, electronically injected charges are investigated. THz electro-modulation (EM) spectroscopy allows for the direct measurement of differential transmission signals and the distinct sensing of either injected holes or electrons. A thorough presentation and discussion of this technique is given in Section 4.1. However, in the following Sections, the generation (compare Section 2.1.1) and the detection (compare Section 2.1.2) of THz pulses is discussed in detail.

### **2.1.1 Generation of Terahertz-Pulses**

In the early days of THz research, there was a lack of bright and stable THz sources. Nowadays, a variety of different methods for the generation of broadband THz pulses exist, such

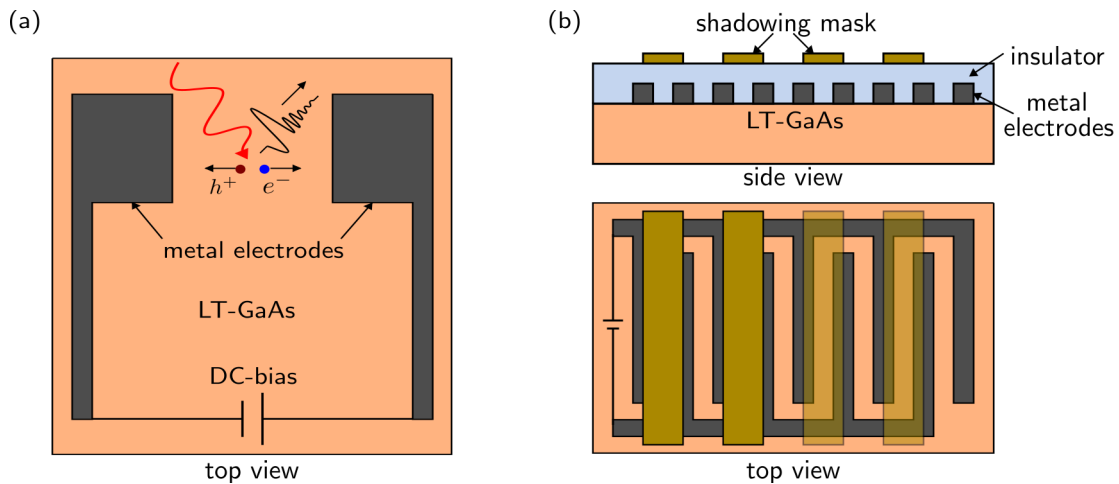


**Fig. 2.2** (a) Schematic architecture and principle of a classic PCA. (b) Schematic architecture of a MSM structure with an interdigitated finger electrode structure and a metallic shadowing mask on top for unidirectional carrier acceleration.

as optical rectification [26], radiation from electron accelerators [27], radiation from laser-induced plasma [28], the usage of resonant-tunneling diodes [29], cold plasma oscillations [30], stimulated polariton scattering [31], and the interaction of femtosecond-laser pulses with different materials, including topological insulators [32], semiconductor surfaces [33], metasurfaces [34] or spintronic materials [35].

In this work, a photoconductive antenna (PCA) is used for pulsed THz generation. A schematic of a PCA is shown in Figure 2.2 (a). The basic architecture of a PCA consists out of a photoconductive material on which metal electrodes are deposited. While a voltage bias is applied between the antenna electrodes, free charge carriers (electrons and holes) are photogenerated upon irradiation with photon energies larger than the bandgap of the PCA material. The free carriers are accelerated towards the electrodes due to the DC bias. Simultaneously, charge trapping into defect sites occur, which results in a decrease of the charge density. The variations in photocurrent density results in the generation of electromagnetic waves following [16]:

$$E_{THz} \propto \frac{\partial j(t)}{\partial t} \quad (2.1.1)$$

where  $E_{THz}$  is the radiated electric field and  $j(t)$  the time dependent current density. To generate radiation within the THz regime, the switching of the PCA should happen on a picosecond timescale. The switch-on time is determined by the pulse duration, and thus a femtosecond laser is used (mostly titanium-sapphire laser). The switch-off time is mainly defined by the photogenerated carrier lifetime in the PCA material. Often, low-temperature grown gallium arsenide (LT-GaAs) is used as the photoconductive material. Due to a high density of point defects the lifetime of the photogenerated carriers is in the subpicosecond

range. [24]

The simple PCA structure (Fig. 2.2 (a)) exhibits some severe drawbacks such as a small optically excited area and the need for high electric fields. By minimizing the gap between the electrodes and by using a interdigitated finger structure those problems can be circumvented. However, an interdigitated finger electrode geometry has distinct areas where photocarriers are accelerated in opposite directions resulting in destructive interference of the generated electromagnetic wave. To ensure unidirectional carrier acceleration a slightly modified metal-semiconductor-metal (MSM) structure is used as can be seen in Figure 2.2 (b). Here, every second electrode gap is covered by a metallic shadowing mask. In these regions no carriers are generated as the incoming pulse is reflected. Thus, unidirectional acceleration can be ensured. In the far-field the THz radiation interferes constructively leading to high-intensity pulses. [36]

### 2.1.2 Detection of Terahertz-Pulses

A THz detector collects information of the incoming electromagnetic radiation and converts it into readable data. Several detection techniques exist, which rely on different mechanisms. Nevertheless, every detection system can be characterized by the same quantities such as the detection bandwidth, the sensitivity, the linearity and many more [37].

Two key parameters are the noise and the signal-to-noise ratio (SNR) of the detection system. Noise is defined as the measurement of unwanted signal, which mostly has a random distribution. The SNR is defined as the ratio of signal power to noise power [38]:

$$SNR = \frac{P_{signal}}{P_{noise}}. \quad (2.1.2)$$

Another definition of the SNR uses the mean signal  $\bar{S}$  and the standard deviation of the signal  $\sigma_S$  [39]:

$$SNR' = \frac{\bar{S}}{\sigma_S}. \quad (2.1.3)$$

Most systems measure the signal with a certain sampling frequency  $\nu_{sampl.}$ . Thus, if  $\nu_{sampl.}$  increases, then the systems  $SNR'$  increases as well due to the integration of more measurement points during the same time interval. Thus, the  $SNR'$  is multiplied with the factor  $\sqrt{\nu_{sampl.}}$  to obtain  $SNR^*$ :

$$SNR^* = \frac{\bar{S}}{\sigma_S} \cdot \sqrt{\nu_{sampl.}}. \quad (2.1.4)$$

The  $SNR^*$  is in the unit of  $\sqrt{\text{Hz}}$ . The relation of the spectroscopic  $SNR^*$  and the general

$SNR$  is given by:

$$SNR = SNR^* \cdot \sqrt{T_{int}} \quad (2.1.5)$$

where  $T_{int}$  is the integration time. The  $SNR$  can be contributed to a specific measurement whereas the  $SNR^*$  characterizes the measurement technique. Therefore, the systems  $SNR^*$  essentially determines the necessary acquisition time for the measurement. The noise is reduces with the square of the integration time. This means a system with a ten times smaller  $SNR^*$  would require a measurement time which is 100 times longer to achieve identical results. [37]

The  $SNR^*$  of a system strongly depends on the type of detector. Several techniques to detect THz radiation exist, such as electro-optic sampling [40], using an unbiased PCA [41], bolometric methods [42], using Golay cells [43], using laser-induced air plasma [44], heterodyne detection [45], and many more.

Nevertheless, free-space electro-optic (EO) sampling is by far the most applied technique. It is a purely optical method and offers a flat frequency response and thus a high linearity, which makes it an attractive method for broadband THz detection. EO sampling is based on the Pockels effect, the change of birefringence of a sensor crystal in presence of an electric field  $E$ . Thus, a linearly polarized wave will be elliptically polarized in dependence of the field strength  $E$ . This polarization can be explained by different phase velocities of the orthogonal wave components with respect to the principal axes of the EO crystal, due to different refractive indices. [46]

The phase difference  $\Delta\phi$  also called phase retardation, can be expressed by [47]:

$$\Delta\phi = \frac{\omega n^3 E r_{41} L}{c} \quad (2.1.6)$$

where  $\omega$  is the angular frequency of the probe pulse,  $n$  is the unperturbed refractive index,  $r_{41}$  is the only nonzero coefficient of the electro-optic tensor,  $L$  is the crystal length and  $c$  is the velocity of light in vacuum. [47]

A schematic of the experimental detection setup and of the corresponding polarizations of the probe pulse are shown in Figure 2.3 (a) and (b), respectively. The THz pulse and the probe pulse fall onto an EO crystal (here: ZnTe). Typically, both waves are linearly polarized parallel to the  $[1\bar{1}0]$  direction of the ZnTe crystal. Without the presence of a THz field, the probe pulse passes with linear polarization through the EO crystal and is afterwards circularly polarized by an  $\lambda/4$  plate. A Wollaston prism splits the probe beam into two orthogonal components, which fall onto a balanced photodetector, where the difference in intensity  $\Delta I = I_x - I_y$  is measured. In absence of a THz field the intensity difference  $\Delta I$  is zero.

In presence of a THz field, the refractive index of the EO crystal changes and its birefringence causes a slightly elliptic polarization of the probe beam. Then, the  $\lambda/4$  plate translates the probe polarization into a nearly circular polarization resulting in a non-zero intensity difference  $\Delta I$  proportional to the applied THz field amplitude.  $\Delta I$  can be approximated via

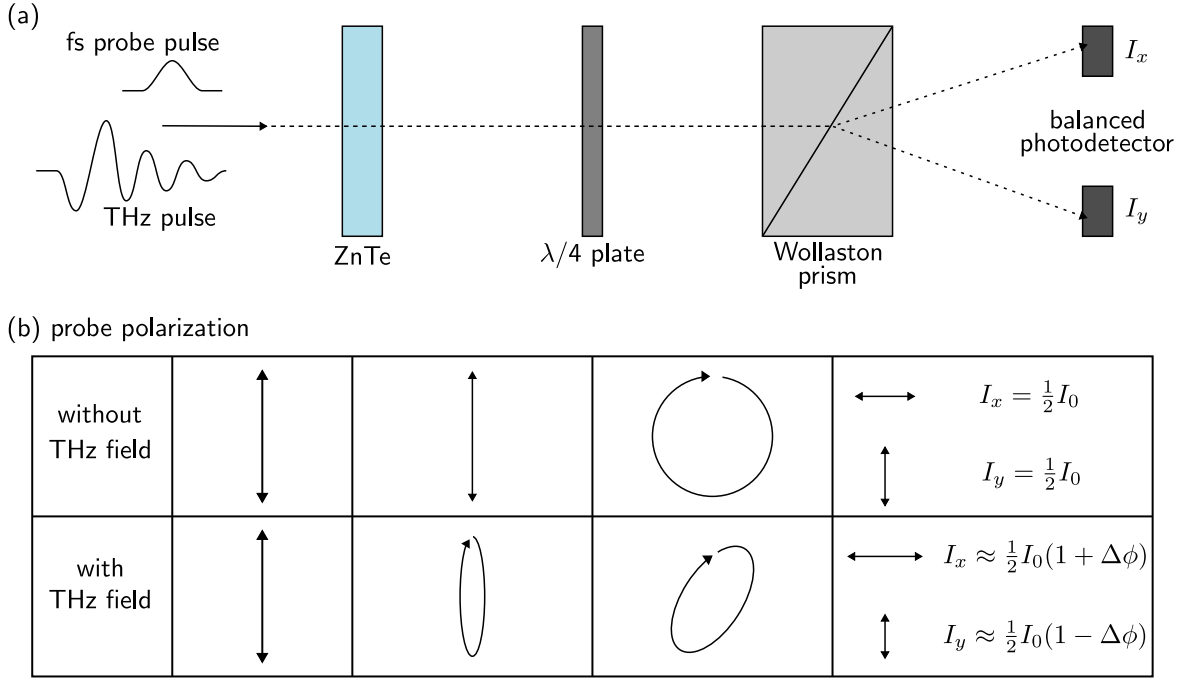


**Fig. 2.3** Schematic principle of the THz detection setup using EO sampling (a). Corresponding probe pulse polarizations with and without the presence of a THz field (b). Figure adapted from [24].

[48]:

$$\Delta I \approx I_p \cdot \Delta\phi = I_p \cdot \frac{\omega n^3 E_{THz} r_{41} L}{c} \quad (2.1.7)$$

where  $I_p$  is the probe intensity and  $E_{THz}$  the electric field strength of the THz-pulse. The complete time-dependent THz pulse can be obtained by modulating the time-delay between the THz-pulse and the probe pulse. This is achieved by introducing a delay-stage which modulates the length of the pathway of the exciting-pulse beam which generates the THz radiation. [40, 48]

## 2.2 Charge Transport in Organic Semiconductors

Nowadays, numerous applications rely on organic semiconductor (OSC) technology, such as organic light emitting diodes used in the display industry [49], radio-frequency identification (RFID) tags for remote identification and localization of objects [50] and many more [51]. But, OSC devices still exhibit low carrier mobilities  $\mu$  and thus low conductivities  $\sigma$  in comparison to its crystalline counterparts (compare Table 2.1). The occurring charge transport

mechanisms determine the conductivity. Therefore, fundamental understanding of charge transport in organic semiconductors is of great interest.

material	$\mu_e$ (cm <sup>2</sup> /Vs)	$\mu_h$ (cm <sup>2</sup> /Vs)	reference
gallium arsenide	9000	450	[52, 53]
crystalline silicon	1400	400	[54, 55]
polycrystalline silicon	50-100	20-30	[56, 57]
amorphous silicon	<1	<1	[58]
organics	5-10	30-50	[59, 60]

**Table 2.1** Comparison of electron and hole mobilities ( $\mu_e$  and  $\mu_h$ ) of different materials.

This chapter covers the basic theory about charge transport in organic semiconductors. A brief introduction into molecular semiconductors is given in Section 2.2.1. Section 2.2.2 discusses the most important charge transport mechanisms such as Bloch transport and hopping transport. At the end of this chapter, in Section 2.2.3, the main charge transport models relevant in the field of organic semiconductors are outlined.

## 2.2.1 Molecular Organic Semiconductors

In contrast to inorganic semiconductors, organic semiconductors (OSCs) are mainly build from carbon compounds. OSCs can be divided into two subgroups, polymers and molecular semiconductors (MSCs). In this work, the focus lies on MSCs, but the fundamental principle of charge transport is similar in polymeric semiconductors.

Charge transport in OSCs is based on the concept of charge carrier de-localization within conjugated  $\pi$ -orbitals. The formation of molecular orbitals results from the superposition of atomic orbitals. A molecular orbital describes possible states of the molecules' electrons and is given by the wavefunction  $\Psi_{MO}$ , which is a solution of the Schrödinger equation [61]:

$$H\Psi = E\Psi, \quad (2.2.1)$$

where  $H$  is the Hamilton operator and  $E$  the energy of the system. Each molecular orbital is characterized by quantum numbers, which define its form and energy and by a certain energy eigenvalue, which can be interpreted as the probability of finding an electron in the corresponding volume element. The exact determination of  $\Psi_{MO}$  is nearly impossible, thus an approximation can be achieved by the method of linear combination of atomic orbitals (LCAO). The wave function is built as a linear superposition of atomic orbitals  $\Psi_{AO}$ :

$$\Psi_{MO} = c_1\Psi_{AO1} \pm c_2\Psi_{AO2}, \quad (2.2.2)$$

where  $c_{1/2}$  are coefficients which are chosen in a way that the energy  $E$  of the Schrödinger equation is minimized and therefore a stable compound is formed [61]. Several combinations

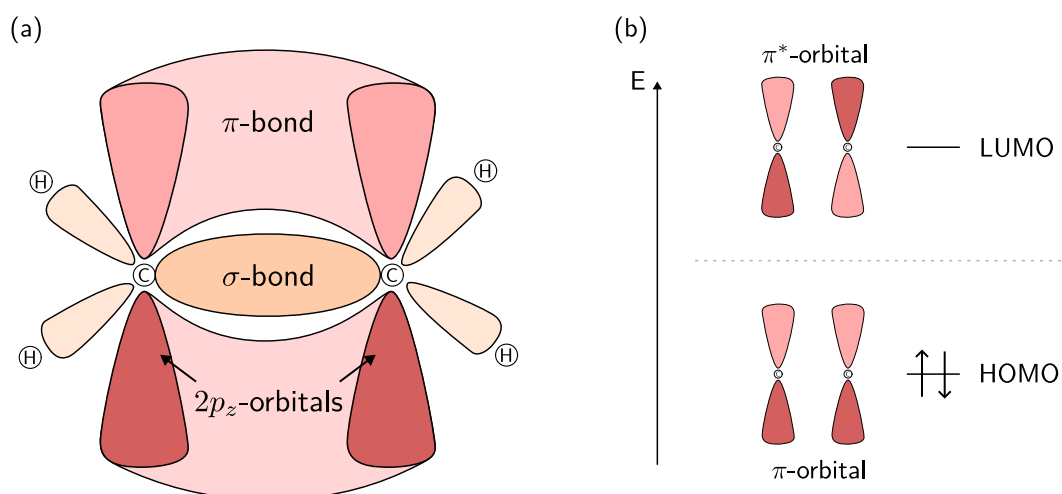


**Fig. 2.4** Schematic of the molecular orbitals of ethene build from six  $sp^2$  hybridized orbitals forming the  $\sigma$ -bonds as well as two  $2p_z$  orbitals arising in  $\pi$ -bonds (a). Generally, in molecular orbital theory, the existence of double bonds can be described with the simultaneous formation of a  $\sigma$ - and a  $\pi$ -bond, as depicted. Corresponding energy levels of the HOMO and LUMO level of ethene, which arise from a bonding  $\pi$ -orbital and an antibonding  $\pi^*$ -orbital (b). The difference in energy of the two levels is the bandgap energy  $E_G$ .

of atomic orbitals are possible and thus different molecular orbitals arise. A schematic image of the molecular orbitals of ethene is shown in Figure 2.4 (a). The energetic levels of distinct molecular orbitals are exemplarily depicted in Figure 2.4 (b). Due to the Pauli principle, only two electrons with different spin states are allowed in the same orbital. The filling of the orbitals with electrons occurs in a way that the overall energy of the molecule is minimized and thus not all orbitals are occupied. The most important orbitals are the highest occupied molecular orbital (HOMO) and the lowest unoccupied molecular orbital (LUMO), which are the frontier orbitals of the system. The energy difference between the HOMO and the LUMO level can be referred to as the bandgap energy  $E_G$ . [62]

The overlap of molecular orbitals defines the force holding the atoms together. Orbital overlap in the region directly between the carbon atoms gives rise to  $\sigma$ -orbitals and corresponds to the so-called  $\sigma$ -bond. Orbitals which are situated laterally, above and below the plane of the nuclei, are called  $\pi$ -orbitals. In case the  $\pi$ -orbitals overlap, a  $\pi$ -bond is formed which is much weaker than the  $\sigma$ -bond. The overlap of  $\pi$ -orbitals is also called  $\pi$ -conjugation, which leads to a delocalization of  $\pi$ -electrons among an electron cloud, which is distributed across the whole molecule as schematically depicted in Figure 2.4 (a). Basically,  $\pi$ -conjugated systems exhibit a smaller energy and are thus more stable. Examples for conjugated systems are linear carbon chains with alternating single and double bonds (e.g. ethylene, butadiene, ...), molecules with aromatic compounds (e.g. benzene, thiophene, ...) or polymers built from carbon chains, aromatics or both such as polyacetylene, polythiophene or polyphenylene vinylene. [61, 62] The energy splitting of the HOMO and LUMO level is the reason for the semiconducting properties of certain organic compounds.

In contrast to organic polymers, where long coherent chains with large  $\pi$ -conjugated systems arise, molecular semiconductors are small  $\pi$ -conjugated molecules which organize themselves in a crystalline arrangement. The constituents of the resulting molecular solid are only weakly bound by Van-der-Waals forces. Charge transport in such materials is determined by the overlap of neighboring  $\pi$ -conjugated orbitals, which can be expressed by the transfer integral  $J$ . Thus, the crystal structure and the overall crystallinity has a major influence on the charge transport mechanisms in MSC devices. [63]

### 2.2.2 Charge Transport Mechanisms

In general, semiconductors are characterized by their carrier mobility  $\mu$ . The mobility relates the drift velocity  $v$  of free charge carriers to an electric field  $E$  acting upon the charges. The drift velocity can be written as [64]:

$$v = \mu E. \quad (2.2.3)$$

In the case of  $n$  charge carriers per volume element, Equation 2.2.3 gives the current density  $j$ :

$$j = nev = ne\mu E = \sigma E, \quad (2.2.4)$$

where  $\sigma$  is the materials conductivity, given by  $\sigma = ne\mu$ . [64]

For organic semiconductors, the current density and thus the charge transport is determined by the transfer of electrons between LUMO sites or holes between HOMO sites. Thus, the electronic coupling strength between neighboring molecules, expressed by the transfer integral  $J$ , mainly determines the influence of static and dynamic disorder on the nature of charge transport within organic materials. The charge transport can be categorized into distinct transport regimes: band transport and hopping transport. Information on the type of transport can be obtained by the temperature dependence of the mobility  $\mu(T)$  as schematically is shown in Figure 2.5. In case that the interaction energy between neighboring sites is large and disorder is weak, the charge carriers are strongly delocalized and band transport dominates. Bloch waves propagate through the crystal and may scatter at lattice vibrations. Thus, the temperature dependence of the mobility should exhibit the characteristic  $T^{-3/2}$  dependence, which relates to increased scattering at acoustic phonons at elevated temperatures [64]. Hopping transport dominates if any type of disorder becomes significant in comparison to the interaction with the nearest neighbor. The concept of delocalized wave functions collapses and charge carriers are localized at individual sites. The charge transfer becomes thermally activated and thus the mobility exhibits a temperature dependent activation  $\mu(T) \propto e^{1/T}$ , also known as Arrhenius-type behavior [65, 66]. Two special cases of

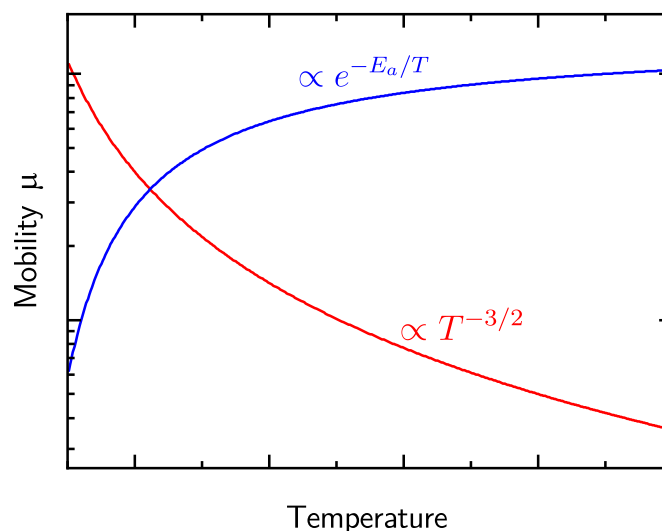


**Fig. 2.5** Schematic of characteristic temperature dependencies of the mobility  $\mu(T)$  for band transport (red) and hopping transport (blue).

hopping transport are polaronic transport and disorder-controlled transport. In case of polaronic transport, the system is perfectly ordered and hopping results from dynamic disorder due to phonons, intra- and inter-molecular vibrations. The hopping rate is thermally activated and well-defined leading to a time-independent diffusivity and mobility. For strongly disordered systems, the hopping rates are asymmetric. In contrast to polaronic transport, the forward and backward jumps have different activation energies and thus the diffusivity and mobility are time-dependent. [65]

### 2.2.3 Charge Transport Models

During the last decades, several theoretical frameworks developed trying to explain the fundamental charge transport physics in organic semiconducting devices. Especially for the interpretation of THz spectroscopy data, a solid model for the description of the AC conductivity is crucial. Thus, in the urge to explain experimental data, a variety of phenomenological charge transport models emerged. Each of those is based on some physically relevant assumptions. Within this section a brief overview of some of the most important charge transport models, which have been applied throughout this work, is given.

#### Drude Model

One model for the description of charge transport in semiconductors is the Drude model, which has been developed by Paul Drude in the year 1900 [67]. It is based on the assumption

of free charge carriers within metals, which do not interact among each other and are only scattered at the atomic nuclei. Another important assumption is, that after each scattering process, the momentum is completely randomized. Even though the basic assumptions are wrong with respect to today's state of physics [68], the Drude model describes charge transport in semiconductors quantitatively correct [69] and is thus still a relevant concept for the interpretation of measurement results. The mobility is described by an effective mass  $m^*$  of the charge carriers, which depends on the band structure of the semiconductor, and by a scattering time  $\tau$ , which defines the time between two consecutive scattering events. The mobility and the scattering time are related via:

$$\mu_{Drude} = \frac{e\tau}{m^*}, \quad (2.2.5)$$

where  $e$  is the elementary charge. The frequency dependent AC-conductivity  $\tilde{\sigma}$  is obtained by solving the equation of motion for the location  $x(t)$  with a time dependent external field  $E(t)$ :

$$m^* \frac{\partial^2 x}{\partial t^2} + \frac{m^*}{\tau} \frac{\partial x}{\partial t} = eE(t). \quad (2.2.6)$$

With the ansatz of  $x(t) = x(\omega)e^{-i\omega t}$  and  $E(t) = E(\omega)e^{-i\omega t}$  it can be solved to be:

$$x(\omega) = -\frac{e\tau}{m^*} \frac{1}{i\omega + \omega^2\tau} E(\omega). \quad (2.2.7)$$

Then, with help of Equation 2.2.4 the AC-conductivity is defined as [70]:

$$\tilde{\sigma}(\omega) = \frac{ne^2\tau}{m^*} \frac{1}{1 - i\omega\tau} = \sigma_{DC} \frac{1}{1 - i\omega\tau} \quad (2.2.8)$$

where  $\sigma_{DC}$  is the DC-conductivity. The real and imaginary part of  $\tilde{\sigma}$  are exemplary plotted in Figure 2.6.

### Drude-Smith Model

A variety of measurements, which cannot be explained with the Drude model gave rise to the development of extended Drude models, such as the Drude-Smith model [71]. In contrast to the classical Drude model, it is based on the assumption, that the momentum after a scattering event is not fully randomized. It can be described by the generalized Drude formula:

$$\tilde{\sigma}_{DS}(\omega) = \frac{ne^2\tau}{m^*} \frac{1}{1 - i\omega\tau} \left[ 1 + \sum_{n=1}^{\infty} \frac{c_n}{(1 - i\omega\tau)^n} \right], \quad (2.2.9)$$

where  $c_n$  is a coefficient representing the fraction of the charge carriers original velocity that is preserved after the  $n$ -th scattering event. [71]

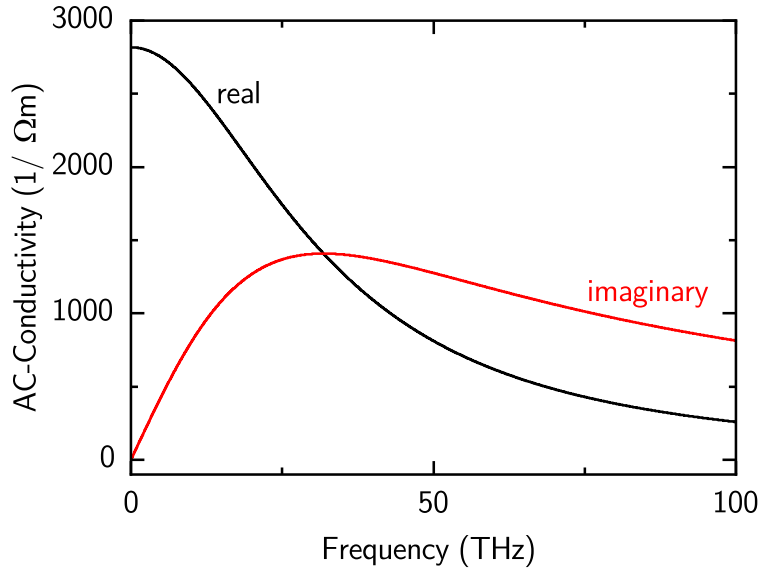


**Fig. 2.6** Real (black) and imaginary (red) part of the AC-conductivity  $\tilde{\sigma}$  for  $n = 2 \times 10^{25} \text{ 1/m}^3$ ,  $\tau = 5 \text{ fs}$  and  $m^* = m_e$ , where  $m_e$  is the electron mass (comp. Equ. 2.2.8).

Mostly, the single scattering approximation is used, where only the first scattering event is considered:

$$\tilde{\sigma}_{DS}(\omega) = \frac{ne^2\tau}{m^*} \frac{1}{1 - i\omega\tau} \left[ 1 + \frac{c}{(1 - i\omega\tau)} \right]. \quad (2.2.10)$$

This approximation allows good agreements with experimental results when a negative coefficient  $c$  is used which is often interpreted as back-scattering at grain boundaries [72, 73, 74]. The real and imaginary part of the Drude-Smith-conductivity for several values of  $c$  are shown in Figure 2.7. It can be seen that the Drude-Smith modification leads to a negative imaginary part of the conductivity for  $c < -0.5$ .

### Localization-Modified Drude Model

Mott and Kaveh proposed another modification of the Drude model, which addresses weak disorder-induced localization [75]. The resulting model is called localization-modified Drude (LMD) model. This correction term is obtained by perturbation theory and is also called diffusion correction. It is important to note, that Mott and Kaveh pointed out that the elastic mean free path of the charge carriers has to be greater than the correction term in order to apply this modification. Nevertheless, this is not always given, as will be shown in Section 4.4. The real and the imaginary part of the LMD model are given by [76, 77]:

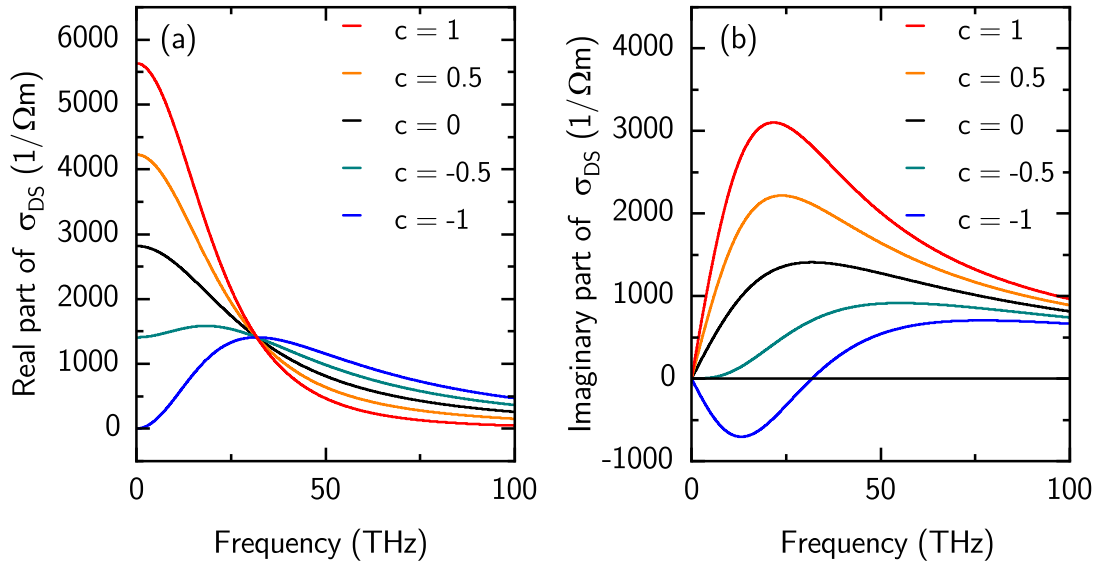


**Fig. 2.7** Real (a) and imaginary (b) part of the AC-Drude-Smith conductivity  $\sigma_{DS}$  for different values of  $c$  with  $n = 2 \times 10^{25} \text{ 1/m}^3$ ,  $\tau = 5 \text{ fs}$  and  $m^* = m_e$ , where  $m_e$  is the electron mass (comp. Equ. 2.2.10). For  $c = 0$  the Drude-conductivity is obtained.

$$\sigma_{1,LMD}(\omega) = \frac{\epsilon_0 \omega_p^2 \Gamma}{\omega^2 + \Gamma^2} \left[ 1 - \frac{C}{(k_F v_F)^2} \Gamma^2 + \frac{C}{(k_F v_F)^2} \Gamma^{1.5} (3\omega)^{0.5} \right], \quad \text{and} \quad (2.2.11)$$

$$\sigma_{2,LMD}(\omega) = \frac{\epsilon_0 \omega_p^2 \omega}{\omega^2 + \Gamma^2} \left[ -1 + (1 - \sqrt{6}) \frac{C}{(k_F v_F)^2} \Gamma^2 + \frac{C}{(k_F v_F)^2} \Gamma^{2.5} (3/\omega)^{0.5} \right], \quad (2.2.12)$$

where  $\epsilon_0$  is the vacuum permittivity,  $\omega_p$  is the plasma frequency,  $\Gamma = 1/\tau$  is the scattering rate,  $C$  is a constant close to unity,  $k_F$  is the Fermi wavevector and  $v_F$  is the Fermi velocity. The real and imaginary part of the LMD model are shown in Figure 2.8.

### Drude-Anderson Model

The Drude-Anderson (DA) model by Fratini et al. assumes the presence of a strong dynamical disorder, which results in carrier localization [78]. Therefore, it is often called transient or dynamic localization scenario. In this model, several time constants are introduced such as a Drude relaxation time  $\tau$ , a backscattering time  $\tau_b$  and an inelastic time  $\tau_{in}$  with  $\tau < \tau_b < \tau_{in}$ . The real part of the DA conductivity  $\sigma_{1,DA}$  is given by [79]:

$$\sigma_{1,DA}(\omega) = \frac{ne^2 L^2 \tanh\left(\frac{\hbar\omega}{2k_B T}\right)}{\tau_b - \tau} \frac{1}{\hbar\omega} \cdot \text{Re} \left[ \frac{1}{1 + \tau/\tau_{in} - i\omega\tau} - \frac{1}{1 + \tau_b/\tau_{in} - i\omega\tau_b} \right] \quad (2.2.13)$$

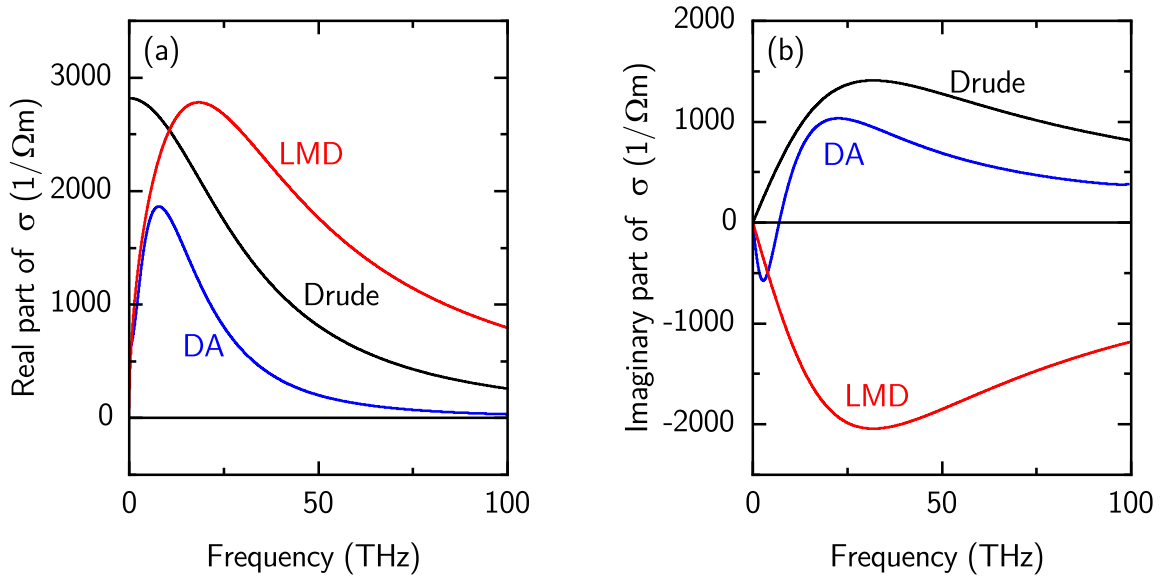


**Fig. 2.8** Real (a) and imaginary (b) part of the LMD (red) and the DA conductivity (blue). For all graphs the scattering time is chosen to be  $\tau = 5$  fs. For the LMD model  $C/(k_f v_F)^2 = 25 \text{ fs}^2$  and for the DA model  $\tau_b = 50$  fs and  $\tau_{in} = 150$  fs is used. As a reference the Drude conductivity from Fig. 2.6 is added as black lines.

where  $L^2$  is defined as:

$$L^2 = \frac{2k_B T}{m_h^*} \tau (\tau_b - \tau). \quad (2.2.14)$$

The real and imaginary part of the DA model are shown in Figure 2.8, with the imaginary part being obtained by Kramers-Kronig relation.

## 2.3 Charge Distribution Calculation

The charge carrier density, and with it the charge carrier distribution, has a significant impact on the physics inside field-effect devices. This chapter covers the fundamentals of the calculation of charge carrier distributions. Section 2.3.1 gives a brief introduction to the Poisson equation and the Fermi-Dirac distribution necessary to calculate the density of states within the semiconductor device. Section 2.3.2 explains how the physical interactions can be translated into a sparse matrix, which allows a drastic reduction of computational cost. The applied numerical methods, such as the Newton method and the successive over-relaxation method are briefly introduced in Section 2.3.3 and Section 2.3.4, respectively. At the end of this chapter in Section 2.3.5, the basic algorithm flowchart to solve the Poisson equation for large systems is outlined.

### 2.3.1 Poisson Equation & Fermi-Dirac Statistics

The Poisson equation is based on the Maxwell equations of electrostatic fields:

$$\vec{\nabla} \cdot \vec{E}(\vec{r}) = \frac{1}{\varepsilon_0} \rho(\vec{r}) \quad (2.3.1)$$

$$\vec{\nabla} \times \vec{E}(\vec{r}) = 0 \quad (2.3.2)$$

where  $\vec{E}(\vec{r})$  is the vectorial electric field,  $\vec{r}$  is the position vector,  $\varepsilon_0$  is the permittivity of vacuum and  $\rho(\vec{r})$  the local charge carrier density. The electric field can be expressed as the negative gradient of the scalar electric potential  $\varphi(\vec{r})$ . Then, the Maxwell equations yield the Poisson equation:

$$\Delta\varphi(\vec{r}) = -\frac{1}{\varepsilon_0} \rho(\vec{r}). \quad (2.3.3)$$

If the local permittivity  $\varepsilon(\vec{r})$  is taken into account the Poisson equation is rewritten as:

$$\vec{\nabla} \left[ \varepsilon(\vec{r}) \vec{\nabla} \varphi(\vec{r}) \right] = -\frac{1}{\varepsilon_0} \rho(\vec{r}). \quad (2.3.4)$$

Another possibility is to express the Poisson equation in an integral form:

$$\int \vec{\nabla} \left[ \varepsilon(\vec{r}) \vec{\nabla} \varphi(\vec{r}) \right] dV = -\frac{Q}{\varepsilon_0} \quad (2.3.5)$$

where  $Q$  is the charge within the volume  $V$ . The application of Gauß's law transforms the volume integral into a surface integral:

$$\oint \left[ \varepsilon(\vec{r}) \vec{\nabla} \varphi(\vec{r}) \right] d\vec{A} = -\frac{Q}{\varepsilon_0} \quad (2.3.6)$$

To explicitly solve the Poisson equation it is necessary to consider boundary conditions of the volume. If the potential ( $\varphi$ ) on a closed surface is known, it is called Dirichlet boundary condition. In case, the orthogonal derivative of the potential ( $\vec{n} \cdot \vec{\nabla} \varphi$ ) on a closed surface is given, it is called Von-Neumann boundary condition. [80]

In some cases the charge carrier density  $\rho$  does not only depend on the location but as well on the potential  $\rho(\varphi)$ :

$$\vec{\nabla} \left[ \varepsilon(\vec{r}) \vec{\nabla} \varphi(\vec{r}) \right] = -\frac{1}{\varepsilon_0} \rho(\vec{r}, \varphi). \quad (2.3.7)$$

This modification of the Poisson equation is often called Poisson-Boltzmann equation as it is mainly used in electrochemical calculations where the distribution of charges follows the Boltzmann statistics [81]. Within this work, the distribution of charge carriers inside the

semiconductor is governed by the Fermi-Dirac statistics. The charge carrier density  $n$  within the band of a semiconductor is obtained by [82]:

$$n = \int_{E_C}^{\infty} N(E)f(E)dE \quad (2.3.8)$$

where  $N(E)$  is the density of states for electrons inside a semiconductor at energy  $E$ ,  $f(E)$  is the Fermi function for electrons at energy  $E$  and  $E_C$  is the energy of the conduction band edge. The Fermi-function, often also denoted as the Fermi-Dirac distribution function, describes the probability of occupancy of a state with energy  $E$  at temperature  $T$ :

$$f(E) = \frac{1}{1 + \exp\left(\frac{E-E_F}{k_B T}\right)} \quad (2.3.9)$$

where  $k_B$  is the Boltzmann constant and  $E_F$  the Fermi energy at  $T = 0$  K of the semiconductor. The density of states at energy  $E$  inside the semiconductor can be obtained via [83]:

$$N(E) = g \frac{1}{2\pi^2} \left(\frac{2m_e^*}{\hbar^2}\right)^{3/2} \sqrt{E - E_C} \quad (2.3.10)$$

where  $g$  describes the degeneracy of the band,  $m_e^*$  is the effective electron mass and  $\hbar$  is the reduced Plank's constant.

The charge carrier density  $n$  can be rewritten as:

$$n = N_{eff} \mathcal{F}_{1/2}(\eta_F) \quad (2.3.11)$$

where  $N_{eff}$  is the effective density of states:

$$N_{eff} = 2g \left(\frac{m_e^* k_B T}{2\pi\hbar^2}\right)^{3/2} \quad (2.3.12)$$

and using the Fermi-Dirac integral  $\mathcal{F}_{1/2}$ :

$$\mathcal{F}_{1/2} = \frac{1}{\Gamma(3/2)} \int_{E_C}^{\infty} \frac{\eta^{1/2}}{1 + \exp(\eta - \eta_F)} d\eta \quad (2.3.13)$$

with  $\eta_F = (E_F - E_C)/k_B T$  and  $\eta = (E - E_C)/k_B T$  [82]. The Fermi-Dirac integral and also its derivatives can only be obtained by numerical approximations. A thorough review can be found for example in Reference [84]. With such approximations, the relative error can be minimized to values in the range of  $10^{-5}$  [85].

For the case of an applied external potential  $\phi < 0$  the band edges are bent upwards to higher energies. This leads to a redefinition of  $\eta$ . Especially, the situation is different for electrons and holes. For electrons a shift of the conduction band  $E_C$  is relevant and for holes a shift of the valence band  $E_V$ . Thus,  $\eta_e$  for electrons and  $\eta_h$  for holes is defined as:

$$\eta_e = (E_F - (E_C - e\phi)) / (k_B T), \quad (2.3.14)$$

$$\eta_h = ((E_V - e\phi) - E_F) / (k_B T). \quad (2.3.15)$$

### 2.3.2 Sparse Matrix Formulation of the Poisson problem

Every system of equations can be described via a matrix formulation:

$$\mathbf{A} \cdot \vec{x} = \vec{b} \quad (2.3.16)$$

where  $\mathbf{A}$  is a  $n \times n$  matrix and  $\vec{x}$  and  $\vec{b}$  are  $n$ -dimensional vectors. Such a matrix has a storage cost of  $(n^2)$  and every matrix multiplication costs  $\mathcal{O}(n^2)$ . For the Poisson problem, the calculation volume is discretized by finite elements and the derivations are approximated by finite differences. Thus, the matrix of the Poisson problem is a sparse matrix, which means that most of the entries are zero. The non-zero elements are bounded and by using a sparse matrix formulation the storage and the computational costs can be reduced to  $\mathcal{O}(n)$ . [86] In the following part, the sparse matrix representation of the Poisson problem, as discussed in Section 2.3.1, is derived. Using Gauss's law on the Poisson equation yields (compare Equation 2.3.6):

$$\oint [\varepsilon(\vec{r}) \vec{\nabla} \varphi(\vec{r})] d\vec{A} = -\frac{Q}{\varepsilon_0}. \quad (2.3.17)$$

If the volume is discretized to  $N \times M \times L$  lattice points with distances between the points of  $h_j = H_j/j$ , for  $j = n, m, l$ , as shown in Figure 2.9, the surface integral can be numerically expressed by:

$$\sum_{i=2}^7 \tilde{\varepsilon}_i \cdot \frac{\phi_i - \phi_1}{h_i} \cdot h_\alpha h_\beta = -\frac{Q_1}{\varepsilon_0} \quad (2.3.18)$$

where  $i$  is the index of the six nearest neighboring elements, with  $i = 1$  for the center element.  $\tilde{\varepsilon}_i$  is the mean relative permittivity between the center element and the neighboring element  $\tilde{\varepsilon}_i = \frac{1}{2}(\varepsilon_1 + \varepsilon_i)$ .  $Q_1$  is the charge located at the center element with the distance  $h_i$  to the neighboring element with index  $i$ . The rectangular area  $A$  oriented perpendicular to  $h_i$  is spanned by  $h_\alpha$  and  $h_\beta$ , which can be eliminated by:

$$\sum_{i=2}^7 \tilde{\varepsilon}_i \cdot \frac{\phi_i - \phi_1}{h_i^2} \cdot h_\alpha h_\beta h_i = -\frac{Q_1}{\varepsilon_0} \quad \Rightarrow \quad \sum_{i=2}^7 \tilde{\varepsilon}_i \cdot \frac{\phi_i - \phi_1}{h_i^2} = -\frac{\rho_1}{\varepsilon_0} \quad (2.3.19)$$

where  $\rho_1$  is the charge carrier density inside the volume element  $V$ .

One can see, that the Poisson problem reduced to interactions with the next neighbors of each node, which can be expressed by a 7-point stencil. To create a sparse matrix, lexicographical indexing is used:

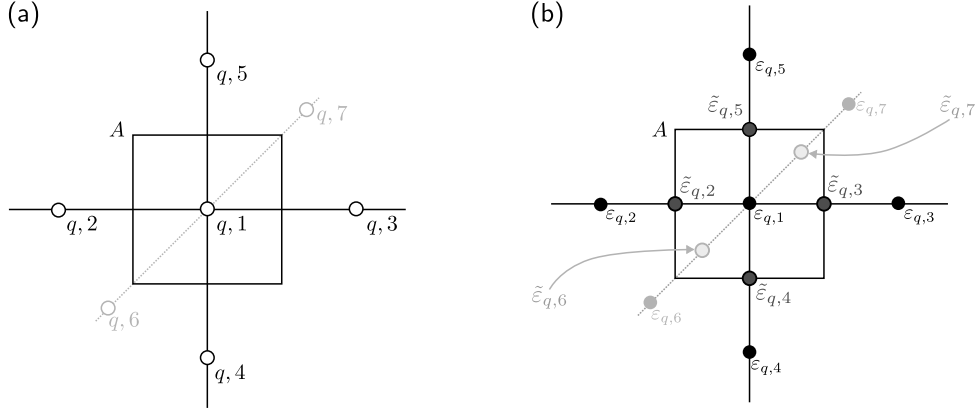


**Fig. 2.9** Schematic of the discretized volume lattice for the Poisson model. (a) Three-dimensional lattice of location  $q,1$  with its neighbors  $q,i$  with  $i \geq 2$ . (b) Three dimensional lattice of relative permittivities  $\varepsilon_{q,i}$  and the mean permittivities  $\tilde{\varepsilon}_{q,i}$  located in the middle between neighboring lattice points on the surface  $A$ .

$$\phi = (\phi_{111}, \phi_{211}, \dots, \phi_{N11}, \phi_{N21}, \dots, \phi_{NM1}, \phi_{NM2}, \dots, \phi_{NML}). \quad (2.3.20)$$

The corresponding Poisson matrix has only seven nonzero entries in each row, due to the defined 7-point stencil. Nevertheless, the full matrix representation is never required, as a pointer vector later describes the geometry of the problem. Finally, the Poisson problem with sparse matrix formulation can be expressed as:

$$\sum_i^7 g_{q,i} \cdot \phi_{c_{q,i}} = -\frac{\rho_q}{\varepsilon_0}, \quad \forall q \in [1, 2, \dots, NML] \quad (2.3.21)$$

where  $g_{q,i}$  describes the physical properties with:

$$g_{q,1} = -\sum_{i=2}^7 \frac{\tilde{\varepsilon}_i}{h_i^2} \quad \text{and} \quad g_{q,i} = \frac{\tilde{\varepsilon}_i}{h_i^2}, \quad \forall i \geq 2 \quad (2.3.22)$$

and  $c_{q,i}$  is the pointer for the lexicographical indexing of the neighboring elements  $i$  for position  $q$ :

$$c_{q,i} = (q, q-1, q+1, q-N, q+N, q-N \cdot M, q+N \cdot M). \quad (2.3.23)$$

The solution of the Poisson problem can then be found by numerical iterative methods. The methods used within this work are described in the following sections.

### 2.3.3 Newton's Method

The Newton's method is an iterative algorithm for finding the root of a function  $f(x)$ . It successively approximates the root with increasing accuracy for each loop. For a one-dimensional problem, the basic principle relies on fitting a tangent to the function  $f(x)$  at

starting point  $x = x^{(0)}$  and finding the intersection of the tangent with the x-axis. The x-value of the intersection  $x^{(1)}$  is then used for fitting a new tangent at  $f(x^{(1)})$ . This procedure is repeated until a termination criterion is fulfilled. The method works quite similar for a three-dimensional, non-linear system of equations, which can be expressed by:

$$\vec{F}(\vec{x}) = 0 \quad (2.3.24)$$

where  $\vec{F}$  describes a system of  $N$  equations and  $\vec{x}$  is the solution vector to fulfill Equation 2.3.24. The function  $\vec{F}$  can be expanded in a Taylor series around a starting value  $\vec{x}^{(0)}$ :

$$\vec{F}(\vec{x}) = \vec{F}(\vec{x}^{(0)}) + \vec{F}'(\vec{x}^{(0)}) \cdot (\vec{x} - \vec{x}^{(0)}) + o(|\vec{x} - \vec{x}^{(0)}|) \quad \text{for } \vec{x} \rightarrow \vec{x}^{(0)} \quad (2.3.25)$$

where  $\vec{F}'(\vec{x})$  is the Jacobi matrix  $J_F(\vec{x})$ . If the Taylor series is truncated after the linear expansion, it can be rewritten as:

$$\vec{F}(\vec{x}) = \vec{F}(\vec{x}^{(0)}) + J_F(\vec{x}^{(0)}) \cdot (\vec{x} - \vec{x}^{(0)}) = \vec{F}(\vec{x}^{(0)}) + J_F(\vec{x}^{(0)}) \cdot \delta\vec{x} \quad (2.3.26)$$

where  $\delta\vec{x}$  is defined as  $\delta\vec{x} = \vec{x} - \vec{x}^{(0)}$ . The root  $\vec{x}^{(1)}$  of the linear expansion (Equation 2.3.26) is found by:

$$\vec{x}^{(1)} = \vec{x}^{(0)} - \frac{\vec{F}(\vec{x}^{(0)})}{J_F(\vec{x}^{(0)})} \quad (2.3.27)$$

provided that the Jacobi matrix  $J_F(\vec{x}^{(0)})$  can be inverted at the position  $\vec{x}^{(0)}$ . Thus, the iteration algorithm of the Newton's method then looks like [87]:

$$\vec{x}^{(m+1)} = \vec{x}^{(m)} - \frac{\vec{F}(\vec{x}^{(m)})}{\vec{F}'(\vec{x}^{(m)})} \quad \text{for } m = 0, 1, 2, \dots \quad (2.3.28)$$

where with every iteration  $m + 1$ , the Newton's algorithm provides better solutions  $\vec{x}^{(m)}$  to fulfill:

$$\vec{F}(\vec{x}^{(m)}) + J_F(\vec{x}^{(m)}) \cdot \delta\vec{x}^{(m+1)} = 0. \quad (2.3.29)$$

The termination condition is reached, if the difference  $\delta\vec{x}^{(m)} = \vec{x}^{(m)} - \vec{x}^{(m-1)}$  is smaller than the difference of the previous iteration  $\delta\vec{x}^{(m-1)}$  multiplied with an initially defined value  $0 < \xi < 1$  [87]:

$$\|\delta\vec{x}^{(m)}\| \leq \xi \|\delta\vec{x}^{(m-1)}\| \quad (2.3.30)$$

### 2.3.4 Successive Over-Relaxation Method

There are a couple of methods for solving a large system of equations such as  $\mathbf{A} \cdot \vec{x} = \vec{b}$ , where  $\mathbf{A}$  is a  $N \times N$  matrix,  $\vec{x}$  is the solution vector and  $\vec{b}$  a vector of constants. In case, that all diagonal entries of  $\mathbf{A}$  satisfy  $a_{ii} \neq 0$ , the Gauss-Seidel iteration can be applied. It is similar to the Jacobi method, with the difference that for every iteration the newest solution component is taken. The Gauss-Seidel method is defined as [86]:

$$x_i^{(m+1)} = \frac{1}{a_{ii}} \left[ b_i - \sum_{j=1}^{i-1} a_{ij} x_j^{(m+1)} - \sum_{j=i+1}^N a_{ij} x_j^{(m)} \right], \quad \text{for } i = 1, 2, \dots, N. \quad (2.3.31)$$

This representation can be rewritten as:

$$x_i^{(m+1)} = x_i^{(m)} - \frac{1}{a_{ii}} \left[ \sum_{j=1}^{i-1} a_{ij} x_j^{(m+1)} + \sum_{j=i}^N a_{ij} x_j^{(m)} - b_i \right], \quad \text{for } i = 1, 2, \dots, N, \quad (2.3.32)$$

with the only modification, that the lower boundary of the second sum starts at  $j = i$ . Nevertheless, Equation 2.3.32 shows that the new iteration  $x_i^{(m+1)}$  is governed by subtracting a correction from the previous  $x_i^{(m)}$ . By introducing a multiplication factor  $\omega$  for the correction term, the successive over-relaxation (SOR) method is obtained. It allows faster convergence as compared to the Gauss-Seidel method, if the  $\omega$  is chosen adequately. The SOR method can be written as [86]:

$$x_i^{(m+1)} = x_i^{(m)} - \frac{\omega}{a_{ii}} \left[ \sum_{j=1}^{i-1} a_{ij} x_j^{(m+1)} + \sum_{j=i}^N a_{ij} x_j^{(m)} - b_i \right], \quad \text{for } i = 1, 2, \dots, N, \quad (2.3.33)$$

where the over-relaxation factor  $\omega$  is in the range of  $1 < \omega < 2$ . If  $\omega$  is in the range  $0 < \omega < 1$  the successive under-relaxation method is obtained. In case of  $\omega = 1$ , Equation 2.3.33 is identical to the Gauss-Seidel method. For the Poisson problem, which can be expressed by sparse matrix of finite-differences (compare Section 2.3.2), a good value for  $\omega$  is given by [86]:

$$\omega = \frac{2}{1 + \sin(\pi \cdot h)} \quad (2.3.34)$$

where  $h$  is the step size  $h = 1/N$  of the  $N \times N$  matrix. Similar to the Newton's method, the iteration of the SOR method is stopped, when a previously defined value  $\xi$  is larger than  $\Delta x$ , which is simply defined as  $Ax - b = \Delta x$ . [86]

### 2.3.5 Poisson Solver Algorithm

The goal of the Poisson solver algorithm is to obtain a self-consistent solution of the Poisson equation inside a large model volume. The algorithm's flowchart is shown in Figure 2.10. In

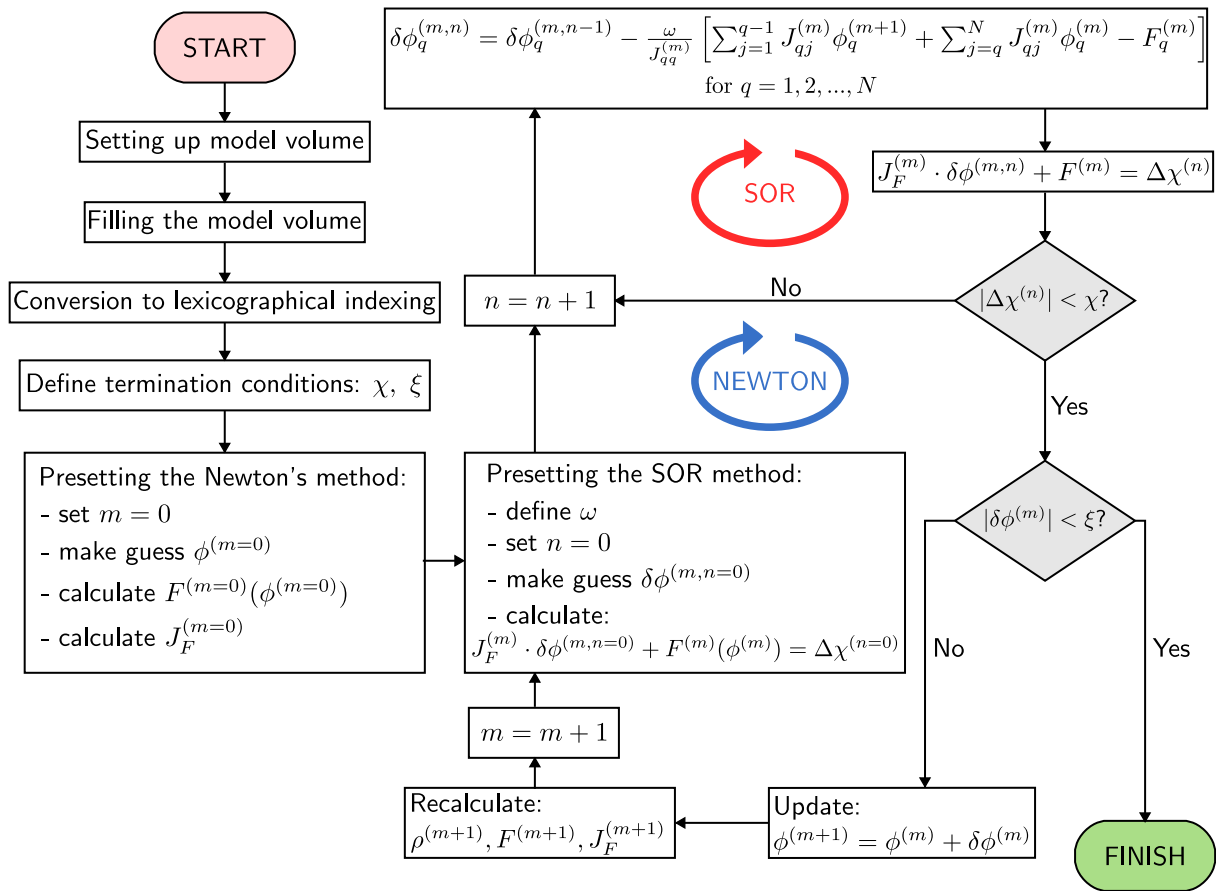


**Fig. 2.10** Flowchart of the Poisson solver algorithm.

the first step, the model volume is set up. This volume is filled with information of the layers such as the number of layers, type of material, thickness of the layers, layer topographies, the work functions as well as the boundary conditions for the Poisson equation (e.g. metal contacts have Dirichlet condition) and the layers' externally applied bias. In the next step, the Poisson problem inside the volume is formulated by a sparse matrix representation using lexicographical indexing (compare Section 2.3.2). Before the loop is started, the termination conditions are defined and the Newton's method is preset. Therefore, a first guess of the potential  $\phi^{(m=0)}$  is defined, the first guess of the root of the Poisson problem  $F^{(m=0)}$  is calculated using

$$F_q^{(0)} = \sum_{i=2}^7 \frac{\tilde{\varepsilon}_i \varepsilon_0}{h_i^2} \phi_{q,i}^{(0)} - \phi_{q,1}^{(0)} \sum_{i=2}^7 \frac{\tilde{\varepsilon}_i \varepsilon_0}{h_i^2} - \rho(\phi_q^{(0)}) \quad (2.3.35)$$

as derived in Section 2.3.2 and the corresponding Jacobian  $J_{F_q}^{(m=0)} = J_q$  is determined via

$$J_{q,1}^{(0)} = \frac{\partial F_q^{(0)}}{\partial \phi_{q,1}^{(0)}} = - \sum_{i=2}^7 \frac{\tilde{\varepsilon}_i \varepsilon_0}{h_i^2} + \frac{\partial}{\partial \phi_q^{(0)}} \rho(\phi_q^{(0)}), \quad \text{for } i = 1 \text{ and} \quad (2.3.36)$$

$$J_{q,i}^{(0)} = \frac{\partial F_q^{(0)}}{\partial \phi_{q,i}^{(0)}} = \frac{\tilde{\varepsilon}_i \varepsilon_0}{h_i^2}, \quad \text{for } i = 2, 3, \dots, 7 \quad (2.3.37)$$

with

$$\frac{\partial}{\partial \phi_q^{(0)}} \rho(\phi_q^{(0)}) = \frac{\partial}{\partial \phi_q^{(0)}} \pm e N_{eff} \mathcal{F}_{1/2}(\eta_q^{(0)}) = \pm e N_{eff} \mathcal{F}_{-1/2}(\eta_q^{(0)}) \quad (2.3.38)$$

as deduced in Section 2.3.1. To obtain the next better approximation of the potential  $\phi^{(m+1)}$ , the correction  $\delta\phi^{(m)}$  has to be calculated. This is done by solving

$$F(\phi_q^{(m)}) + J_F(\phi^{(m)}) \cdot \delta\phi^{(m)} = 0 \quad (2.3.39)$$

with the help of the SOR method, as described in Section 2.3.4. Then, the potential is updated:

$$\phi^{(m+1)} = \phi^{(m)} + \delta\phi^{(m)}. \quad (2.3.40)$$

With  $\phi^{(m)}$  the charge carrier density is updated via

$$\rho(\phi_q^{(m)}) = \pm e N_{eff} \mathcal{F}_{-1/2}(\eta_q^{(m)}). \quad (2.3.41)$$

Afterwards, the root (Equation 2.3.35) is recalculated using

$$F_q^{(m)} = \sum_{i=2}^7 \frac{\tilde{\varepsilon}_i \varepsilon_0}{h_i^2} \phi_{q,i}^{(m)} - \phi_{q,1}^{(m)} \sum_{i=2}^7 \frac{\tilde{\varepsilon}_i \varepsilon_0}{h_i^2} - \rho(\phi_q^{(m)}) \quad (2.3.42)$$

as well as the Jacobian  $J_q^{(m)}$  according to Equations 2.3.36-2.3.38. At the end of the loop, it is checked whether the termination condition is fulfilled. If so, the loop is ended, otherwise, the counter  $m$  is increased and the next iteration is conducted.

The presented algorithm has been developed within the working group of Prof. Dr. Roland Kersting at the Ludwig-Maximilians-University of Munich. It has already been used to investigate screening phenomena within accumulation layers of molecular semiconductors as described in Reference [88].

# 3 Experimental Methods

This chapter covers the most important methods for sample fabrication and characterization used in this work. Processes for thin film deposition as well as the basic device architecture are discussed in Section 3.1. Techniques used for topographical and electrical characterization are addressed in Section 3.2.

## 3.1 Sample Fabrication

All devices are fabricated using thin-film deposition processes. Physical vapor deposition (PVD) is used for depositing metallic as well as molecular semiconductor (MSC) layers by thermal evaporation (compare Section 3.1.1). The insulating parylene-N layer is evaporated via a chemical vapor deposition (CVD) process which is depicted in Section 3.1.2. The fabrication of polymer layers such as for example polystyrene is done by spin coating and is explained in Section 3.1.3. At the end of this part, in Section 3.1.4, the basic architecture of the thin-film devices investigated within this work is presented.

### 3.1.1 Physical Vapor Deposition

Different PVD techniques exist such as electron-beam PVD or thermal evaporation. Throughout this work thermal evaporation PVD is used, where material is evaporated from solid form into atoms or molecules by heating. The particles move ballistically through high vacuum to the substrate, where they form thin layers with deposition rates of a few Å/s up to thicknesses in the nanometer range. [89]

In this work, PVD is used for depositing metallic layers such as chromium (Cr), gold (Au) or molybdenum oxide (MoOx) as well as for depositing molecular semiconductors. The whole process takes place inside a vacuum chamber. A schematic of the PVD chamber is shown in Figure 3.1. The substrate is placed upside-down in the upper part of the chamber. Shadow-masks are used to define the geometry of the deposited layers. The substrate holder inherits a PT1000 temperature sensor, a halogen light bulb for heating and a liquid nitrogen tube for cooling. Multiple sources of deposition materials are situated at the bottom of the chamber. For the evaporation of the metals, high temperatures  $T > 1000\text{ }^\circ\text{C}$  are necessary. Therefore, the boats for Cr, MoOx and Au are made from tungsten and resistive heating is used. The applied currents are in the range of 30 to 50V. For the chromium deposition, a chrome plated tungsten rod is used. In the case of molybdenum oxide a  $\text{Al}_2\text{O}_3$ -coated tungsten boat

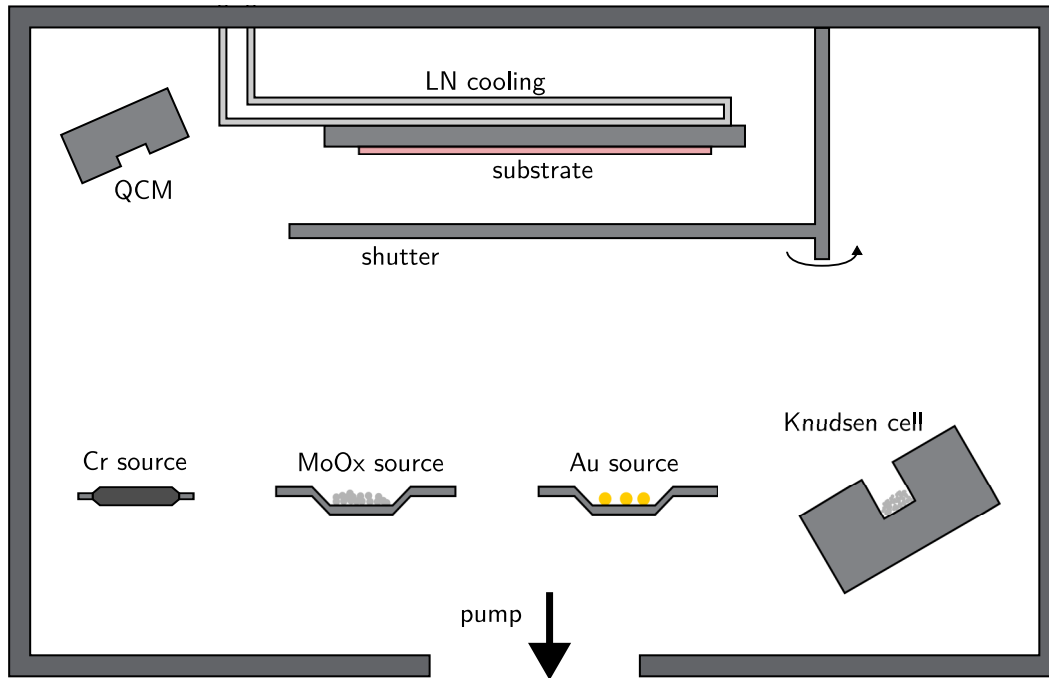


**Fig. 3.1** Schematic of the PVD evaporation chamber. The substrate (pink) is mounted on top facing upside-down. The substrate holder can be actively cooled via liquid nitrogen tubes. The shutter is situated between the substrate and the evaporation sources to prevent the sample from unwanted deposition. Next to the substrate, the quartz crystal microbalance is mounted, which serves as a thickness monitor. The different evaporation sources for Cr, MoOx, Au and the molecular semiconductor are placed on the bottom.

is filled with MoOx powder and for gold, a non-coated tungsten boat is filled with Au-pellets. MSCs evaporate at temperatures between 150 to 400°C. For this reason, evaporation cells made from alumina are used. The design resembles to that of Knudsen cells [90], therefore the term "Knudsen cell" is used throughout this work. The MSC powder is filled into a cylindrical hole inside the middle of the alumina. This geometry suppresses abrupt depositions of large amounts of semiconductor. For each type of semiconductor a distinct Knudsen cell has been manufactured to reduce cross-contamination between distinct depositions. The Knudsen cell is heated via a halogen light bulb. A PT1000 sensor is mounted inside the alumina cell, which allows to precisely control the temperature throughout the process. A shutter is situated between the sources and the substrate to minimize contamination and to exclude unwanted deposition. A stepper motor can move the shutter out of the way to control the start and stop of the deposition process. To monitor the evaporation thickness a quartz crystal microbalance (QCM) is situated next to the substrate. By knowing the density of the material which is evaporated, the deposited thickness can be monitored within sub-Ångström resolution.

After filling the chamber and closing the door a rotary vane pump generates a low pressure of  $p < 1$  mbar. Afterwards, a turbo molecular pump is started, with which base pressures of

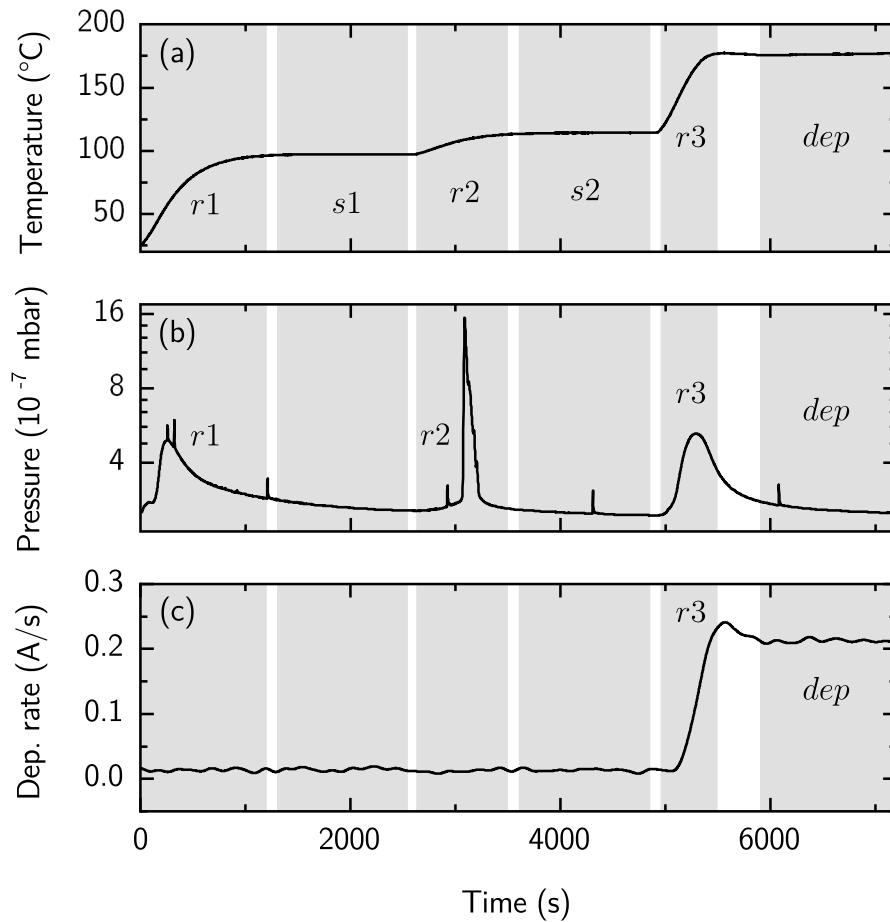


**Fig. 3.2** Exemplary evolution of relevant parameters during the PVD processing of a MSC. Temperature over time is plotted in (a), the chamber pressure in (b) and the deposition rate in (c). The process is divided into six different steps: three ramps ( $r1$ ,  $r2$ ,  $r3$ ) two soaks ( $s1$ ,  $s2$ ) and the deposition ( $dep$ ).

$p_{base} \approx 10^{-7}$  mbar can be reached. In such pressure regimes, the particles' mean free path is in the range of kilometers (compare Appendix A.1). Therefore, collisions between atoms inside the chamber are very unlikely and ballistic transport can be assumed. The pressure is measured and monitored by a pressure gauge (not shown in Fig. 3.1). The deposition process for metals is generally identical to that for MSCs. Figure 3.2 shows an exemplary evolution of the deposition parameters, such as the temperature (Fig. 3.2 (a)) of the Knudsen cell (current in case of metal deposition), the pressure inside the chamber (Fig. 3.2 (b)) and the deposition rate (Fig. 3.2 (c)). The deposition process is divided into three different parts. The first and the second part are for cleaning the evaporation source and getting rid of impurities. The third part is the actual evaporation. Each part inherits a ramping step. A ramp is the gradual increase of the temperature or current until a defined value is reached. In Figure 3.2 the ramps are denoted with  $r1$ ,  $r2$  and  $r3$ . During the ramp, the

pressure inside the chamber rises (compare Fig. 3.2 (b)) due to evaporation of water and other contaminants. A subsequent soaking step after ramp 1 and ramp 2 results in a decrease in pressure while the temperature of the source is held constant. The soaks are denoted with  $s_1$  and  $s_2$  in Figure 3.2. For the MSC deposition the soaks usually have a duration of 2000 s and for the metals 120 s, each. After the second soak  $s_2$  the final ramp  $r_3$  increases the temperature of the source until the deposition rate approaches its desired value in the range of 0.1 to 0.4 Å/s. After some time, the pressure decreases again while the deposition rate stays constant. The shutter is opened and the deposition process starts, denoted with  $dep$  in Figure 3.2. When the desired thickness is reached, the shutter is closed and the process is finished.

During the deposition of metallic contact layers, its surface resistance can be measured. The evaporation process is stopped, if the resistance value drops below a certain threshold. Therefore, thin cables are bonded to the samples' corners with silver conductive paint and feed-through to the outside of the chamber, where they are connected to a handheld ohmmeter. Detailed information on the specific layer thicknesses can be found in Section 3.1.4. For cleaning purposes the chamber can be heated to over 100 °C via halogen lamps which are situated at the side walls. Additionally, the substrate can be heated to ensure the absence of water molecules and other contaminants on the substrates' surface. These cleaning steps are usually conducted between distinct evaporation processes.

### 3.1.2 Chemical Vapor Deposition

Chemical vapor deposition (CVD) is a thin-film deposition technique which, instead of PVD, involves chemical reactions of the precursors in the gas-phase, on the substrate or both. Achievable film thicknesses range from a few nanometers to hundreds of micrometers [91]. CVD is used for the fabrication of dielectric layers [92], protective coatings [93], semiconductor films [94], diffusion barriers [95] and many more.

Here, the CVD-process is used for the deposition of the polymeric dielectric poly-para-xylylene (parylene-N), which works as an insulator layer. Besides a good transparency for THz radiation and a dielectric constant of  $\epsilon_{paN} = 2.6$  [96], parylene-N (paN) exhibits a huge dielectric strength of  $\geq 2.8$  MV/cm [97] allowing the injection of large charge carrier densities in the range of  $n_{2D} > 2 \times 10^{12}$  1/cm<sup>2</sup>. Furthermore, the deposition of paN results in a pinhole-free and conformal coating with the ability to withstand multiple temperature cycles between 4.2 K and 300 K [98].

The polymeric paN is synthesized via the Gorham method [99] as shown in Figure 3.3. At temperatures above 600 °C the dimere di-para-xylylene is split up into monomeres of para-xylylene via pyrolysis. On surfaces with temperatures lower than 30 °C the monomeres polymerize and form poly-para-xylylene. Figure 3.4 shows a schematic of the CVD system used in this work. It consists of two ovens, an evaporation chamber, a cooling trap and a vacuum pump. All is connected via tubes including three valves to control the process. The substrate holder can be heated via halogen lamps (not shown in Fig. 3.4) and cooled

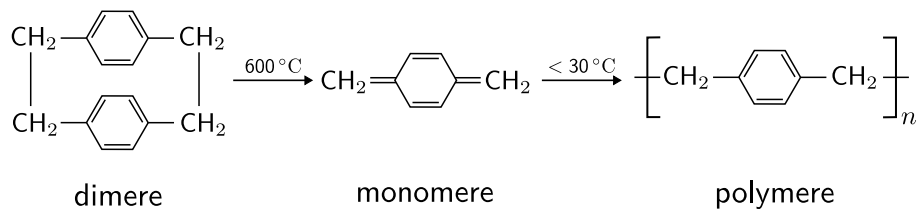


**Fig. 3.3** Synthesis route of PaN as described by Gorham [99].

by a water cooling system. Before the process starts, the paN precursor is loaded into the sublimation oven, the substrate is placed on top of the substrate holder and valve A is closed while valve B and valve C are open. A precursor mass of 1.5 g is enough to fabricate layers of thicknesses up to 500 nm. Then, the system is evacuated to a pressure of  $10^{-2}$  mbar. The substrate holder is heated up to  $\approx 100^\circ\text{C}$  for about 30 minutes to get rid of residual water on top of the sample. Afterwards, the sample is cooled down to  $11^\circ\text{C}$ . The sublimation oven is warmed up to  $120^\circ\text{C}$  leading to the evaporation of the precursor. The dimers travel through the tube system into the  $660^\circ\text{C}$  pyrolysis oven. The dimers split up into monomers, as outlined in Figure 3.3. To start the deposition process valve B is closed and valve A is opened. Now, the monomers travel into the evaporation chamber and polymerize at the cold sample surface. The thickness is monitored via the thin-film interference effect.

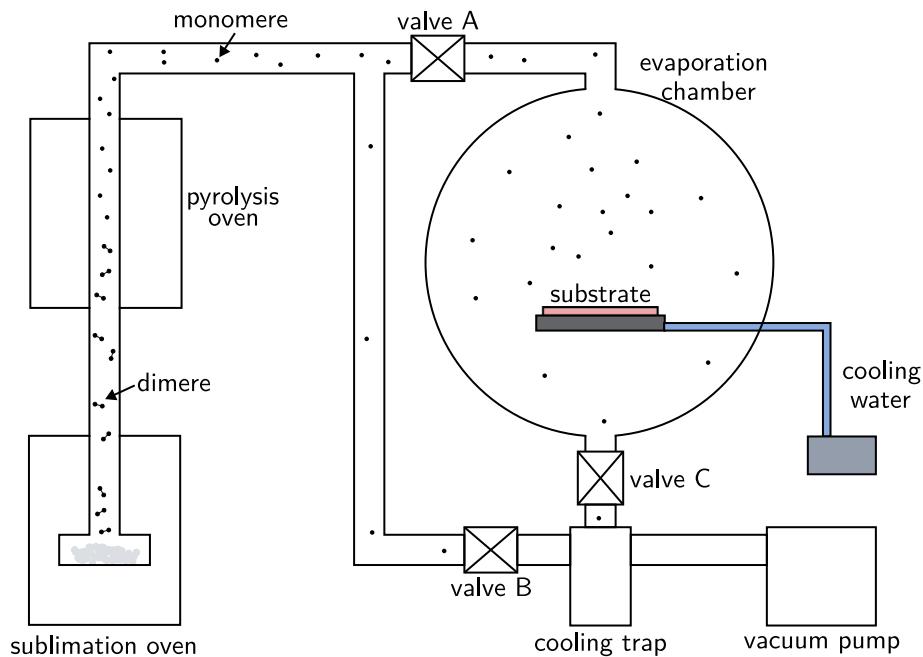


**Fig. 3.4** Schematic of the chemical vapor deposition system used in this work. It consists out of a sublimation oven, a pyrolysis oven and an evaporation chamber which are connected via tubes and separated by valves. The whole system is operated in vacuum with a pressure of  $\approx 20 \mu\text{bar}$

Color changes are observed and can be correlated to the deposited thickness using Fresnel equations. With the refractive index of paN  $n_{paN} = 2.6$  the thickness upon specific color changes can be determined quite accurately within  $\pm 20$  nm, which has been confirmed using tactile measurements such as atomic force microscopy and profilometry. A calculation and a thickness table can be found in Appendix A.2.

The deposition rate strongly depends on the substrate temperature and is normally in the range of 3 to 6 nm/min. To withstand voltages of up to 70 V, final thicknesses of paN between 250 nm to 350 nm are deposited.

### 3.1.3 Spin Coating

Another possibility for the deposition of uniform films is spin coating from dilute solutions. It allows the fabrication of thin films with thicknesses of a few nanometer to several micrometers [100]. Besides the application for photoresist layer deposition [101], it can also be used to form thin layers of organic semiconductors [60] or for functionalization [102] and planarization of surfaces [103].

The basic principle relies on the distribution of a solution on a sample surface via centrifugal force while spinning the substrate at a high number of rotations per minute (rpm) with subsequent evaporation of the solvent. Properties of the solution such as viscosity, evaporation rate and concentration as well as process parameters like acceleration and rotation speed influence film thickness and surface properties. Four distinct steps of the spin coating process are shown in Figure 3.5 (a-d). In the first step, the fluid is dispensed onto the substrate surface as depicted in Figure 3.5 (a). The amount of volume which has to be deposited depends on the viscosity of the solution. Optimally, the whole surface of the substrate is covered with the solution during this dispense step. Mostly, the fluid is dispensed while the substrate remains static. In case of bad wetting behavior of the solution on the substrate, dynamic dispense at rotation speeds of about 500 rpm can be applied. The second step is the rotational acceleration of the substrate (compare Figure 3.5 (b)) which leads to a quick expulsion of the fluid. Initially, the upper layers of the fluid cannot follow the quick rotation due to its inertia. After some time the viscous shear drag equals the rotational acceleration. In the third step, the substrate is being spinned at a constant rpm-value. Fluid viscous forces subsequently reduce the thickness. Thus, changing of interference colors on the substrate can be observed. As this process is slowing down over time, the fourth step is reached, which is dominated by the evaporation of the solvent (compare Figure 3.5 (d)). This step can be supported by an annealing step, where the substrate is placed on top of a hotplate. [104] In this work, a *WS-400BZ-6NPP Lite* spin coater by *Laurell* is used for the planarization of the parylene-N insulator with poly(methyl methacrylate) (PMMA) or polystyrene (PS). The properties of the coating solutions can be read in Table 3.1.

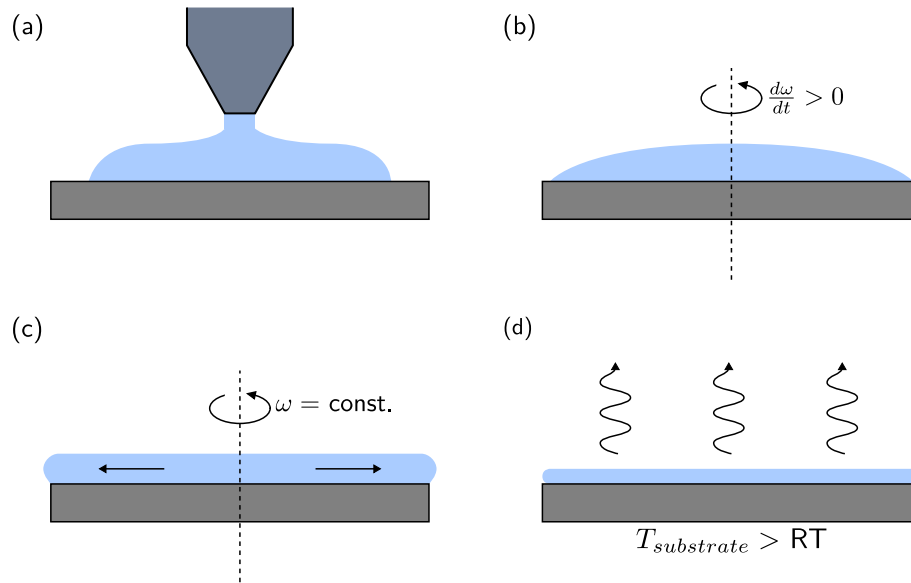


**Fig. 3.5** Typical phases during the spin coating process: (a) dispense of fluid, (b) acceleration with abrupt fluid expulsion, (c) fluid thinning under constant spinning rate and (d) evaporation of the solution solvent.

material	solvent	concentration
polystyrene (PS)	toluene	1.5%wt
poly(methyl methacrylate) (PMMA)	1,2-dichlorbenzene	2%wt

**Table 3.1** Properties of the spin coating solutions used for planarization of the parylene-N insulating layer.

For the fabrication of the samples within this work, a two step spin coating process has been applied. In the first step, the substrate is spun at  $\omega_1 = 500$  rpm for 5 s. During this time the coating solution is dispensed onto the sample. In the second step, the rotation speed is increased to  $\omega_2 = 3000$  rpm with an acceleration of 1100 rpm/s. After 50 s the spin coating is finished. The samples are put onto a 140 °C hotplate for at least one hour. Thicknesses of approximately 80 nm for PS and 120 nm for PMMA are achieved.

### 3.1.4 Device Architecture

The devices fabricated within this work exhibit a coplanar geometry. The term coplanar originates from the planar contacts which sandwich the active layer of the sample. The fabrication is done layer by layer, where each film is subsequently deposited via PVD (compare Section 3.1.1) or CVD (compare Section 3.1.2). The schematic architecture can be seen in Figure 3.6 (a). As a substrate a 0.5 mm thick sapphire dice with dimensions of 10 × 10 mm or a 125 μm thick polyethylene naphthalate (PEN) foil (Teonex<sup>®</sup> by Teijin DuPont Films<sup>TM</sup>)

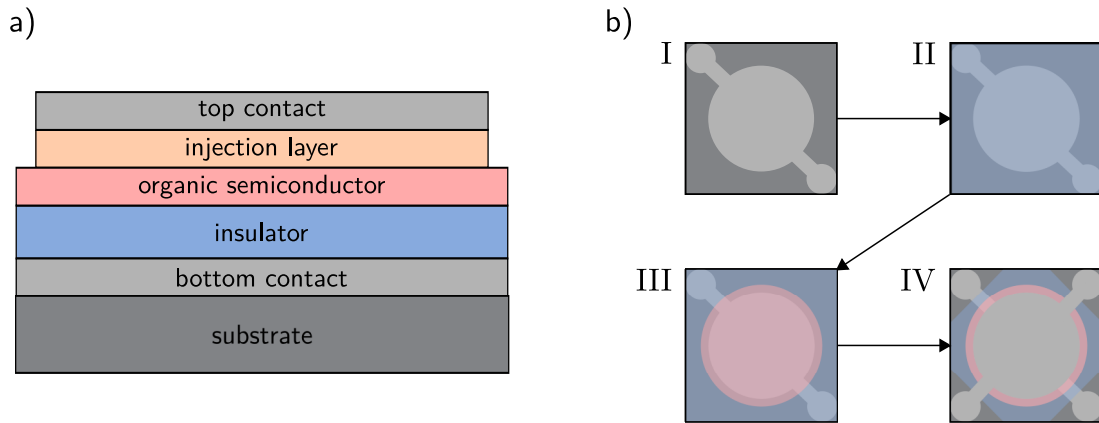


**Fig. 3.6** Schematic of the device architecture. Sketch of the side-view of the coplanar layer structure (a). Top-view drawing of the distinct fabrication steps (b). I: after bottom contact evaporation. II: after paN deposition. III: after PVD of the MSC. IV: after the removal of paN from the corners and the evaporation of the top contact.

is used. The PEN foil allows for the parallel fabrication of up to 16 samples. Nevertheless, sapphire as a substrate is crucial for frequency resolved THz spectroscopy measurements, as the resonance frequency of internal reflections inside PEN foil lies within the THz band. Sapphire samples are also favored for temperature dependent measurements, due to the superior heat conductivity of sapphire in comparison to PEN.

The bottom contact is a 6 nm thick film of chromium deposited via PVD (compare Section 3.1.1). The geometry of the bottom contact is composed of three circular shapes connected by a stripe as can be seen in Figure 3.6 (b)-I. The large circle in the middle defines the active area, the other two smaller circles are for contacting.

Subsequently, the whole sample is covered with 250 nm thick layer of the paN insulator, as shown in Figure 3.6 (b)-II, via CVD (compare Section 3.1.2). The paN surface can be planarized by spin coating polystyrene or poly(metha methacrylate) (compare Section 3.1.3), which leads to a reduction of the surface roughness from 5 nm to 1 nm. During the next step, as shown in Figure 3.6 (b)-III, the organic semiconductor is deposited by PVD through a circular shadowmask. The thickness of the MSC layer is in the range of 25 nm to 50 nm. Next, the paN is removed from the corners of the sample. Finally, the injection layer (Au or MoOx) and the top contact (Cr) are evaporated by PVD. The top contact geometry is identical to the bottom contact layout but rotated by 90° (compare Figure 3.6 (b)-IV). During the top contact deposition, the sample is cooled down to approximately 0 °C as excessive heat stress can lead to structural changes of the MSC layer, especially for MSCs with low melting points. Therefore, liquid nitrogen is pumped through the cooling tubes of the PVD which are in contact to the sample holder. The thickness of the top contact is monitored via the sheet resistance across the surface. An exemplary thickness-resistance curve is depicted in Figure 3.7. Here, the ideal case is shown, where a 7 nm Cr layer exhibits a sheet resistance

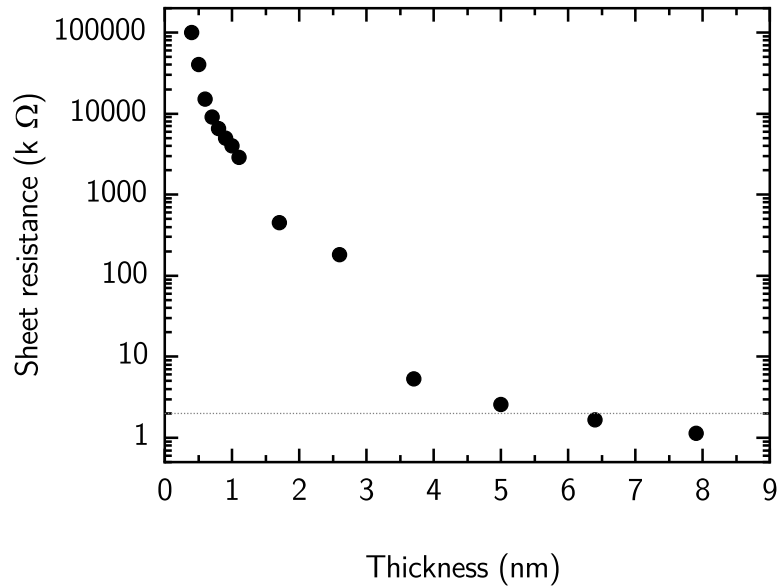


**Fig. 3.7** Exemplary data of the measured sheet resistance over the deposited Cr thickness during of top contact evaporation. The resistance quickly drops over several magnitudes with an increase of a few nanometer of Cr. The curve saturates after 5 nm to 6 nm. The dotted line at 2 kΩ marks the desired resistance value which is reached at Cr thicknesses of 7 nm.

of 2 kΩ. This is a good trade-off between a thin metallic layer for low reflection of the THz pulse and a high contact conductivity to ensure full percolation and small RC time constants during the charge injection. An example for a non-ideal case and its reasons is discussed in Appendix A.3.

In the last step, the corners of the device are covered by an additional layer of gold with a thickness of approximately 40 nm. These strengthening gold pads allow for good and repeatable contacting of the device via gold spring contacts.

## 3.2 Device Characterization

Besides the fabrication of the samples, which has been extensively described in the previous sections, the characterization of the devices is crucial and provides useful insight into the physics. During this work, atomic force microscopy is applied to gather information on surface topographies. The basic principle and the experimental setup of the atomic force microscope as well as how its data can be interpreted is discussed in Section 3.2.1. Furthermore, methods such as the measurement of resistance, capacitance and current-voltage curves are used for the electrical characterization of the investigated samples. Electrical characteriza-

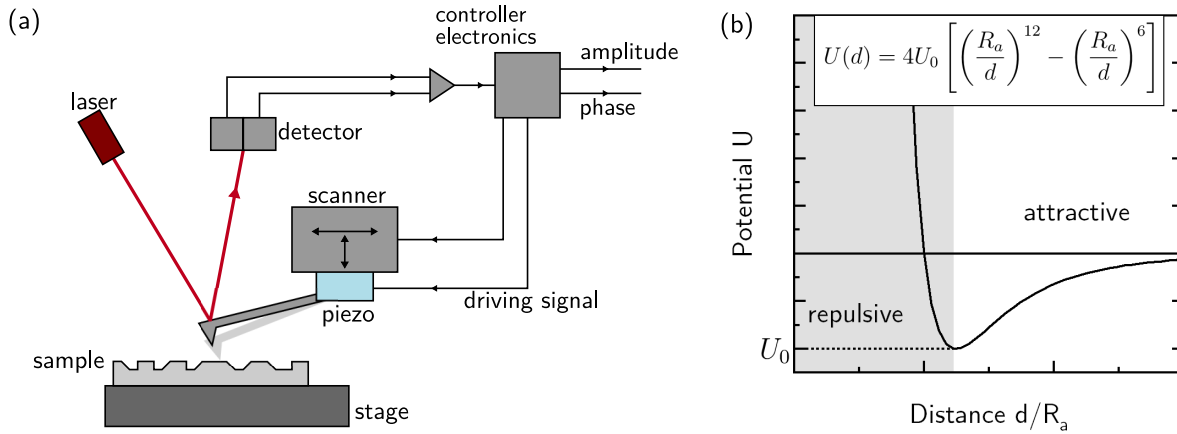


**Fig. 3.8** Schematic working principle of tapping-mode AFM (a). Schematic graph of the Lennard-Jones potential (b).

tion is necessary for the calculation of the charge carrier density and gives valuable feedback for improving the fabrication procedure. Section 3.2.2 covers the electrical characterization routines applied within this work.

### 3.2.1 Atomic Force Microscopy

Atomic force microscopy (AFM) is a technique which allows to gather topographical information of a specimen with resolution in the nanometer regime. The schematic setup and working principle is shown in Figure 3.8. The basic concept relies on the distance dependent force  $F(d)$  between an atomically sharp tip and the sample surface. By scanning the tip across the sample a two-dimensional image is obtained. The total force is composed of several contributions such as the long-range ( $d > 1$  nm) van der Waals force and short-range ( $d > 1$  nm) forces arising from the overlap of electron wave functions of the outermost shells. The potential over the tip-sample distance can be modeled by the Lennard-Jones potential, as depicted in Figure 3.8 (b). It consists of a repulsive interaction for small distances and an attractive part for large distances. [105]

The basic setup of a tapping mode AFM is depicted in Figure 3.8 (a). The tip is situated at the end of a flat spring (cantilever), which is being deflected in dependence of the distance between tip and specimen. The deflection is measured by the position of a laser beam which is reflected from the back of the cantilever onto a four-split photodiode. Different operating modes are possible, but within this work tapping mode has been applied. The cantilever is therefore mounted onto a piezoelectric actuator which drives the cantilever to oscillate close to its resonant frequency in the range of a few hundred kHz with a large amplitude ( $\approx 50$  nm). Due to interactions of the tip with the sample, the oscillation amplitude changes monotonously with the tip-sample distance. Overall, tapping mode allows besides a robust feedback loop, high-resolution imaging of even soft samples and gives contamination layer

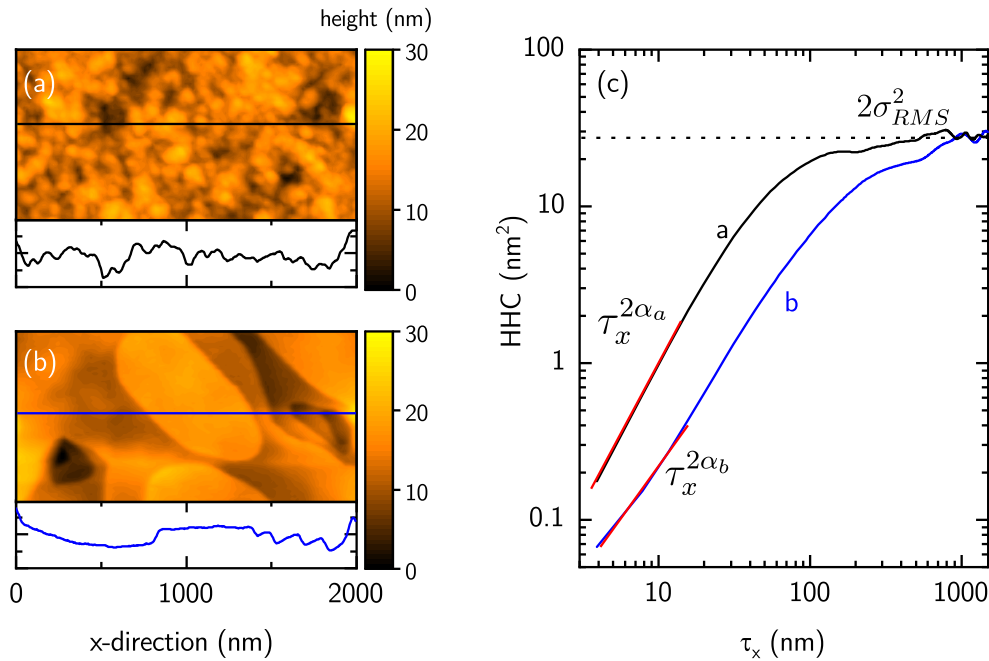


**Fig. 3.9** Exemplary AFM images (a) and (b) of fundamentally different topographies with identical RMS roughness  $\sigma$ . Comparison of HHCs of the two AFM images (c).

independent results in ambient conditions. [105]

The resolution of the generated two-dimensional scans strongly depends on the operation of the AFM, as many parameters can be adjusted. This final image resolution can be determined by the systems' response to a sharp edge (edge response). The distance required for the systems' response to rise from 10% to 90% corresponds to the resolution of the image [106]. Within this work, all AFM images exhibit a spatial resolution of at least 30 nm. With this resolution, all features relevant for this work can be resolved. A corresponding edge response and its analysis can be found in Appendix A.4.

Exemplary AFM images are shown in Figure 3.9 (a) and (b). Such two-dimensional scans allow, besides the measurement of distinct feature dimensions, the determination of relevant statistical surface parameters. One key quantity is the root-mean-square (RMS) roughness  $\sigma_{RMS}$ . It describes the deviation of the surface height related to the mean height. The mean height  $\bar{h}$  is defined as [107]:

$$\bar{h} = \langle h(\vec{r}) \rangle = \frac{1}{N \cdot M} \sum_{i=1}^N \sum_{j=1}^M h(x_i, y_j) \quad (3.2.1)$$

with  $h(\vec{r})$  being the measured relative height at position  $\vec{r} = (x, y)$  for a two-dimensional lattice with dimensions of  $N \times M$ . The RMS roughness  $\sigma_{RMS}$  is calculated by [107]:

$$\sigma_{RMS} = \sqrt{\langle [h(\vec{r}) - \bar{h}]^2 \rangle}. \quad (3.2.2)$$

Nevertheless, the RMS roughness inherits no information on the local surface roughness. Fundamentally different topographies can exhibit the same RMS roughness as it is the case for the AFM micrographs (a) and (b) shown in Figure 3.9. Both exhibit an RMS roughness of  $\sigma_{RMS} = 3.6$  nm. However, the height-height-correlation (HHC) can be determined which relates the roughness to the spatial distance along the x-direction. It is defined as [108]:

$$HHC_x(\tau_x) = \frac{1}{M(N-m)} \sum_{i=1}^{N-m} \sum_{j=1}^M (h(x_{i+m}, y_j) - h(x_i, y_j))^2 \quad (3.2.3)$$

where  $\tau_x$  is the distance along the x-direction (fast scanning axis) and  $m = \tau_x/\Delta$  with  $\Delta$  being the sampling interval (distance between neighboring measurement points). HHC curves of the AFM images of Fig. 3.9 (a) and (b) are depicted in Figure 3.9 (c) and it can be seen that they exhibit different shapes. The HHC-curves can be split into two distinct segments which are separated by the knee of the curve corresponding to the correlation length  $\xi$ . In the regime of  $\tau_x < \xi$ , the HHC gives information on the local surface roughness and the local slope  $\alpha$  can be determined by fitting  $\tau_x^{2\alpha}$ . For  $\tau_x > \xi$  the curve saturates and the RMS roughness can be extracted by fitting  $2\sigma_{RMS}^2$ . Therefore, even though the distinct HHC-curves originate from surfaces with identical  $\sigma$  their shapes are fundamentally different. This makes the HHC an important tool for investigating AFM images to get valuable information of the surface properties of the sample. [107]

### 3.2.2 Electrical Characterization

During THz experiments, the voltage across the device is modulated. This voltage modulation leads to an injection of charge carriers into the semiconductor. The geometry of the device as well as the electrical characteristics determine the density of injected charge carriers, which is a crucial value for the accurate interpretation of the THz measurement data. Thus, electrical properties of the sample such as resistance, capacitance and leak-current have a big influence on the THz spectroscopy results. In this section, the methods used for electrical characterization prior to THz experiments are summarized.

#### Resistance

One of the relevant parameters is the resistance of the gate contact  $R_{gate}$  and the top contact  $R_{top}$ . It is measured between the corners of the contact with the help of an ohmmeter (MASTECH<sup>TM</sup>MY74). Both,  $R_{gate}$  and  $R_{top}$  should be in the range of a few k $\Omega$ . A large resistance is a hint for insufficient percolation of the contacts, for example due to a rough surface of the underlying layer. The insufficient percolation may result in inhomogeneous charge injection into the semiconductor. Resistances in the saturation regime of the thickness-resistance

curve (compare Figure 3.7) assure adequate percolation and RC-constants. Therefore, resistances of  $R_{gate}, R_{top} < 10 \text{ k}\Omega$  are sufficient. Most devices investigated within this work yield values of  $R_{gate}, R_{top} \approx 2 \text{ k}\Omega$ .

### Capacitance

Another crucial parameter is the capacitance  $C$  of the sample. It is determined by the permittivity  $\varepsilon$  of the insulating material (here: parylene-N), the insulator thickness  $d_{ins}$  and the active area  $A_{active}$  of the device, which is defined by the geometrical overlap between the top contact, the semiconducting layer and the gate contact. The devices' capacitance  $C$  can be calculated via [109]:

$$C = \varepsilon_0 \cdot \varepsilon \cdot \frac{A_{active}}{d_{ins}} \quad (3.2.4)$$

with  $\varepsilon_0$  being the vacuum permittivity and  $\varepsilon$  being the permittivity of the insulator (here:  $\varepsilon_{paN} = 2.6$  [97]). For a device with a paN thickness of 300 nm and an active area of  $0.2827 \text{ cm}^2$ , the capacitance should give a capacitance of 2.17 nF. The capacitance value is critical, as it is used to calculate the injected charge carrier density  $n_{2d}$ . The charge  $Q$  of a parallel plate capacitor with the applied voltage  $U$  can be calculated by  $Q = C \cdot U$  [109]. Thus, the two dimensional charge carrier density is determined via:

$$n_{2d} = \frac{Q}{e \cdot A_{active}} = \frac{C \cdot U}{e \cdot A_{active}} \quad (3.2.5)$$

with  $e$  being the elementary charge. The device's capacitance between the top contact and the gate contact is measured using a handheld LCR meter (Keysight™U1701B). Typical values of the investigated samples are in the range of 1.6 nF to 2.6 nF, depending on the thickness of the paN insulator and on whether the paN layer has been smoothed by an additional layer of PS or PMMA.

### IV-curves

Irregularities and contamination during device fabrication may result in non-uniform layers and pinholes within the insulator. These could lead to increased leakage current through the sample when a bias is applied, which results in a reduced charge carrier density. In general, the samples throughout this work are modulated with 50 V, which leads to an injected charge carrier density of  $2 \times 10^{12} \text{ 1/cm}^2$ . A leakage current of 1 nA corresponds to approximately  $6 \times 10^9$  electrons per second. The overall number of electrons inside the device is  $\approx 6 \times 10^{11}$  with a device area of  $0.3 \text{ cm}^2$ . This means, 1% of the injected charge carriers are lost due to a leakage current of 1 nA. However, the THz setups' sensitivity is much lower than 1% and thus this change in signal cannot be measured due to noise. Therefore, leakage currents in the range of  $I_{leak} < 1 \times 10^{-8} \text{ A}$  are acceptable. To make sure the devices exhibit no

considerably larger leakage the IV-curve is recorded. Therefore, the current through the device is measured while a voltage between the gate and top contact is gradually increased up to 50 V. An exemplary IV-curve is depicted in Figure 3.10. Here, a maximum current of  $\approx 5 \times 10^{-10}$  A assures a negligible leakage current and thus non-relevant charge loss during THz electromodulation spectroscopy measurements.

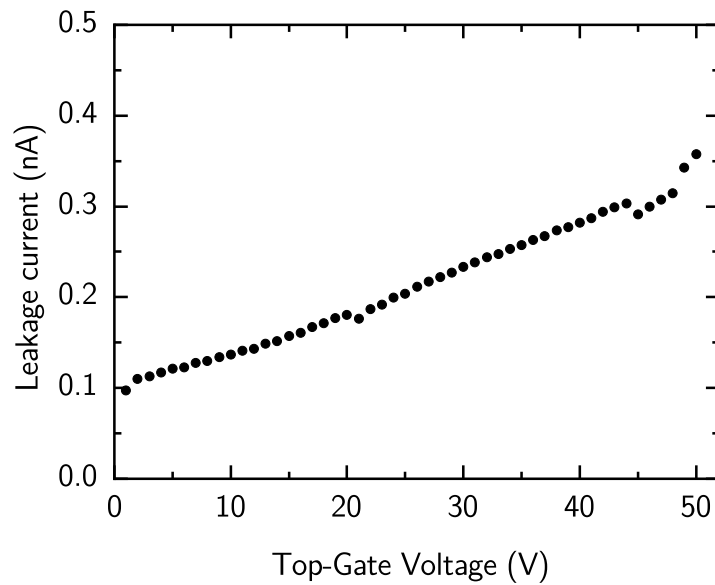


**Fig. 3.10** Exemplary IV-Curve of the leakage characteristics through the device.

## 4 Results

Diverse phenomena inside organic field-effect devices drastically limit the charge transport, which is the main research focus within this work. Moreover, the strength of THz electro-modulation spectroscopy for characterizing organic semiconducting materials is shown and is used to investigate such thin-film devices. Thus, in Section 4.1, the THz spectroscopy technique is thoroughly presented with respect to its application to organic thin-film devices. Special attention is given to the requirements of the investigated semiconductor structures as well as the limitations of the THz electromodulation technique.

The influence of the surface roughness on the charge distribution within the accumulation region is addressed in Section 4.2. As this impact cannot be examined solely by experimental means, self-consistent solutions of the Poisson equation give insight into fundamental transport processes within such field-effect devices.

Besides the insulator surface, the interface between the semiconductor and the contact material has a major impact on the device performance. How gold as injection material can lead to detrimental effects due to ion migration is investigated in Section 4.3.

At the end of this chapter, in Section 4.4, charge transport properties of small-molecule field-effect devices are investigated. Temperature-dependent measurements as well as frequency-resolved data are examined and give rise to the assumption that only a part of the injected charge carriers can contribute to band transport, while the majority is trapped or only performs hopping transport.

### 4.1 THz Electromodulation Spectroscopy for Organic Semiconductor Characterization

The understanding of the fundamental charge transport physics inside organic semiconductor devices is crucial for their future applicability. Most research within this field focuses on the investigation of transistor curves, which exhibit some severe drawbacks. On the one hand, the interpretation of the measurement data is very delicate and often leads to overestimation of the mobility [10, 11, 110]. On the other hand, several phenomena such as contact resistances [111] and grain boundaries [112] affect the overall conductivity and cannot be addressed individually.

Therefore, terahertz (THz) spectroscopy established as a powerful tool to study the intrinsic charge carrier dynamics of inorganic and organic semiconductors as the carriers' displacement occurs at a nanoscopic scale. Commonly, THz spectroscopy relies on optical-pump

excitation leading to the generation of multiple quasiparticles, e.g. excitons and polarons as well as charge carriers. Thus, the distinction of specific carrier dynamics is challenging. Furthermore, a quantitative interpretation of the conductivity data is delicate as it strongly depends on the density of charges, which can only be estimated or extracted by fitting the data. Additionally, comparison to field-effect devices is difficult as the carriers accumulate within a conducting channel near the insulator surface. Whereas in optically pump-probe THz spectroscopy, charges are generated within the bulk of the semiconductor. Thus, influence of a high density accumulation region as well as surface effects cannot be probed. [25] Here, THz electromodulation spectroscopy is presented, which is an alternative approach for investigating organic semiconductor thin-films. The injection of charge carriers is controlled via the modulation of the gate voltage. Therefore, electron and hole dynamics can be separately probed. The density of the injected charges can be precisely determined due to the devices' coplanar geometry. Furthermore, the comparably slow modulation frequency makes this method insensitive to phenomena arising from contact resistances. Moreover, charge transport within a conducting channel, as it is the case in field-effect transistors, is probed. Although, THz electromodulation spectroscopy measures tiny relative signals in the range of  $10^{-6}$  the presented setup exhibits a detection limit of  $\approx 1 \text{ cm}^2/\text{Vs}$ . Thus, most of today's relevant organic semiconductor materials can be investigated.

The applicability of THz electromodulation spectroscopy on inorganic materials has already been shown [12, 13]. However, the techniques' transfer to be applicable to organic thin-films is not straightforward, due to the much smaller mobilities which require a higher sensitivity and thus a higher stability of the system. In the following work, the basic principle of the experimental technique, the analysis of the data and first results on molecular semiconductors are presented. Furthermore, the sample requirements and the techniques' detection limits are discussed.

P. Riederer and R. Kersting: Terahertz Electromodulation Spectroscopy for Characterizing Electronic Transport in Organic Semiconductor Thin Films. *J. Infrared Millim. Terahertz Waves* **44**, 1-16 (2023); doi: 10.1007/s10762-022-00893-z; licensed under a Creative Commons Attribution (CC BY) license.

Author contribution: P.R. fabricated the samples and measured the data. R.K. supervised the study. P.R. and R.K. drafted the manuscript. All authors contributed with writing the final version of the manuscript.

Reprinted under the terms of the Creative Commons Attribution License (CC BY 4.0, <http://creativecommons.org/licenses/by/4.0/>), which permits unrestricted use and redistribution provided that the original author and source are credited.

Journal of Infrared, Millimeter, and Terahertz Waves (2023) 44:1–16  
<https://doi.org/10.1007/s10762-022-00893-z>



## Terahertz Electromodulation Spectroscopy for Characterizing Electronic Transport in Organic Semiconductor Thin Films

Philipp Riederer<sup>1</sup> · Roland Kersting<sup>1</sup>

Received: 10 October 2022 / Accepted: 29 November 2022 / Published online: 26 December 2022  
© The Author(s) 2022

### Abstract

Terahertz (THz) spectroscopy is a well-established tool for measuring the high-frequency conductance of inorganic semiconductors. Its application to organic semiconductors, however, is challenging, because of the low carrier mobilities in organic materials, which rarely exceed  $10 \text{ cm}^2/\text{Vs}$ . Furthermore, low charge carrier densities in organic field-effect devices lead to sheet conductivities that are often far-below the detection limits of conventional THz techniques. In this contribution, we present the application of THz electromodulation spectroscopy for characterizing charge transport in organic semiconductors. Pulses of THz radiation are transmitted through organic field-effect devices and are time-resolved by electro-optic sampling. A differential transmission signal is obtained by modulating the gate voltage of the devices. This controls charge injection into the semiconductors, where the charge carriers reduce the THz transmission by their Drude response. Advantageous is that a nearly noise-free differential transmission can be obtained. Furthermore, electro-modulation allows to sense specifically either injected electrons or holes. Because the method exclusively probes transport of mobile carriers, it provides access to fundamental transport properties, which are difficult to access with conventional characterization methods, such as conductance measurements of organic field-effect transistors. The outstanding property that a relative differential signal is measured allows to obtain charge carrier mobilities with high reliability. Mobilities as small as  $1 \text{ cm}^2/\text{Vs}$  can be probed, which makes THz electromodulation spectroscopy an attractive tool for studying charge transport in most technologically relevant organic semiconductors.

**Keywords** Terahertz spectroscopy · Conductivity · Mobility · Thin films · Organic semiconductors

---

✉ Roland Kersting  
[roland.kersting@lmu.de](mailto:roland.kersting@lmu.de)

<sup>1</sup> Photonics and Optoelectronics Group, Faculty of Physics and Center for NanoScience (CeNS), Ludwig-Maximilians-Universität, Königstr. 10, 80539 Munich, Germany

PACS 07.60.-j · 73.50.-h · 81.70.Fy · 81.05.Fb

## 1 Introduction and Objective

Many physical properties of semiconductors determine their applicability in future devices, and the corresponding characterization techniques range from conductance measurements to failure analysis [1]. The prime research interest of organic semiconductors focuses on their electrical conductivity. Organic field-effect transistors (FETs) promise application in a variety of fields, ranging from display technology to electrochemical sensing and bioelectronics [2–5]; thus, most works on organic semiconductors investigate charge transport in FETs [6].

Concluding from the devices' conduction onto the physics of charge transport, however, is challenging, particularly when investigating thin films of organic semiconductors, which are polycrystalline by nature. As illustrated in Fig. 1a, contact resistances due to injection and extraction barriers, grain boundaries, and traps slow down charge transport between the source and drain contacts of FETs. Thus, several physical phenomena affect the devices' overall conductance, and the extraction of intrinsic transport properties is difficult and not always unambiguous. The same is expected when using van der Pauw techniques [7, 8], Hall measurements [9, 10], and time-of-flight methods [11, 12], because here, carrier transport is also hindered by grain boundaries and traps. Furthermore, several works have warned that the extraction of the carriers' mobility  $\mu$  from conductance data have led to severe overestimates in the past [13, 14].

Terahertz (THz) spectroscopy offers an alternative access to intrinsic transport properties of semiconductors [15]. As illustrated in Fig. 1b, charge carriers, as for instance holes, respond to the field  $E(t)$  of the incident THz pulse and change the transmission of the THz radiation. By analyzing transmission data in amplitude and phase, the conductivity  $\sigma$  and the Drude mobility  $\mu$  of the charge carriers

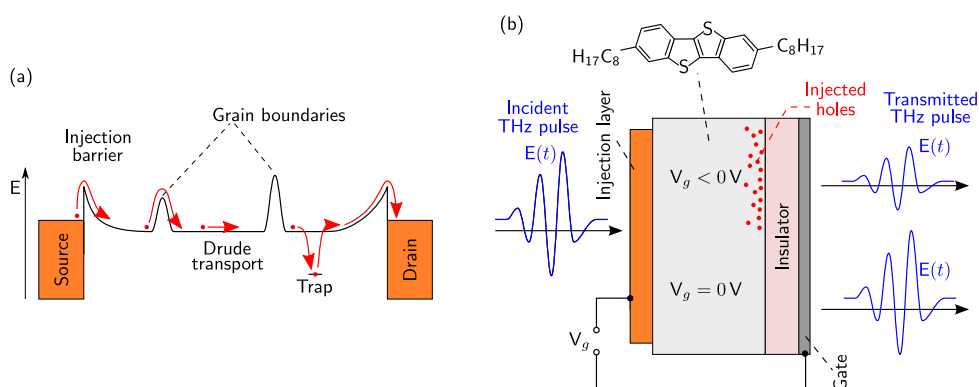


**Fig. 1** **a** Illustration of classical conductance measurements. Schottky barriers, grain boundaries, and traps hinder charge transport along the channel between source and drain. **b** Schematic of THz electromodulation spectroscopy where injected charge carriers reduce the transmission of THz radiation

can be deduced. The concept's applicability and precision has been demonstrated in pioneering works on bulk semiconductors, such as silicon and GaAs [16, 17]. However, most technically relevant organic semiconductors are intrinsic and contain no mobile carriers [18]. One technical solution is the photo-generation of electron–hole pairs prior to probing the conductance with THz radiation [19–22]. The separation of the individual conductivities of electrons and holes, however, is difficult, because both affect THz transmission.

In this work, we show that THz electromodulation spectroscopy is a suitable tool for investigating charge transport in molecular semiconductors. As illustrated in Fig. 1, the polarity of the gate voltage causes the injection of either electrons or holes. Thus, only one type of carriers is probed, and switching between two gate voltages  $V_g$  provides a differential THz signal, from which the sheet conductivity  $\sigma_{2D}$  and the Drude mobility  $\mu$  can be deduced. Similar techniques have been developed for the microwave region [23, 24].

## 2 Experimental Technique

### 2.1 Setup for THz Electromodulation Spectroscopy

In a semiconductor thin film, the conductivity of the charge carriers causes absorption and dispersion of THz radiation when transmitted through the structure. Insight into the physics of charge transport can be obtained from the frequency dependence of the transmission, and it is common practice to resolve the THz signals in time-domain followed by Fourier transformation of the data [25, 26]. The required sub-picosecond time resolutions can be achieved, for instance, by Auston switches [27], photoconductive antennas [28, 29], homodyne mixing [30, 31], heterodyne mixing [32, 33], and electro-optic sampling [34, 35].

The setup presented here utilizes electro-optic sampling and is illustrated in Fig. 2. The laser source is a Ti:Sapphire oscillator, which produces pulses of 80-fs duration centered at 780 nm at a repetition rate of 80 MHz. A beam splitter divides the laser power into a 500-mW beam for exciting the THz emitter and a sampling beam of 100 mW, which is used for time-resolving the THz signal. The THz emitter is an interdigitated metal-semiconductor-metal structure fabricated on top of semi-insulating GaAs as described in Ref. [36]. For collimating and for focusing the THz radiation, off-axis parabolic mirrors with working distances of 100 mm and 150 mm are used. The sample is positioned at one focus of the THz beam path. For low-temperature measurements, a cryostat can be inserted through a 100-mm flange. The radiation transmitted through the sample is focused onto a 1-mm-thick (110) ZnTe crystal. The probe beam passes a polarizer and a half-wave plate ( $\lambda/2$ ). After reflection on a semi-insulating silicon wafer, the probe beam is brought to overlap with the THz pulses within the ZnTe crystal for electro-optic sampling of the THz field. A Wollaston prism splits up the two polarization components, each of which is detected by a photodiode. This copies the THz pulses' amplitude and phase information onto the 780-nm beam. A quarter-wave plate ( $\lambda/4$ ) is used for balancing the DC current of the photodiodes.

The photodiodes' differential photocurrents are amplified and measured using a digital lock-in amplifier (LIA). As will be shown in Section 3, the signal changes due to the charge carriers are minute and their detection requires efficient noise suppression, which can be achieved by modulating the THz beam at high frequency. In our setup, modulation frequencies of approximately 40 kHz are used for switching the electrical polarity of the THz emitter and thus the polarity of the emitted THz pulses. For this, the LIA's reference output sources a power amplifier, which drives the THz emitter (Em) with an amplitude of 8 V. The AC signal of the photodiodes is amplified by the LIA and averaged by a low-pass filter with a time constant of 30  $\mu$ s. The output voltage is digitized at 102 kHz with 24-bit resolution prior to processing by the measurement software.

The absorption of THz radiation by water is eliminated by mounting the optical setup in a vacuum chamber, which reaches pressures of 0.1 mbar. Figure 3 shows typical THz transients obtained without a sample. The data are recorded in dependence on time delay  $t$  between THz pulse and sampling laser pulse (illustrated in Fig. 2). The corresponding spectrum spans from approximately 0.3 to 2.6 THz. Because of the setup's insulation by the vacuum chamber and the referencing at 40 kHz, the signal-to-noise ratio of the setup reaches  $\eta = 2 \times 10^5 \text{ Hz}^{1/2}$ .

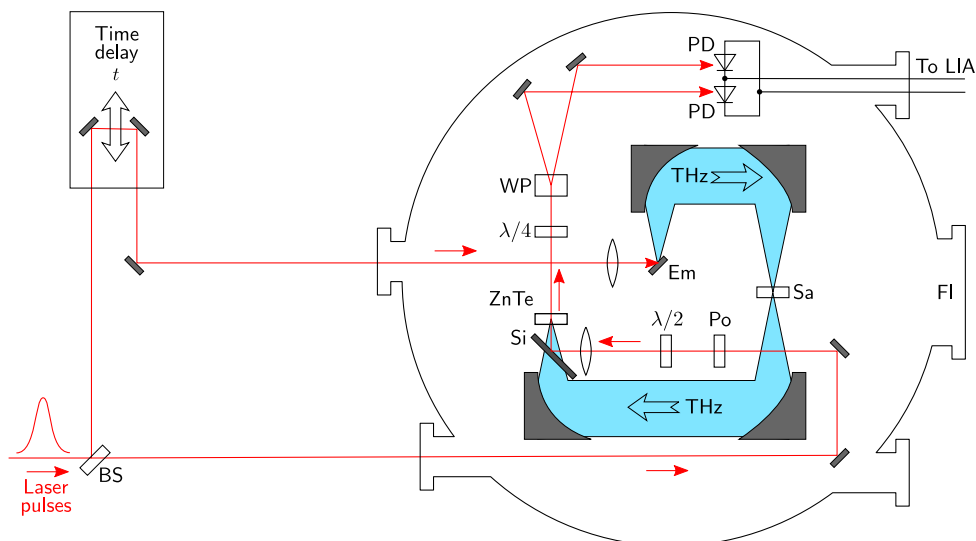


**Fig. 2** Schematic of the setup. The vacuum chamber has a diameter of 0.8 m. Abbreviations used: Terahertz emitter (Em), sample (Sa), flange for inserting an optional sample cryostat (FI), beam splitter (BS), polarizer (Po), half-wave plate ( $\lambda/2$ ), quarter-wave plate ( $\lambda/4$ ), silicon beam splitter (Si), zinc telluride crystal (ZnTe), Wollaston prism (WP), photo diode (PD), lock-in amplifier (LIA)

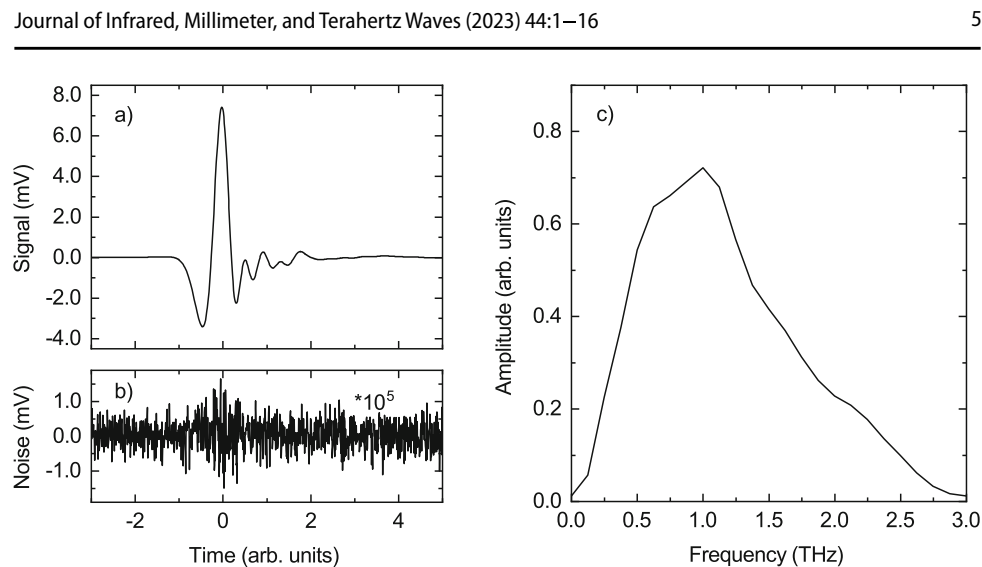


**Fig. 3** **a** Time-resolved THz pulse acquired at a total integration time of 20 s per data point. **b** Noise of the system. **c** Corresponding amplitude spectrum

## 2.2 Thin-Film Devices

The classical approach for deducing the charge carriers' conductivity  $\sigma$  is to compare two THz transients: one recorded after transmission through the semiconductor and a second one, a reference, without the sample [16, 17]. This concept cannot be applied when characterizing organic thin films. Compared to silicon, where electron mobilities can reach  $\mu \approx 1500 \text{ cm}^2/\text{Vs}$ , the mobilities in organic semiconductors rarely exceed  $10 \text{ cm}^2/\text{Vs}$ . Furthermore, organic field-effect structures have accumulation layers that are only a few nanometers thick [18, 37]. Both lead to diminutive sheet conductivities  $\sigma_{2D} = e\mu n_{2D}$  and thus to a weak interaction between the THz radiation and the carriers within the organic semiconductor. Changes in the setup's performance between two consecutive measurements would cause transmission changes that exceed by far the imprint of the charge carriers onto the THz transmission.

Electromodulation overcomes this challenge. Within milliseconds, charge carriers can be electrically injected into the device or can be extracted. This allows for recording the two required transmission signals without mechanically replacing the sample. The technique, however, requires electrically controllable semiconductor thin films. A suitable device structure is illustrated in Fig. 4a. The geometrical dimensions of the devices are set by the focal width of the THz beam. An active area with a diameter of 5 mm is appropriate for the setup discussed above.

All devices presented here are fabricated on 1-mm-thick sapphire substrates or on  $125 \mu\text{m}$ -thick foils of polyethylene naphthalate (PEN). Devices on PEN foil are flexible, as shown in Fig. 4b and allow the fabrication of large sets of individual structures on a single foil. The advantage of sapphire substrates is their good heat conductance, which is required for low-temperature experiments.

The first layer deposited on top of the substrate is a 6-nm-thick chromium film, which will later serve as gate contact. This thin chromium layer sufficiently transmits

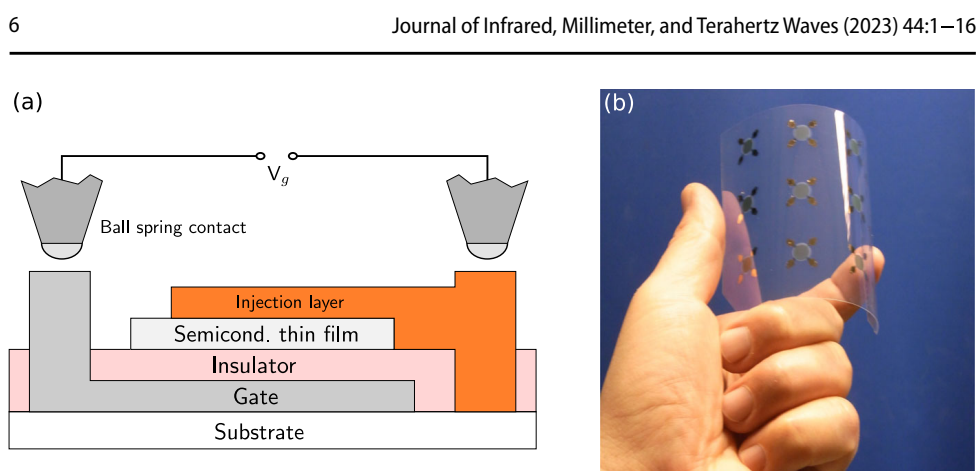


**Fig. 4** **a** Schematic of a cross section through a device for THz electromodulation spectroscopy. **b** Image of bendable devices fabricated on PEN foil

THz radiation. The insulator is a parylene N film with a thickness of approximately 300 nm. At this thickness, break-through fields of about 2.5 MV/cm can be reached, which sets the upper limit of the injected charge density to nearly  $4 \times 10^{12} \text{ cm}^{-2}$ .

The organic semiconductor is deposited on top of the parylene and has a thickness of about 50 nm. This work presents data obtained on the molecular semiconductors dinaphtho[2,3-b:2',3'-f]thieno[3,2-b]thiophene (DNTT) [38], 2,7-dioctyl[1]benzothieno[3,2-b][1]benzothiophene ( $\text{C}_8$ -BTBT- $\text{C}_8$ ), and 2,7-didodecyl[1]benzothieno[3,2-b][1]benzothiophene ( $\text{C}_{12}$ -BTBT- $\text{C}_{12}$ ) [39]. As injection layers, various materials can be used, such as 2 nm Au topped by 6 nm Cr or 3 nm  $\text{MoO}_x$  followed by 6 nm Cr. The purpose of the chromium to provide conductivity across the device, whereas the purpose of the gold and  $\text{MoO}_x$  is to establish electrical contact to the underlying molecular semiconductor. A precise control of the contact metal thicknesses is crucial as layers thinner than 5 nm often show no percolation whereas thick layers reduce the transmitted signal significantly. Additionally, the thickness of the injection metal depends on the roughness of the semiconductor. On rough semiconductors, metal films with thicknesses up to 15 nm may be needed in order to achieve full percolation.

Good electrical contacts require metallic layers with work functions that fit the band edges of the organic semiconductor. The work functions of Au (4.7 eV) and  $\text{MoO}_x$  ( $\approx 5.6$  eV) are close to the valence bands of many molecular semiconductors, which reduces the height of the injection barriers and allows for efficient injection of holes [40, 41].

The metallic layers and the molecular semiconductors are fabricated by physical vapor deposition at a base pressure of  $10^{-7}$  mbar. Typical deposition rates are  $0.2 \text{ \AA/s}$ . The parylene N layers are fabricated by chemical vapor deposition [42] at a pressure of  $10^{-2}$  mbar with a deposition rate of  $1 \text{ \AA/s}$ . Prior to every deposition step, the devices are heated up to  $60^\circ\text{C}$  at  $10^{-7}$  mbar for several hours, which removes residual water and other contaminants from the surfaces and increases the purity of the deposited semiconductors. After fabrication, the devices may be sealed with 300 nm of parylene N (not shown in Fig. 4), which prevents indiffusion of contaminants and increases the device lifetime.

Electrical contact to the devices is achieved by ball spring contacts. The two metal layers that sandwich the semiconductor form a capacitor with a capacitance of  $C \approx 2$  nF. Each of the two metal layers has two leads, by which the load resistance of the capacitor can be deduced, which is typically  $R \approx 1$  k $\Omega$ . The resulting time constant  $\tau_{RC} = RC \approx 2$   $\mu$ s, sets the upper limit of the modulation frequency of the devices. The experiments shown here are performed at modulation frequencies below 100 Hz.

### 3 Results on Molecular Thin Films

In molecular semiconductors, conduction due to electrons, as well as due to holes, has been observed [18]. In general, the mobilities in p-conducting materials exceed by far those observed in n-conducting molecular semiconductors [43]. In this work, we focus exclusively on p-conducting molecular semiconductors.

With the injection of charge carriers, the THz transmission  $\Delta S$  through the devices decreases, as shown in Fig. 5. All investigated devices show relative transmission changes  $|\Delta S/S| \leq 2 \times 10^{-4}$ . These small signals attest the need for excellent noise properties of the setup. Ramping the gate voltage  $V_g$  causes the injection of charge carriers into the semiconductor and thus a reduction of the THz transmission, as shown in Fig. 5. However, the THz signal is reduced only while  $V_g$  is negative, that is, during periods when holes are accumulated within the semiconductor. At positive  $V_g$ , no reduction of the THz transmission is observed, as it would be expected for electrons. Apparently, the conductance due to the injection of electrons is marginal, which may either be because of too high injection barriers or negligible conductance of the injected electrons.

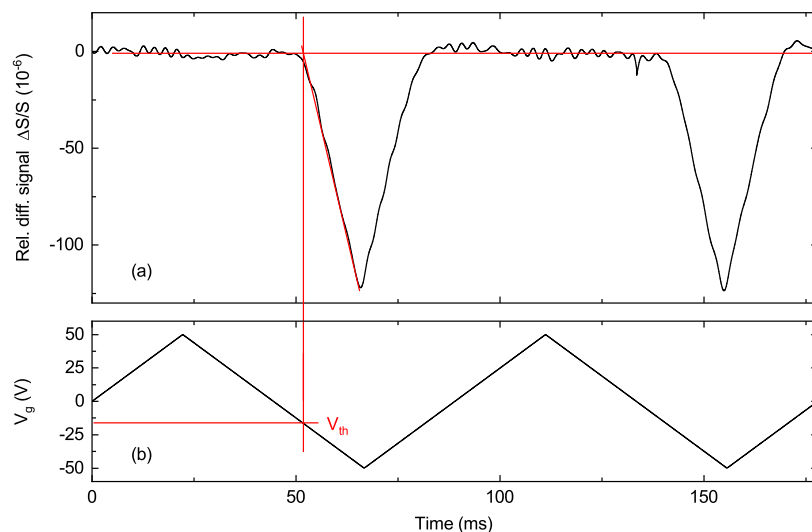


**Fig. 5** Electromodulation of a  $C_8$ -BTBT- $C_8$  device on the millisecond time scale. **a** Change of the transmission signal  $\Delta S/S$  recorded at the peak of the THz pulse. **b** Applied gate voltage. The red lines illustrate the procedure for deducing the threshold voltage  $V_{th}$

The THz signal in Fig. 5a linearly follows the applied gate voltage as shown in Fig. 5b. Thus, the time delay between application of  $V_g$  and the actual charging or discharging of the device occurs on time scales that are much shorter than the modulation period of about 100 ms (Fig. 5). An exponential dependence as it would be expected for significant injection barriers is not observed.

The analysis of the THz signals described in Section 4 requires knowledge of the injected sheet density of charge carriers  $n_{2D,inj}$ . Two methods can be applied: (i) Measurements of the device's capacitance per unit area  $\tilde{C}$  provide a good estimate of the injected charge in dependence of applied gate voltage  $V_g$ . Nevertheless, this procedure requires that injection barriers can be neglected and that the charge carrier density follows in a linear manner  $V_g$  as indicated in Fig. 5. (ii) Alternatively, the injected density  $n_{2D,inj}$  can be deduced by integrating the time-dependent charging current. In all experiments reported here, we find no significant difference between the values determined with the two methods. However, both methods provide only the density of charges injected into the device  $n_{2D,inj}$ , which is not necessarily identical with the density of mobile charges  $n_{2D}$  within the accumulation region at the interface to the insulator.

Figure 5 also shows an offset between  $V_g$  and the decay of the THz transmission, the threshold voltage  $V_{th}$ . In most devices,  $V_{th}$  is negative, and holes are injected only if  $V_g < V_{th}$ . The linearity of the signal in Fig. 5 suggests that a polarization density  $P$  is present within the device and that the sheet density of mobile charge carriers is described by

$$e n_{2D} = \tilde{C} V_g - P \quad (1)$$

where  $\tilde{C}$  is the unit capacitance per area. Evaluating the threshold voltage, as indicated in Fig. 5, therefore allows for determining the carrier sheet density  $n_{2D}$ . The difference between  $n_{2D,inj}$  and  $n_{2D}$  results from the built-in polarization of the device. For the following measurements, typical sheet densities of  $n_{2D} \approx 10^{12} \text{ cm}^{-2}$  are deduced.

The charge carriers within the device respond in an oscillatory motion to the driving THz pulse, as shown in Fig. 6a by  $\Delta S(t)$ . The transients are recorded by applying a square-wave voltage with an amplitude of 50 V at a frequency of about 11 Hz. For each modulation state, two signals are recorded: one without charge carriers within the semiconductor and one with carriers,  $S_0(t)$  and  $S_1(t)$ , respectively. The difference  $\Delta S(t) = S_1(t) - S_0(t)$  is about four orders of magnitude smaller than the original transmission signals. Between the two modulation states, only the hole density within the device changes. Thus,  $\Delta S(t)$  exclusively results from the response of the charge carriers to the THz pulse. A closer inspection proves causality of the charge carrier's response. The magnifications of the center peaks in Fig. 6c and d show that the charge carriers delay the transmission of the THz pulses.

#### 4 Analysis of Electromodulation Data

The purpose of THz electromodulation spectroscopy on thin film semiconductors is to determine electrical properties, such as conductivity  $\sigma$  and mobility  $\mu$ . A first

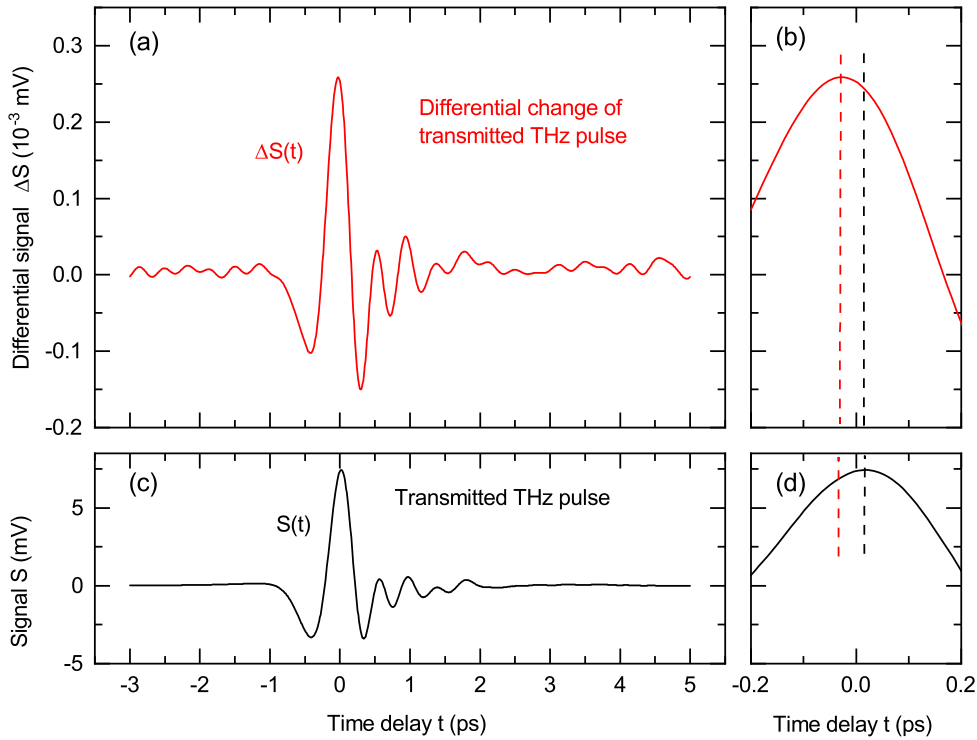


**Fig. 6** **a** Transmission change  $\Delta S$  due to electromodulation of a DNTT device at  $V_g = \pm 50$  V. **b** Magnification of the peak of  $\Delta S(t)$ . **c** Signal  $S(t)$  of the transmitted THz pulse and **d** magnification of the peak of  $S(t)$

estimate can be drawn from the extremal values of  $\Delta S$  of the data shown, for instance, in Figs. 5 and 6, using an equivalent of Tinkham’s formula [44, 45]:

$$\sigma_{2D} = \frac{-\Delta S}{S} \frac{2\sqrt{\epsilon_b}}{Z_0} \tag{2}$$

where  $\epsilon_b$  is the background permittivity of the semiconductor and  $Z_0 = 376.7 \Omega$  is the impedance of free space. Supposition of the above approximation is that the thickness of the conducting sheet is much smaller than the wavelength, which is the case in our structures [46]. Taking, for instance,  $-\Delta S/S = 10^{-4}$  from Fig. 5 and assuming for  $\epsilon_b = 2.8$  [24, 47] yields  $\sigma_{2D} = 0.89 \times 10^{-6} \Omega^{-1}$  and  $\mu = 2.8 \text{ cm}^2/\text{Vs}$  when using the estimate of Eq. 2.

Such an estimate, however, neglects the frequency dependence of the charge carriers’ response. Previous work [48] has shown that the holes’ response can be well described by Drude gas with complex sheet conductivity:

$$\sigma_{2D}(\omega) = \frac{n_{2D} e^2 \tau}{m_h^*} \cdot \frac{1 + i \omega \tau}{1 + \omega^2 \tau^2} \tag{3}$$

where  $\tau$  is the Drude scattering time,  $m_h^*$  is the holes’ effective mass, and  $\omega$  is the angular frequency.

The complex conductivity causes not only absorption and dispersion of the transmitted THz radiation. Additionally, reflections may occur at every interface, because the index of refraction of the semiconductor changes with  $n_{2D}$ . A rigorous treatment would require calculation of the device’s overall transmission by matrix methods [49]. However, the quantity  $\Delta S/S$  is a relative differential signal. This allows for neglecting the optical transmission through the substrate, the gate metal, and the injection layer. For obtaining  $\Delta S/S$ , two different layer stacks have to be analyzed, as illustrated Fig. 7. Both stacks are the same, except for layer 2, which either contains no charge carriers (a) or the injected charges (b). The thicknesses are  $d_1 \approx 300$  nm,  $d_2 \approx 3$  nm, and  $d_3 \approx 50$  nm.

The propagation of THz radiation through a layer indexed by  $n$  is described by its complex wave vector  $k_n$  and  $E_n(t) = E_{n,0} \exp\{i(k_n z - \omega t)\}$  for the electric field, when assuming propagation in  $z$ -direction. In conducting media, the current density is  $j = \sigma E$  and the wave vector becomes [50]:

$$k = \sqrt{\omega^2 \epsilon_b \epsilon_0 \mu_0 + i \omega \mu_0 \sigma} \tag{4}$$

where  $\epsilon_b$  is the relative background permittivity of the material, and  $\epsilon_0$  and  $\mu_0$  are the electric and magnetic field constants, respectively.

Considering absorption within the layers and reflection at every interface leads to the complex transmission of such a three-layer system [49]:

$$t = \frac{4 k_1 k_2 e^{i k_2 d_2}}{(k_1 + k_2)(k_2 + k_3) + (k_1 - k_2)(k_2 - k_3) e^{2 i k_2 d_2}} \tag{5}$$

Again, absorption and dispersion within layers 1 and 3 do not need to be considered for evaluating transmission changes due to modulation of layer 2. A similar equation was derived for changes of the index of refraction by photoinjected carriers [51].

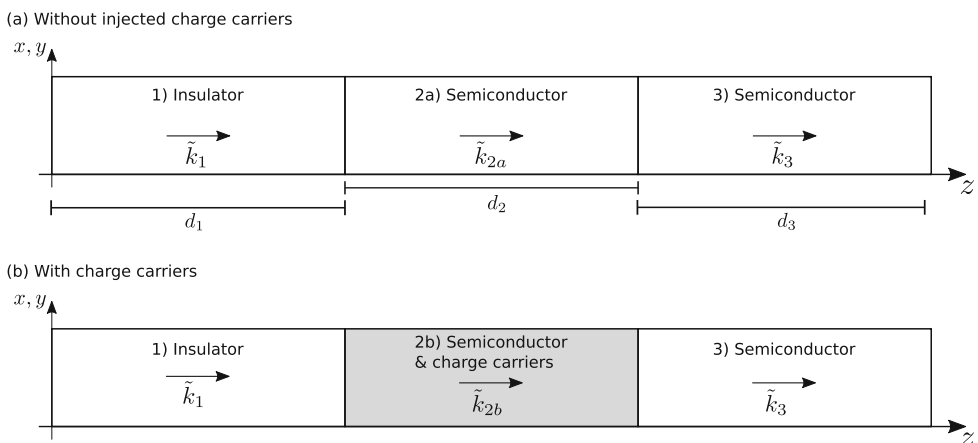


**Fig. 7** Layer sequence for analyzing the relative differential transmission  $\Delta S/S$ . The illustrations visualize the two modulation states: **a** without injected carriers and **b** state with injected carriers. The thicknesses of the layers are  $d_i$  and the complex wave vectors of the THz radiation are labelled by  $k_i$

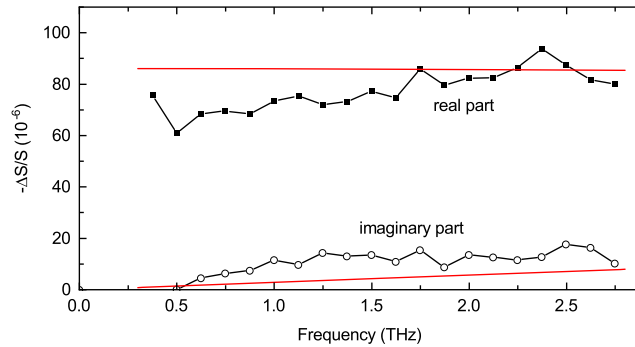


**Fig. 8** Relative differential transmission obtained on C<sub>12</sub>-BTBT-C<sub>12</sub> in dependence of frequency. The experimental data for the real and imaginary part of the differential transmission are shown by black squares and circles, respectively. Calculations based on the Drude model are shown by red lines. Reprint with permission from Ref [48]. Copyright 2017 American Chemical Society

Using Eq. 5, the calculated relative differential transmission follows from:

$$\frac{\Delta S}{S} = \frac{t_{2b} - t_{2a}}{t_{2a}} \quad (6)$$

where  $t_{2a}$  and  $t_{2b}$  are the transmissions calculated for the modulation states without carriers and with carriers, respectively.

Experimental data obtained on C<sub>12</sub>-BTBT-C<sub>12</sub> and calculated data are compared in Fig. 8 in frequency domain. Measurements, such as those displayed in Fig. 6, provide  $\Delta S(t)$  and  $S(t)$ , which are Fourier-transformed to  $\Delta S(\nu)/S(\nu)$ . The symbols in Fig. 8 show the real part and the imaginary part. Also shown are calculations following Eqs. 3 to 6. Used parameters are  $n_{2D} = 0.92 \times 10^{12} \text{ cm}^{-2}$ , which is deduced from the devices unit capacitance using gate voltage  $V_g = -50 \text{ V}$  and threshold  $V_{th} = -12 \text{ V}$ . For the effective hole mass  $m_h^*$ , the free electron mass is assumed. This leaves the Drude scattering time  $\tau$  as a fit parameter. Reasonable agreement between experimental data and calculation is achieved for  $\tau = 5.3 \text{ fs}$ . The corresponding Drude mobility is  $\mu = e\tau/m_h^* = 9.3 \text{ cm}^2/\text{Vs}$ . In a similar way, mobilities of  $21 \text{ cm}^2/\text{Vs}$  have been deduced for pentacene [52]. For DNNT,  $\mu = 1.5 \text{ cm}^2/\text{Vs}$  is deduced by considering the frequency dependence given in Eq. 3, which exceeds the value of  $0.84 \text{ cm}^2/\text{Vs}$  obtained with the estimate according to Eq. 2. The origin of the difference shows that considering the frequency dependence goes beyond the estimate of  $\Delta S/S$  from the peak amplitude only.

The obtained mobilities are local mobilities and mirror the intrinsic transport properties of the semiconductors investigated. For the holes in the accumulation region, a mean free path  $L = \sqrt{2k_B T \tau^2/m_h^*} \approx 0.5 \text{ nm}$  is estimated using the fit parameters of  $m_h^* = m_e$  and  $\tau = 5.3 \text{ fs}$ . This distance is much smaller than the grain sizes, which are about  $250 \text{ nm}$ . Thus, the majority of the holes is not hindered by grain boundaries when following the THz field in an oscillatory motion. Similar holds for traps, for which a minimum spacing of  $d_{\text{trap}} \geq 10 \text{ nm}$  can be deduced from  $n_{2D}$ , because apparently, not all holes are trapped. Altogether, THz electromodulation spectroscopy probes the intrinsic mobility of charge carriers on local nanoscopic scale.

## 5 Limitations of the Technique and Future Applications

One factor that limits the application of the technique is the noise of the setup. The relative noise of every data point can be estimated from the signal-to-noise ratio of the technique  $\eta$ , the number of data points of one scan  $N_{\text{sampl}}$ , and the scan's integration time  $T_{\text{tot}}$ :

$$\frac{\Delta y}{y} = \frac{1}{\eta} \sqrt{\frac{T_{\text{tot}}}{2 N_{\text{sampl}}}} = 6.7 \times 10^{-6} \quad (7)$$

when assuming  $\eta = 2 \times 10^5 \text{ Hz}^{1/2}$ ,  $N_{\text{sampl}} \approx 1000$ , and  $T_{\text{tot}} = 1 \text{ h}$ . This value equals the smallest detectable signal  $(\Delta S/S)_{\text{min}}$  and using Eq. 2 provides an estimate for the minimum mobility that can be detected when evaluating a single data point

$$\mu_{\text{min}} = \left( \frac{\Delta S}{S} \right)_{\text{min}} \frac{2\sqrt{\epsilon_b}}{Z_0 e n_{2D}} \approx 0.40 \text{ cm}^2/\text{Vs} \quad (8)$$

for  $\epsilon_b = 2.8$  and  $n_{2D} = 0.92 \times 10^{12} \text{ cm}^{-2}$ . Measurements on several organic semiconductors have shown that the practical limit for the lowest detectable mobility is  $\mu_{\text{min}} \approx 1 \text{ cm}^2/\text{Vs}$ . This agrees well with the mobility of  $\mu = 1.5 \text{ cm}^2/\text{Vs}$ , which was evaluated for DNTT.

Are the mobilities deduced from THz electromodulation experiments reliable? Carrier mobilities obtained by conventional conductance measurements result from absolute measurements of quantities, as for instance of the current that flows through the FET's channel. In contrast, THz mobilities are deduced from the relative differential transmission  $\Delta S/S$ , which makes them very reliable. The only uncertainty is the injected charge density, which can be deduced with high precision from the capacitance of the device and from the thresholds of the gate voltages shown in Fig. 5.

Long-time fluctuations of the laser system appear to be a limiting factor. Furthermore, at such small mobilities, the diffusive mean free path of the charge carriers may be smaller than the unit cell of the semiconductor lattice and the Ioffe-Regel criterion prohibits the application of Drude theory [53]. Altogether the minimum detectable mobility of  $\mu \approx 1 \text{ cm}^2/\text{Vs}$  shows that the technique can be applied to many molecular and polymeric semiconductors.

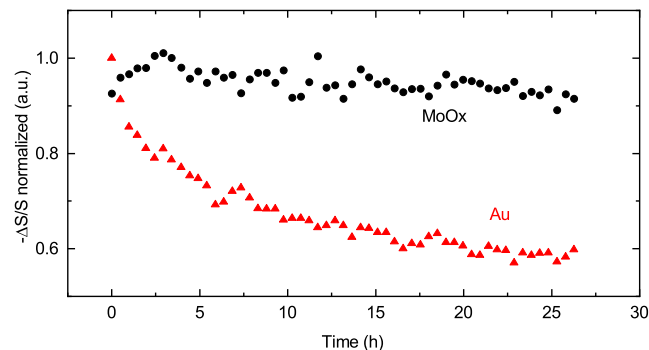


**Fig. 9** Decay of the relative differential transmission signal  $-\Delta S/S$  with time of a C8-BTBT-C8 device. The red triangles and black circles show data recorded on structures with a Au/Cr injection layer and with a MoO<sub>x</sub>/Cr injection layer, respectively

Integration times of several hours, however, require sufficient stability of the investigated devices. The devices' longevity is strongly limited by extrinsic factors. Works on field-effect transistors have shown that indiffusion of water [54, 55] and oxygen [56, 57] reduces device performance, presumably because of trap formation. Two measures help avoiding such impurities: (i) During device fabrication, contaminating the layer surfaces should be avoided. (ii) After device fabrication, the structures should be coated with a protective layer, such as parylene N, which hinders indiffusion of contaminants from the environment.

Another limiting factor is ion migration within the multilayer structure, as this process can rapidly deteriorate the device. We found that gold ions are transported by the electric field from the injection contact toward the channel region [58]. According to Eq. 1, the resulting polarization reduces the number of mobile charges. In structures that contain Au injection layers,  $-\Delta S/S$  decreases within few hours, as shown in Fig. 9 because of the reduction of the density of free holes. Much more stable is the usage of  $\text{MoO}_x/\text{Cr}$  injection layers. Such devices have strongly increased lifetimes, as shown in Fig. 9. These results demonstrate that THz electromodulation spectroscopy is also suited for characterizing extrinsic processes that limit the performance of future organic FETs.

The application of THz electromodulation spectroscopy is not limited to the characterization of molecular semiconductors. Attractive is, for instance, its application to polycrystalline and nanocrystalline inorganic semiconductors. In such materials, grain boundaries, traps, and local screening also impact on macroscopic charge transport [59, 60], which makes it difficult to conclude from classical conductance measurements on intrinsic transport properties. Of particular interest may be the application to polymeric semiconductors and blends of polymeric and molecular semiconductors, because of their enormous potential in organic electronics and photovoltaics [61, 62]. Although most amorphous polymers reveal mobilities far below  $1 \text{ cm}^2/\text{Vs}$ , many works have shown that several semiconducting polymers form composites of a crystalline phase embedded within an disordered phase [63–65]. Here, THz electromodulation spectroscopy may provide insights into the charge transport within those nano-crystallites, which are expected to have much larger mobilities than the surrounding amorphous phase.

## 6 Conclusion

Terahertz electromodulation spectroscopy provides access to the local properties of electrical transport in thin-film devices of organic semiconductors. The technique can be applied for probing the conductivity of charge carriers having mobilities exceeding  $1 \text{ cm}^2/\text{Vs}$ . One advantage of the technique is that a relative differential signal is measured, which allows for the deduction of conductivities independent of external factors, such as contact resistances or device geometries. Data evaluation in the frequency domain shows that the charge carriers in molecular semiconductors can be described by a Drude gas with mobilities of about  $10 \text{ cm}^2/\text{Vs}$ . Besides the determination of charge transport properties, the technique is suited for accessing the impact of

external factors onto device performance, such as degradation due to ion migration from the devices' contacts into the organic semiconductor.

**Acknowledgements** The authors thank Y. Geerts from Université Libre de Bruxelles for supplying the C<sub>12</sub>-BTBT-C<sub>12</sub> as well as Philipp Altpeter and Christian Obermayer for the technical support.

**Author Contribution** P. R. and R. K. wrote the manuscript. P. R. measured the data of Figs. 3, 5, 6, and 9. All authors reviewed the manuscript.

**Funding** Open Access funding enabled and organized by Projekt DEAL. This research was funded by the Deutsche Forschungsgemeinschaft (DFG, German Research Foundation), contract KE 516/11-1.

**Data Availability** The data that support the findings of this study are available from the corresponding author upon reasonable request.

## Declarations

**Competing Interests** The authors declare no competing interests.

**Open Access** This article is licensed under a Creative Commons Attribution 4.0 International License, which permits use, sharing, adaptation, distribution and reproduction in any medium or format, as long as you give appropriate credit to the original author(s) and the source, provide a link to the Creative Commons licence, and indicate if changes were made. The images or other third party material in this article are included in the article's Creative Commons licence, unless indicated otherwise in a credit line to the material. If material is not included in the article's Creative Commons licence and your intended use is not permitted by statutory regulation or exceeds the permitted use, you will need to obtain permission directly from the copyright holder. To view a copy of this licence, visit <http://creativecommons.org/licenses/by/4.0/>.

## References

1. D.K. Schroder, *Semiconductor Material and Device Characterization* (Wiley - IEEE Press, 2006).
2. X. Guo, Y. Xu, S. Ogier, T.N. Ng, M. Caironi, A. Perinot, L. Li, J. Zhao, W. Tang, R.A. Sporea, A. Nejim, J. Carrabina, P. Cain, F. Yan, *IEEE Trans. Electr. Dev.* **64**, 1906 (2017). <https://doi.org/10.1109/ted.2017.2677086>.
3. T. Someya, Z. Bao, G.G. Malliaras, *Nature* **540**, 379 (2016). <https://doi.org/10.1038/nature21004>.
4. J. Rivnay, S. Inal, A. Salleo, R.M. Owens, M. Berggren, G.G. Malliaras, *Nat. Rev. Mater.* **3**, 17086 (2018). <https://doi.org/10.1038/natrevmats.2017.86>.
5. K. Liu, B. Ouyang, X. Guo, Y. Guo, Y. Liu, *npj Flex. Electron.* **6**, 1 (2022).
6. G. Schweicher, G. Garbay, R. Jouclas, F. Vibert, F. Devaux, Y.H. Geerts, *Adv. Mater.* **32**, 1905909 (2020).
7. C. Rolin, E. Kang, J.H. Lee, G. Borghs, P. Heremans, J. Genoe, *Nat. Commun.* **8**, 14975 (2017).
8. S. Jiang, J. Qian, Q. Wang, Y. Duan, J. Guo, B. Zhang, H. Sun, X. Wang, C. Liu, Y. Shi, Y. Li, *Adv. Electr. Mater.* **6**, 2000136 (2020).
9. V. Podzorov, E. Menard, J.A. Rogers, M.E. Gershenson, *Phys. Rev. Lett.* **95**, 226601 (2005).
10. J.F. Chang, T. Sakanoue, Y. Olivier, T. Uemura, M.B. Dufourg-Madec, S.G. Yeates, J. Cornil, J. Takeya, A. Troisi, H. Sirringhaus, *Phys. Rev. Lett.* **107**, 066601 (2011).
11. W. Warta, N. Karl, *Phys. Rev. B* **32**, 1172 (1985).
12. N. Karl, K.H. Kraft, J. Marktanner, M. Münch, F. Schatz, R. Stehle, H.M. Uhde, *J. Vac. Sci. Techn. A* **17**, 2318 (1999).
13. E.G. Bittle, J.I. Basham, T.N. Jackson, O.D. Jurchescu, D.J. Gundlach, *Nat. Commun.* **7**, 10908 (2016).
14. H.H. Choi, K. Cho, C.D. Frisbie, H. Sirringhaus, V. Podzorov, *Nat. Mat.* **17**, 2 (2018). <https://doi.org/10.1038/nmat5035>.
15. P.U. Jepsen, D.G. Cooke, M. Koch, *Laser Photonics Rev.* **5**, 124 (2011).
16. M. van Exter, D. Grischkowsky, *Appl. Phys. Lett.* **56**, 1694 (1990).

17. N. Katzenellenbogen, D. Grischkowsky, Appl. Phys. Lett. **61**, 840 (1992).
18. G. Horowitz, in *Organic Electronics*, ed. by H. Klauk (WILEY-VCH, 2006).
19. L. Fekete, P. Kuzel, H. Nemeč, F. Kadlec, A. Dejneka, J. Stuchlik, A. Fejfar, Phys. Rev. B **79**, 115306 (2009).
20. J.B. Baxter, C.A. Schmuttenmaer, J. Phys. Chem. B **110**, 25229 (2006).
21. E. Hendry, M. Koeberg, J.M. Schins, H.K. Nienhuys, V. Sundström, L.D.A. Siebbeles, M. Bonn, Phys. Rev. B **71**, 125201 (2005).
22. E. Hendry, F. Wang, J. Shan, T.F. Heinz, M. Bonn, Phys. Rev. B **69**, 081101(R) (2004).
23. S. Seki, A. Saeki, T. Sakurai, D. Sakamaki, Phys. Chem. Chem. Phys. **16**, 11093 (2014).
24. W. Choi, Y. Tsutsui, T. Sakurai, S. Seki, Appl. Phys. Lett. **110**, 153303 (2017).
25. D. Mittleman, *Sensing with Terahertz Radiation* (Springer, Berlin, 2002).
26. C.A. Schmuttenmaer, Chem. Rev. **104**, 1759 (2004).
27. P.R. Smith, D.H. Auston, M.C. Nuss, IEEE Journal of Quantum Electronics **24**(2), 255 (1988). <https://doi.org/10.1109/3.121>.
28. C. Fattinger, D. Grischkowsky, Appl. Phys. Lett. **54**, 490 (1989).
29. H. Harde, D. Grischkowsky, J. Opt. Soc. Am. B **8**, 1642 (1991).
30. R.H. Jacobsen, K. Birkelund, T. Holst, P.U. Jepsen, S.R. Keiding, J. Appl. Phys. **79**, 2649 (1996).
31. R. Kersting, K. Unterrainer, G. Strasser, H.F. Kauffmann, E. Gornik, Phys. Rev. Lett. **79**, 3038 (1997).
32. S.E. Ralph, D. Grischkowsky, Appl. Phys. Lett. **60**, 1070 (1992).
33. J.N. Heyman, R. Kersting, K. Unterrainer, Appl. Phys. Lett. **72**, 644 (1998).
34. Q. Wu, X.C. Zhang, Appl. Phys. Lett. **67**, 3523 (1995).
35. Q. Wu, M. Litz, X.C. Zhang, Appl. Phys. Lett. **68**, 2924 (1996).
36. A. Dreyhaupt, S. Winnerl, T. Dekorsy, M. Helm, Appl. Phys. Lett. **86**, 121114 (2005).
37. D. Säiler, A. Bornschlegel, R. Kersting, Appl. Phys. Lett. **117**, 083301 (2020).
38. T. Yamamoto, K. Takimiya, J. Am. Chem. Soc. **129**, 2224 (2007).
39. P. Xie, T. Liu, J. Sun, J. Yang, Adv. Func. Mater. **32**, 2200843 (2022).
40. D. Kumaki, T. Umeda, S. Tokito, Appl. Phys. Lett. **92**, 013301 (2008).
41. M.T. Greiner, Z.H. Lu, NPG Asia Materials **5**, e55 (2013).
42. J.B. Fortin, T.M. Lu, *Chemical Vapor Deposition Polymerization: The Growth and Properties of Poly-ylene Thin Films* (Kluwer Academic Publishers, Boston, Dordrecht, New York, London, 2004).
43. J.T.E. Quinn, J. Zhu, X. Li, J. Wang, Y. Li, J. Mater. Chemistry C **5**, 8654 (2017). <https://doi.org/10.1039/c7tc01680h>.
44. R.E. Glover, M. Tinkham, Phys. Rev. **108**, 243 (1957).
45. S. Funk, G. Acuna, M. Handloser, R. Kersting, Opt. Expr. **17**, 17450 (2009).
46. J. Neu, K.P. Regan, J.R. Swierk, C.A. Schmuttenmaer, Appl. Phys. Lett. **113**, 233901 (2018).
47. C. Grigoriadis, C. Niebel, C. Ruzie, Y.H. Geerts, G. Floudas, J. Phys. Chem. B **118**, 1443 (2014).
48. T.R. Arend, A. Wimmer, G. Schweicher, B. Chattopadhyay, Y.H. Geerts, R. Kersting, J. Phys. Chem. Lett. **8**, 5444 (2017).
49. P. Yeh, *Optical waves in layered media* (Wiley, 2005).
50. M. Dressel, G. Grüner, *Electrodynamics of Solids* (Cambridge University Press, 2002).
51. H. Altan, F. Huang, J.F. Federici, A. Lan, H. Grebel, J. Appl. Phys. **96**, 6685 (2004).
52. S.G. Engelbrecht, M. Prinz, T.R. Arend, R. Kersting, Appl. Phys. Lett. **105**, 012101 (2014).
53. N.F. Mott, E.A. Davis, *Electronic processes in non-crystalline materials* (Clarendon Press, 1979).
54. C. Goldmann, D.J. Gundlach, B. Batlogg, Appl. Phys. Lett. **88**, 063501 (2006).
55. A. Tamayo, T. Salzillo, M. Mas-Torrent, Adv. Mater. Interf. **9**, 2101679 (2022).
56. A. Benor, A. Hoppe, V. Wagner, D. Knipp, Org. Electr. **8**, 749 (2007).
57. T. Hallam, C.M. Duffy, T. Minakata, M. Ando, H. Siringhaus, Nanotechn. **20**, 025203 (2009).
58. P. Riederer, M. Bouraoui, R. Kersting, Appl. Phys. Lett. **120**, 243503 (2022).
59. S.G. Engelbrecht, L. De Angelis, M. Tönnies, R. Kersting, Appl. Phys. A **113**, 641 (2013).
60. S.G. Engelbrecht, T.R. Arend, T. Zhu, M.J. Kappers, R. Kersting, Appl. Phys. Lett. **106**, 092107 (2015).
61. C. Mueller, T.A.M. Ferenczi, M. Capoy-Quiles, J.M. Frost, D.D.C. Bradley, P. Smith, N. Stingelin-Stutzmann, J. Nelson, Adv. Mat. **20**, 3510 (2008).
62. K.J. Baeg, M. Caironi, Y.Y. Noh, Adv. Mater. **25**, 4210 (2013).
63. R. Noriega, J. Rivnay, K. Vandewal, F.P.V. Koch, N. Stingelin, P. Smith, M.F. Toney, A. Salleo, Nature Mat. **12**, 1038 (2013).

- 
64. X. Xue, G. Chandler, X. Zhang, R.J. Kline, Z. Fei, M. Heeney, P.J. Diemer, O.D. Jurchescu, B.T. O'Connor, *ACS Appl. Mater. Interfaces* **7**, 26726 (2015).
65. Y. Lei, P. Deng, M. Lin, X. Zheng, F. Zhu, B.S. Ong, *Adv. Mater.* **28**, 6687 (2016).

**Publisher's Note** Springer Nature remains neutral with regard to jurisdictional claims in published maps and institutional affiliations.

## 4.2 Effects of Insulator Surface Roughness on Charge Transport in Organic Field-Effect Devices

In field-effect devices, the majority of charge carriers is accumulated within the first monolayers at the insulator-semiconductor interface [113]. Thus, it seems obvious that this interface has a huge impact on the device's charge transport properties. Previous works demonstrated, that the type of gate dielectric material has a strong influence on the performance of the device [114, 115]. It has been shown, that the mobility increased if the insulator exhibits a smaller dielectric constant  $\epsilon$ . This observation has been attributed to the induced polarization by high  $\epsilon$  materials leading to enhanced localization of charge carriers at the insulator-semiconductor interface.

Besides the influence of the insulator material on the mobility it is assumed that charge transport in field effect devices is also strongly affected by the dielectric surface roughness [116]. Steudel et al. [117] have shown that the RMS roughness of the insulating silicon dioxide layer has a major impact on the performance of pentacene field-effect transistor. However, they observed that with increasing roughness of the  $\text{SiO}_2$  the pentacene crystallite size lowered. Thus, the decrease of the mobility could not be solely attributed on the roughness as the number of grain boundaries increased as well. [117]

Due to the fact, that the sole impact of the insulator roughness cannot be experimentally addressed, self-consistent calculations and topographical measurements are combined to give insight into fundamental conductance phenomena related to roughness properties of the

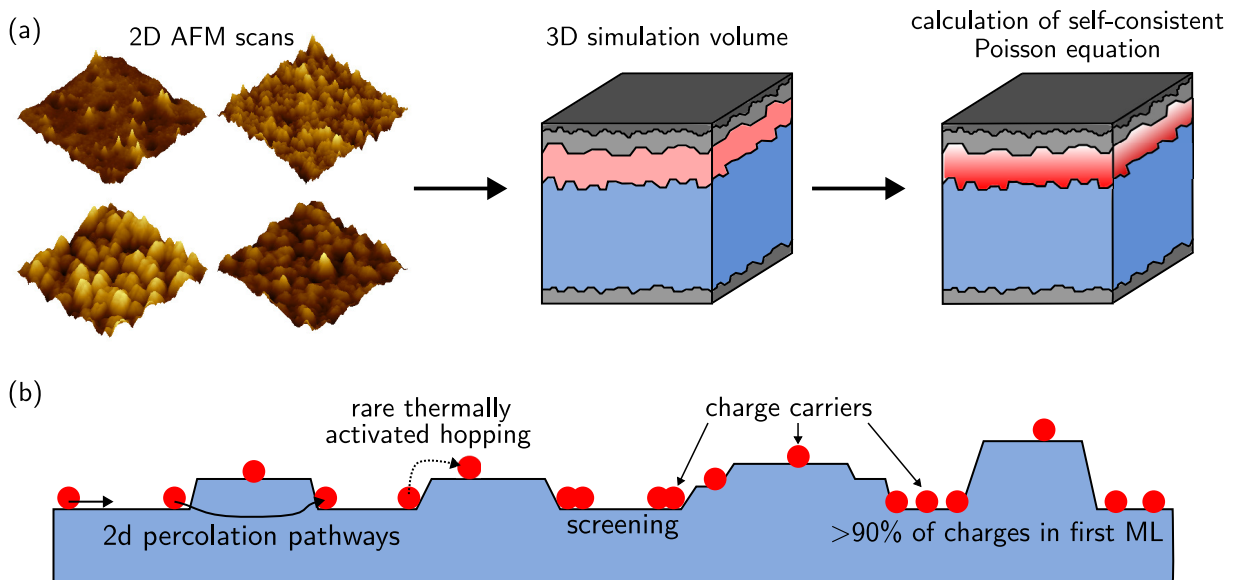


**Fig. 4.1** Work-flow of merging 2D AFM data with 3D self-consistent calculations (a). Schematic of charge transport phenomena related to insulator surface roughness (b).

insulator. Therefore, atomic force microscopy (AFM) images of the distinct surfaces of the device are used to build up a three-dimensional volume in which the Poisson equation is self-consistently solved, as depicted in Figure 4.1 (a). This is achieved by transferring the Poisson problem into a sparse matrix formulation and by applying the Newton algorithm combined with the successive overrelaxation method (compare Section 2.3). As a result, local charge carrier densities, local potentials and the resulting sheet conductance are calculated. Several phenomena are derived from the simulation results which are schematically outlined in Figure 4.1 (b). It is found that screening has a significant influence on the hole density distribution. Roughness in the range of one monolayer already reduces the sheet conductance by approximately 50%. The temperature dependence of the sheet conductance gives rise to the assumption that carriers rarely undergo thermally activated hopping, which is often assumed in a one-dimensional model. Instead, two-dimensional percolation pathways present within the first monolayer seem to dominate the charge transport. This work emphasizes the importance of smooth surfaces and initiated the idea of planarizing the paN with polystyrene and poly(meta methacrylate), as described in Section 3.1.3.

P. Riederer, M. Bouraoui and R. Kersting: Impact of surface roughness on conduction in molecular semiconductors. *Appl. Phys. Lett.* **120**, 112103 (2022); doi: 10.1063/5.0085778; licensed under a Creative Commons Attribution (CC BY) license.

Author contribution: P.R. and M.B. fabricated the samples. P.R. measured the AFM microscope images. P.R. evaluated the measured data. R.K. built the simulation software. P.R. and R.K. simulated the volume and evaluated the simulation data. R.K. supervised the study. P.R. and R.K. drafted the manuscript. All authors contributed with writing the final version of the manuscript.

Reprinted under the terms of the Creative Commons Attribution License (CC BY 4.0, <http://creativecommons.org/licenses/by/4.0/>), which permits unrestricted use and redistribution provided that the original author and source are credited.

# Impact of surface roughness on conduction in molecular semiconductors

Cite as: Appl. Phys. Lett. **120**, 112103 (2022); doi: [10.1063/5.0085778](https://doi.org/10.1063/5.0085778)

Submitted: 19 January 2022 · Accepted: 2 March 2022 ·

Published Online: 14 March 2022



P. Riederer,  M. Bouraoui,  and R. Kersting<sup>a)</sup> 

## AFFILIATIONS

Photonics and Optoelectronics Group, Faculty of Physics and Center for NanoScience (CeNS), Ludwig-Maximilians-Universität, Königstr. 10, 80539 München, Germany

<sup>a)</sup> Author to whom correspondence should be addressed: [roland.kersting@lmu.de](mailto:roland.kersting@lmu.de)

## ABSTRACT

The interface roughness between gate insulator and semiconductor is expected to reduce the conductance of molecular field-effect transistors. This study merges atomic force microscopy data of layer topographies with self-consistent calculations of charge carrier densities and conductances within the channel region. It is found that a roughness equivalent to one monolayer reduces the conductance by nearly 50%. Currents flow mainly within the first monolayer of the semiconductor and along percolation pathways, where charges rarely undergo transfers between adjacent monolayers.

© 2022 Author(s). All article content, except where otherwise noted, is licensed under a Creative Commons Attribution (CC BY) license (<http://creativecommons.org/licenses/by/4.0/>). <https://doi.org/10.1063/5.0085778>

Record charge carrier mobilities in molecular semiconductors are reported nearly every year and are currently approaching values where technical applications are coming within reach.<sup>1–4</sup> However, until now the mobilities in molecular field-effect transistors (FETs) have been much smaller than those in silicon devices, and the reasons are under debate. Discussed, for instance, are the small widths of the electronic bands of organic semiconductors,<sup>5,6</sup> polaronic effects,<sup>7,8</sup> dynamic localization of the charge carriers,<sup>9,10</sup> and the roughness of the gate insulator.<sup>11</sup>

Recent experimental work on molecular FETs has shown that an increased surface roughness of the gate insulator leads to a larger density of grain boundaries, which reduces the effective carrier mobility.<sup>12</sup> We report how roughness on its own diminishes the channel conductance. We will show that a root mean square (RMS) roughness equivalent to one monolayer reduces the conductance by about 50%. Currents mainly flow along percolation pathways within the first monolayer. Thermally activated transfers between monolayers rarely occur.

In the first step of this work, we investigate how surface roughness affects the distribution of free carriers within the molecular semiconductor at the interface to the gate insulator. In the second step, we conclude from the charge distribution on the conductance of the channel. Such a study would be challenging using exclusively experimental means, because the accumulation region is cladded between the gate insulator and semiconductor layers above, and thus, is not directly accessible. Therefore, we combine experimental data of the layers' surface topographies with self-consistent calculations of the interplay

between roughnesses, local potentials, and charge carrier distributions within the channel.

The layer topographies are recorded on devices as described in Ref. 13. Figure 1 displays the layer sequence. The gate contact is an 6 nm thick chromium layer, and the injection layer consists of 3 nm MoO<sub>x</sub> topped by 6 nm chromium. Both contacts, as well as the molecular semiconductor 2,7-dioctyl[1]benzothieno[3,2-b][1]benzothiophene (C<sub>8</sub>-BTBT-C<sub>8</sub>), are fabricated by physical vapor deposition. The gate insulator is obtained by chemical vapor deposition of parylene N.<sup>14</sup> The thicknesses of the insulator and of the C<sub>8</sub>-BTBT-C<sub>8</sub> are  $t_{ins} \approx 300$  and  $t_{sem} \approx 40$  nm, respectively. The topographies of the individual layers are obtained by atomic force microscopy (AFM). Typical RMS values are shown in Fig. 1. The most important value for this work is the roughness of the gate insulator  $\Delta z_{ims}$ .

The charge carrier distributions are calculated for volumes as illustrated in Fig. 1. We assume that a gate voltage is applied between bottom and top contact, which leads to the injection of holes from the top-contact and their accumulation at the interface between the C<sub>8</sub>-BTBT-C<sub>8</sub> semiconductor and the parylene N gate insulator. Two main effects define the distribution of free holes along this interface: (i) The applied voltage and the roughness of the interface cause potential wells where holes accumulate. Local hole densities can approach  $10^{19}$  cm<sup>-3</sup> as we show later. (ii) At such densities, strong Coulomb forces between the injected holes arise. They screen the electrostatic potentials, which in turn modifies the charge carrier distributions.

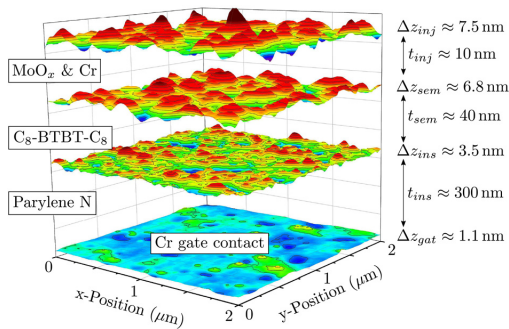


**FIG. 1.** Illustration of the layer topographies of the investigated structure. The thicknesses  $t_i$  of the layers are not to scale, but the roughnesses  $\Delta z_i$  are. All micrographs are recorded at different spots.

The overall potential landscape within the device is obtained by the self-consistent solution of the Poisson equation by considering the carrier statistics that regulate the local charge density.<sup>15</sup> Usually, Maxwell–Boltzmann statistics are applied. In this work, however, the Fermi energies approach the valence band and Fermi–Dirac statistics are appropriate. Volumes as illustrated in Fig. 1 are discretized by  $100 \times 100 \times 100$  nodes. The node spacing perpendicular to the layers is set to 4 nm, which is close to typical values for the long axes of unit cells found in molecular semiconductors with substituents, such as aromatic rings and long alkyl groups.<sup>16,17</sup> Within the layer plane, the nodes are 20 nm apart, which corresponds to the lateral resolution of the AFM data. Discretizing the Poisson problem leads to a sparse system of equations that can be solved by iterative methods. The computational costs are efficiently reduced by applying listing concepts.<sup>15,18</sup> All data presented are obtained using a damped Newton–Raphson algorithm combined with the method of successive overrelaxation.

Throughout this work, an external bias between the gate and the injection layer of  $V_{ext} = 50$  V is assumed, which leads to a sheet density of  $n_{2D} \approx 2 \times 10^{12} \text{ cm}^{-2}$  of accumulated holes. For all calculations, the effective mass of the holes is set to the free electron mass.<sup>19,20</sup> Between the molecular semiconductor and the  $\text{MoO}_x$  injection layer, a Schottky barrier of 0.2 eV is assumed. The relative permittivities of the insulator and the molecular semiconductor are set to 2.7 and 2.8, respectively.<sup>21–23</sup> However, these values change with the choice of materials; the selections made above are intended to overlap with previous studies on similar materials.

Figure 2 shows lateral cross sections through the simulated device within the interface region between the semiconductor and the insulator. Displayed are the material distribution (a), local potentials (b), and hole densities (c) and (d). In this particular calculation, the RMS roughness of the gate insulator is  $\Delta z_{ins} = 3.5$  nm, and the lattice temperature is set to  $T = 300$  K. The composition map in Fig. 2(a) illustrates the material inhomogeneity at the interface between the gate dielectric and the semiconductor. Figure 2(b) shows the local potential  $\phi$ , which is the superposition of the externally applied bias  $V_{ext}$  and the Coulomb potential due to accumulated holes around a specific node. The local valence band edge is  $E_{vb,loc} = E_{vb,mat} - e\phi$ , where  $E_{vb,mat}$  is the material's valence band edge. Thus, negative potentials

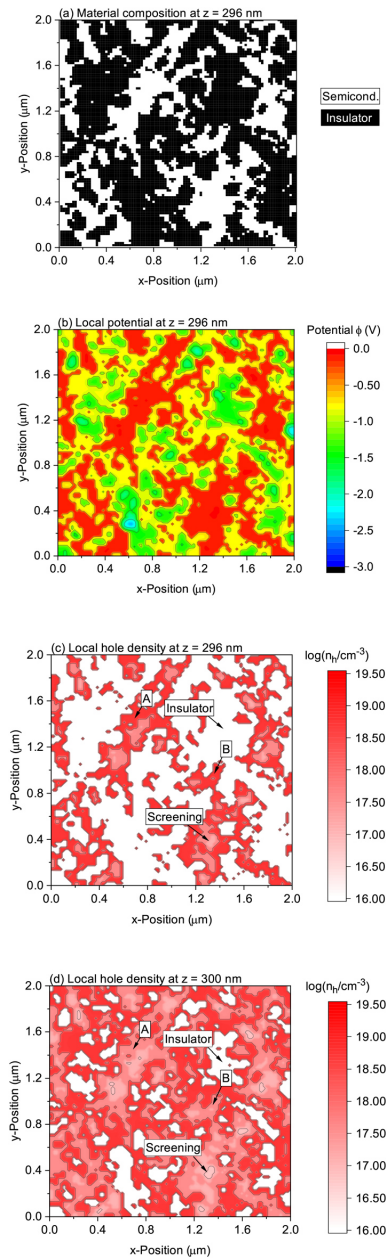


**FIG. 2.** Cross sections through the simulated volume at  $z = 296$  nm from the gate contact (a)–(c) and at  $z = 300$  nm (d). (a) Material composition. (b) Local potential  $\phi$ . (c) and (d) Local hole densities.

draw the valence band edge toward the Fermi energy, which leads to the accumulation of holes.

Local densities of accumulated holes  $n_h$  are shown in Fig. 2(c). Areas without any carriers mirror the insulator regions. All other areas can be attributed to potential wells of the semiconductor, as shown in Fig. 2(b). Within the wells, the charge carrier densities vary between  $10^{16}$  and  $10^{19}$  cm $^{-3}$ . These regions show one peculiarity caused by the Coulomb interaction between the injected holes. In nearly all of the red shaded regions, the hole density  $n_h$  is smaller near the center of the region than at its border. The high density of the holes screens the wells' potentials and draws the local band edges from the Fermi energy, which in turn reduces the charge densities within the wells. Further calculations not displayed here show that lateral screening reduces charge carrier densities within the puddles to about 50%.

One monolayer further apart from the interface, the holes cover nearly the entire cross section, as shown in Fig. 2(d). Only a few insulating islands remain. The hole densities displayed in Figs. 2(c) and 2(d) also illustrate the efficiency of Coulomb screening perpendicular to the layers. This becomes visible when comparing spots, such as those indicated by A and B. These regions have high charge carrier densities within the lower layer and drastically reduced densities one layer above.

Details of how the screened potential  $\phi$  affects valence band edges  $E_{vb,loc}$  and hole densities  $n_h$  are provided in Fig. 3. In equilibrium, the Fermi energy is constant across the device. The gradient of the band edge within the insulator mirrors the externally applied field. In contrast, the valence band within the semiconductor is nearly flat and close to the Fermi energy. At the maxima of the valence band, the hole densities approach  $10^{19}$  cm $^{-3}$ , as shown in Fig. 3(b). Such densities cause efficient field screening in the direction toward the injection layer. The carrier densities drop by orders of magnitude with increasing  $z$ , similar to those discussed for homogeneous layers.<sup>24</sup> One consequence is that the roughness of the interface with the insulator has a much bigger impact on transport properties than the roughness of the interface of the injection material. Therefore, in the following, we exclusively focus on the impact of the insulator roughness  $\Delta z_{ins}$  on charge transport.

According to the data of Fig. 3(b), about 95% of the charge carriers are accumulated within the first two monolayers, which corresponds to a layer thickness of about 8 nm. In this region, the local potential  $\phi$  shifts the valence band edge  $E_{vb,loc}$ , as illustrated in Fig. 4 along the plane of the interface. From one monolayer to the next, the potential changes by about 70 mV, equivalent to a shift of the band edge by nearly  $3 k_B T$ , when assuming room temperature. Thus, substantial thermal activation is needed for charge carrier transfers from lower to upper monolayers, whenever such a transfer is required for maintaining current flow between the potential wells. Previous work suggested that the charge transfer is limited by potential barriers between the wells.<sup>41</sup> This framework, however, applies to one-dimensional conductors rather than to two-dimensional surfaces where alternate percolation pathways may sustain conduction. Distinct percolation thresholds have been observed, for instance, in blends of molecular semiconductors and polymers.<sup>25</sup>

In order to determine the conductance along the channel, we assume that the local conductivity  $\sigma$  depends exclusively on the local density  $n_h$  at the particular node and the generic mobility  $\mu$ . For this local mobility, a value of 10 cm $^2/Vs$  is assumed, which is close to values

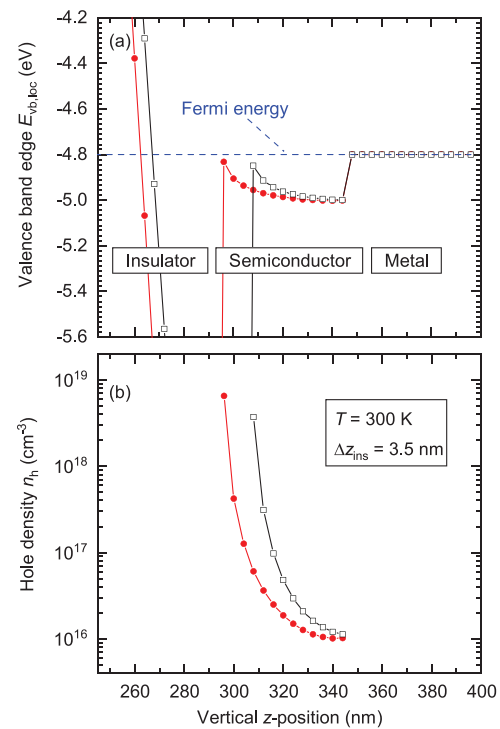


FIG. 3. Results for two distinct  $xy$ -positions, which are shown by the red dots and the open black boxes, respectively. (a) Valence band edges of the insulator and the semiconductor. For the metal, the Fermi energy is shown. (b) Hole density in dependence on the distance from the gate contact.

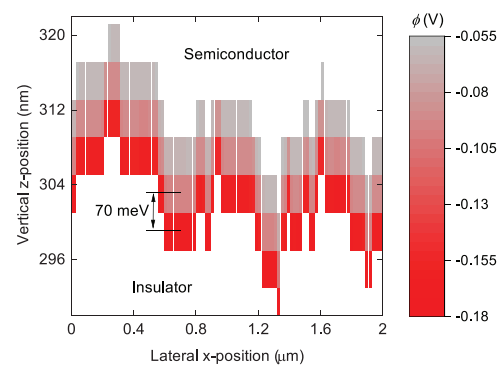
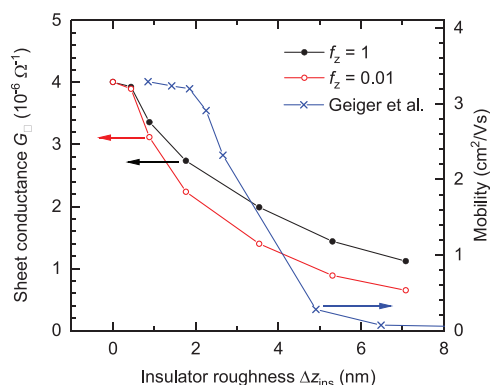


FIG. 4. Heat map of the local potential  $\phi$  for the first three semiconductor monolayers within the  $xz$ -plane. The heights and widths of the bars indicate the dimensions of the unit cells between the nodes.

measured, for instance, by terahertz spectroscopy.<sup>13,20</sup> The conductance between two nodes results from their local conductivities. Also included is thermal excitation according to a Maxwell-Boltzmann distribution if the potential difference  $\Delta\phi$  between the nodes requires this. Additionally, one may regard that many molecular semiconductors have reduced transfer integrals along the long axis of their unit cells, that is, for transfers between adjacent monolayers. This reduction in the transfer integrals is attributed by introducing the factor  $f_z$  that formally reduces the conductance between monolayers. Altogether, this approach describes a network of resistances, and solving the corresponding system of equations provides the sheet conductance  $G_{\square}$ . The impact of the roughness  $\Delta z_{\text{ins}}$  on  $G_{\square}$  is shown in Fig. 5 for  $f_z = 1$  and  $f_z = 0.01$ . For these calculations, the amplitude of the original AFM data is numerically varied, and the Poisson problem is solved for every roughness  $\Delta z_{\text{ins}}$ .

As expected, the sheet conductance  $G_{\square}$  decreases with the increasing surface roughness. Starting with a hypothetical perfect interface, the sheet conductance  $G_{\square}$  drops to 25% for  $\Delta z_{\text{ins}} \approx 7$  nm, which is equivalent to about two monolayers. Along a one-dimensional channel, this roughness would require frequent transfers with activation energies of several  $k_B T$ , and  $G_{\square}$  would diminish drastically. Thus, the moderate decay of  $G_{\square}$  with  $\Delta z_{\text{ins}}$  suggests that the macroscopic paths of the charge carriers rarely require thermal excitation. The cross sections of Fig. 2 reveal such conduction pathways over long distances. Consequently, the roughness of a two-dimensional channel has a reduced impact on the conductance  $G_{\square}$ . This notion is supported by conductance data obtained by setting  $f_z = 0.01$  in order to simulate small transfer integrals between adjacent monolayers. Despite this severe reduction, we observe only a disproportionate decrease in less than 50% in sheet conductance even for a roughness of  $\Delta z_{\text{ins}} \approx 7$  nm. Apparently, the vast majority of the inter-molecular charge transfers appear within the same monolayer.

The temperature dependence of the sheet conductance shown in Fig. 6 fits the understanding that charge carriers rarely have to hop between adjacent monolayers. With decreasing temperature  $T$ , the Fermi-Dirac distribution will further concentrate the charge carriers



**FIG. 5.** Calculated sheet conductance  $G_{\square}$  in dependence on the RMS roughness of the insulator at a lattice temperature of  $T = 300$  K (dots and circles). The reduction of the interlayer conductance is considered by the factor  $f_z$ . The crosses show experimental data of Geiger *et al.*<sup>12</sup>

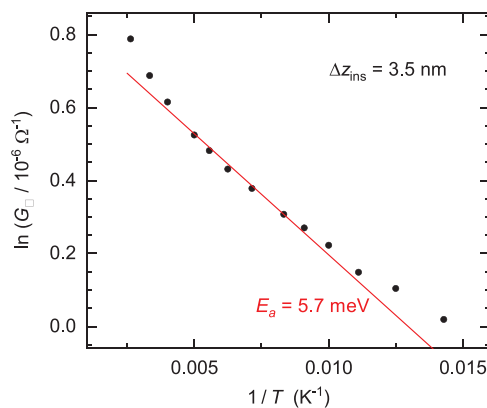


**FIG. 6.** Arrhenius plot illustrating the dependence of the sheet conductance  $G_{\square}$  on temperature  $T$  for a roughness of  $z_{\text{ins}} = 3.5$  nm and  $f_z = 1$ . The solid line fits the data with an activation energy of  $E_a = 5.7$  meV.

within the first monolayer. Thermally activated transfers of about 70 meV between adjacent monolayers will become less probable. For such transfers, an exponential relation between sheet conductivity  $G_{\square}$  and  $1/T$  is expected. However, the sheet conductances deviate from such an Arrhenius type behavior as indicated by the line in Fig. 6. Moreover, such a fit would produce unrealistic small activation energies of about 5.7 meV. The deviation from Arrhenius behavior and the small activation energy support the understanding that charge carriers rarely have to overcome potential barriers on their way across two-dimensional channels. Such percolation pathways appear in Figs. 2(c) and 2(d) as extended areas with high carrier density. The cross sections of (c) and (d) are separated by one monolayer. Thus, within these areas, the charge carriers can be transported within the same monolayer over distances of several hundred nanometers.

The calculated data in Fig. 5 show qualitative agreement with the experimental data of Geiger *et al.*<sup>12</sup> obtained on field-effect transistors of dinaphtho[2,3-b:2',3'-f]thieno[3,2-b]thiophene (DNTT) field-effect transistors. The authors report that as the roughness increases the DNTT grain sizes decrease. Thus, charge carriers frequently have to overcome grain boundaries, which reduces the device's mobility. The impact of grain boundaries was not considered in the present study. However, the comparison of calculated and experimental data suggests the following picture: At low surface roughness, the decrease in conductivity mainly results from surface roughness alone. With increasing roughness, the impact of grain boundaries takes over and drastically reduces sheet conductance within the channel region.

In conclusion, we accessed the impact of interface roughness on channel conductance in molecular field-effect devices. Experimental AFM data were merged with self-consistent calculations of local potentials and charge carrier distributions. The high concentration of charge carriers at the interface leads to strong Coulomb screening vertical to the layers, as well as within the plane of the interface. We found that an interface roughness of about one monolayer reduces sheet conductance by about 50%. This surprisingly moderate reduction can be

explained by conduction paths that rarely require charge transfers between the first monolayers of the organic semiconductor.

This research was funded by the Deutsche Forschungsgemeinschaft (DFG, German Research Foundation), Contract No. KE 516/11-1. The authors acknowledge discussions with A. Kadir and thank the authors of Ref. 12 for supporting this work with the experimental data shown in Fig. 5.

#### AUTHOR DECLARATIONS

##### Conflict of Interest

The authors have no conflicts of interest to disclose.

##### DATA AVAILABILITY

The data that support the findings of this study are available from the corresponding author upon reasonable request.

#### REFERENCES

- <sup>1</sup>H. Sirringhaus, *Adv. Mater.* **26**, 1319 (2014).
- <sup>2</sup>G. Schweicher, G. Garbay, R. Jouclas, F. Vibert, F. Devaux, and Y. H. Geerts, *Adv. Mater.* **32**, 1905909 (2020).
- <sup>3</sup>K. Takimiya, K. Bulgarevich, M. Abbas, S. Horiuchi, T. Ogaki, K. Kawabata, and A. Ablat, *Adv. Mater.* **33**, 2102914 (2021).
- <sup>4</sup>E.-K. Lee, M. Y. Lee, A. Choi, J.-Y. Kim, O. Y. Kweon, J.-H. Kim, J. Y. Jung, T.-J. Shin, J. H. Oh, J. I. Park, and S. Y. Lee, *Adv. Electr. Mater.* **3**, 1700142 (2017).
- <sup>5</sup>J. Cornil, J. P. Calbert, and J. L. Brédas, *J. Am. Chem. Soc.* **123**, 1250 (2001).
- <sup>6</sup>Y. C. Cheng, R. J. Silbey, D. A. da Silva Filho, J. P. Calbert, J. Cornil, and J. L. Brédas, *J. Chem. Phys.* **118**, 3764 (2003).
- <sup>7</sup>K. Hannewald, V. M. Stojanović, J. M. T. Schellekens, P. A. Bobbert, G. Kresse, and J. Hafner, *Phys. Rev. B* **69**, 075211 (2004).
- <sup>8</sup>A. F. Stassen, R. W. L. de Boer, N. N. Iosad, and A. F. Morpurgo, *Appl. Phys. Lett.* **85**, 3899 (2004).
- <sup>9</sup>A. Troisi and G. Orlandi, *J. Phys. Chem. A* **110**, 4065 (2006).
- <sup>10</sup>S. Fratini and S. Ciuchi, *Phys. Rev. Lett.* **103**, 266601 (2009).
- <sup>11</sup>S. Steudel, S. D. Vusser, S. D. Jonge, D. Janssen, S. Verlaak, J. Genoe, and P. Heremans, *Appl. Phys. Lett.* **85**, 4400 (2004).
- <sup>12</sup>M. Geiger, R. Acharya, E. Reutter, T. Ferschke, U. Zschieschang, J. Weis, J. Pflaum, H. Klauk, and R. T. Weitz, *Adv. Mater. Interfaces* **7**, 1902145 (2020).
- <sup>13</sup>T. R. Arend, A. Wimmer, G. Schweicher, B. Chattopadhyay, Y. H. Geerts, and R. Kersting, *J. Phys. Chem. Lett.* **8**, 5444 (2017).
- <sup>14</sup>S. Ganguli, H. Agrawal, B. Wang, J. F. McDonald, T. M. Lu, G.-R. Yang, and W. N. Gill, *J. Vac. Sci. Technol. A* **15**, 3138 (1997).
- <sup>15</sup>D. Sailer, A. Bornschlegl, and R. Kersting, *Appl. Phys. Lett.* **117**, 083301 (2020).
- <sup>16</sup>M. Abe, T. Mori, I. Osaka, K. Sugimoto, and K. Takimiya, *Chem. Mater.* **27**, 5049 (2015).
- <sup>17</sup>Y. Tsutsui, G. Schweicher, B. Chattopadhyay, T. Sakurai, J.-B. Arlin, C. Ruzié, A. Alier, A. Ciesielski, S. Colella, A. R. Kennedy, V. Lemaire, Y. Olivier, R. Hadji, L. Sanguinet, F. Castet, S. Osella, D. Dudenko, D. Beljonne, J. Cornil, P. Samorì, S. Seki, and Y. H. Geerts, *Adv. Mater.* **28**, 7106 (2016).
- <sup>18</sup>W. Hackbusch, *Iterative Solution of Large Sparse Systems of Equations* (Springer, 2016).
- <sup>19</sup>M. Ohtomo, T. Suzuki, T. Shimada, and T. Hasegawa, *Appl. Phys. Lett.* **95**, 123308 (2009).
- <sup>20</sup>S. G. Engelbrecht, M. Prinz, T. R. Arend, and R. Kersting, *Appl. Phys. Lett.* **105**, 012101 (2014).
- <sup>21</sup>C. Grigoriadis, C. Niebel, C. Ruzié, Y. H. Geerts, and G. Floudas, *J. Phys. Chem. B* **118**, 1443 (2014).
- <sup>22</sup>W. Choi, Y. Tsutsui, T. Sakurai, and S. Seki, *Appl. Phys. Lett.* **110**, 153303 (2017).
- <sup>23</sup>S. Sahin, N. K. Nahar, and K. Sertel, *Int. J. Infrared Millimeter Waves* **40**, 557 (2019).
- <sup>24</sup>G. Horowitz, in *Organic Electronics, Materials, Manufacturing, and Applications*, edited by H. Klauk (Wiley-VCH Verlag, 2006), Chap. 1, p. 3.
- <sup>25</sup>J. Smith, M. Heeney, I. McCulloch, J. N. Malik, N. Stingelin, D. D. Bradley, and T. D. Anthopoulos, *Org. Electr.* **12**, 143 (2011).

## 4.3 Degradation of Molecular Semiconductor Devices due to Field-Induced Gold Migration

One major disadvantage of organic semiconductors besides their low charge carrier mobility, is the phenomenon of performance degradation over time, also called operational instability. Several studies showed that during the application of a gate bias, the threshold voltage of organic FETs gradually increases with time, which is known as bias-stress effect [118]. While long-term stability is essential for commercial applications, mid-term stability is crucial for THz electromodulation spectroscopy investigations. Frequency resolved measurements require up to 24 hours of integration time to achieve reasonable smooth results. If the investigated thin-film devices exhibit severe degradation within this period of time, the resulting data cannot be interpreted correctly. Thus, device stability within these time-intervals are inevitable for frequency resolved THz electromodulation spectroscopy. Nevertheless, the origin of degradation and the bias-stress effect are widely discussed. Previous work suggest the role of water when a  $\text{SiO}_2$ -insulating layer is used [119]. Moreover, the choice of the gate dielectric seem to have an influence of this phenomenon [120]. Additionally, accelerated degradation is observed at elevated temperatures [121] or due to exposure to light [122], moisture and atmosphere [123]. Though, it has also been found that the bias-stress effect can be recovered by applying a reverse bias [121] a coherent explanation for these observations is still lacking.

Besides the choice of the insulator material, the choice of the injection contact material seem to have a huge influence on the overall device performance as well [124]. Gold (Au) is commonly used as a contact material but its influence on the devices' degradation is rarely considered [118, 122, 125, 126, 127].

Here, THz electromodulation spectroscopy is used to show that samples with Au containing contacts exhibit severe decrease of performance over time if a negative voltage is applied.

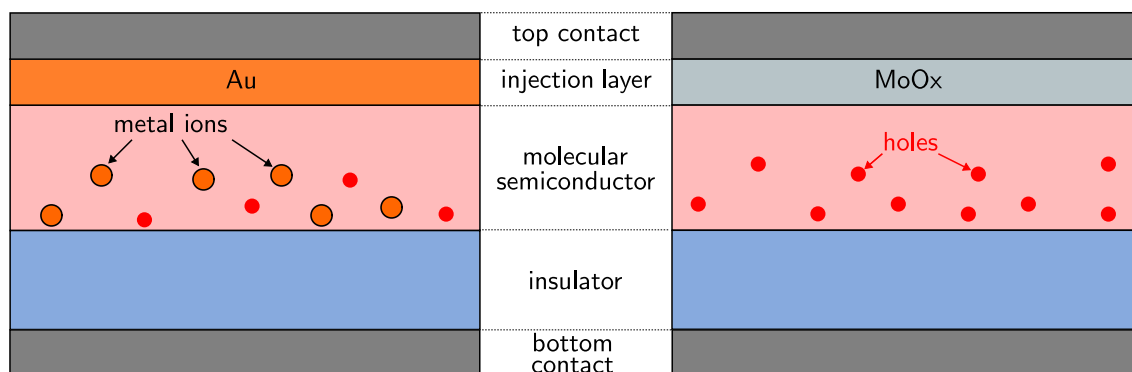


**Fig. 4.2** Schematic degradation principle of molecular semiconductor devices exhibiting Au contacts. Metal ions migrate into the OSC leading to a reduced density of mobile charge carriers (left). If MoOx is used instead of gold, this performance-degrading effect vanishes (right).

The partial reversibility of this phenomenon under positive bias supports the assumption that charged particles migrate into the devices' conducting channel. There, the metal ions act as defects (compare Figure 4.2) which results in a reduction of the density of mobile holes within the organic semiconductor. The theoretical lattice deformation energy necessary for the Au diffusion into C8-BTBT-C8 is in accordance with the measured voltage-independent thermal activation energies. By exchanging the Au with molybdenum oxide (MoO<sub>x</sub>), the degrading effects vanish.

These results facilitated the fabrication of devices with long-term stable performance. This stability is crucial for time intensive experiments such as frequency- or temperature-resolved THz electromodulation spectroscopy measurements.

P. Riederer, M. Bouraoui and R. Kersting: Field-induced migration of gold in molecular semiconductors. *Appl. Phys. Lett.* **120**, 243503 (2022); doi: 10.1063/5.0092224; licensed under a Creative Commons Attribution (CC BY) license.

Author contribution: P.R. and M.B. fabricated the samples. P.R. measured the data. P.R. evaluated the measured data. R.K. supervised the study. P.R. and R.K. drafted the manuscript. All authors contributed with writing the final version of the manuscript.

Reprinted under the terms of the Creative Commons Attribution License (CC BY 4.0, <http://creativecommons.org/licenses/by/4.0/>), which permits unrestricted use and redistribution provided that the original author and source are credited.

# Field-induced migration of gold in molecular semiconductors

Cite as: Appl. Phys. Lett. **120**, 243503 (2022); doi: [10.1063/5.0092224](https://doi.org/10.1063/5.0092224)

Submitted: 22 March 2022 · Accepted: 3 June 2022 ·

Published Online: 15 June 2022



P. Riederer,  M. Bouraoui,  and R. Kersting<sup>a)</sup> 

## AFFILIATIONS

Photonics and Optoelectronics Group, Faculty of Physics and Center for NanoScience (CeNS), Ludwig-Maximilians-Universität, Königstr. 10, 80539 München, Germany

<sup>a)</sup> Author to whom correspondence should be addressed: [roland.kersting@lmu.de](mailto:roland.kersting@lmu.de)

## ABSTRACT

We report on the degradation of field-effect devices due to the migration of gold from injection contacts into the channel region. The experimental results are obtained by THz spectroscopy on devices with a migration distance of 50 nm. The dependence of the degradation on gate voltage, as well as the partial reversibility, indicates that degradation is caused by field-induced transport of gold ions. The transport is found to be thermally activated with an activation energy independent of the field strength, which suggests that lattice deformations of the molecular semiconductor support the migration of gold.

© 2022 Author(s). All article content, except where otherwise noted, is licensed under a Creative Commons Attribution (CC BY) license (<http://creativecommons.org/licenses/by/4.0/>). <https://doi.org/10.1063/5.0092224>

The application of molecular semiconductors for future electronic and optoelectronic devices requires excellent electronic performance as well as sufficient stability and reliability of the components.<sup>1</sup> In organic field-effect transistors (FETs), degradation can cause changes in threshold voltages,<sup>2,3</sup> hysteresis,<sup>4</sup> and increased contact resistances.<sup>5,6</sup> Extrinsic factors that diminish device reliability often arise from contaminations acquired during fabrication or due to indiffusion from the environment during device operation. Identified were, for instance, residues of water<sup>7–9</sup> and oxygen.<sup>10,11</sup> Less is known about the deterioration of the FETs' contacts<sup>12</sup> and the associated ingress of contact materials such as metals.<sup>13,14</sup> In this work, we show that gold contacts on molecular semiconductors are prone to field-induced migration, whereas molybdenum oxide (MoO<sub>x</sub>) injection layers are much more stable. The electromigration of gold ions into the channel region reduces the density of mobile holes and increases the threshold voltage of field-effect devices.

Most organic FETs have a planar layout as illustrated in Fig. 1(a). Such structures offer a relatively large surface area for indiffusion of contaminants from the environment. Additionally, the transport toward the channel region is expedited by short distances, which rarely exceed 50 nm. In contrast, electromigration of metals from the source and drain contacts occurs along the channel length, which, in general, exceeds 1 μm. Thus, metal migration from the contacts can be expected to occur on longer timescales than indiffusion of contaminations from the surface. This makes definite studies of field-induced metal migration in FETs challenging. We, therefore, select devices as

illustrated in Fig. 1(b), which provide much better access to ion migration of metals, because the transport distance toward the sensitive channel region is only on the order of 50 nm.

As illustrated in Fig. 1(b), the impact of metal defects on the density of mobile holes can be measured by THz electromodulation spectroscopy.<sup>15</sup> Without metal migration, a negative gate voltage  $V_g$  causes the injection of holes into the molecular semiconductor and their accumulation at the interface to the insulator. As long as the holes are mobile, the conductance of this sheet of charge carriers can be probed by THz spectroscopy, because the carriers' Drude response reduces the THz transmission. In contrast, charged defects do not respond to THz radiation. Such defects are formed by metals that migrate from the injection contacts into the molecular semiconductor. Because the total charge of mobile holes and charged defects depends only on the applied gate voltage  $V_g$ , the ingress of metal ions reduces the density of mobile holes, which leads to an increase in THz transmission.

Devices as illustrated in Fig. 1 are fabricated on foils of polyethylene naphthalate (PEN). The active area of the structure has a diameter of 5 mm, which is about twice the spot diameter of the incident THz radiation. The gate contact is a 6 nm thick chromium layer deposited by physical vapor deposition (PVD) onto the PEN foil. The insulator consists of a 300 nm thick parylene N layer, which is fabricated by chemical vapor deposition.<sup>16</sup> The organic semiconductor is a 50 nm thick layer of 2,7-dioctyl[1]benzothieno[3,2-b][1]benzothiophene (C<sub>8</sub>-BTBT-C<sub>8</sub>).<sup>17</sup> It is deposited by PVD at a base pressure of 10<sup>-7</sup> mbar and at a rate of 0.2 Å/s. The injection layers consist either of (i) 2 nm

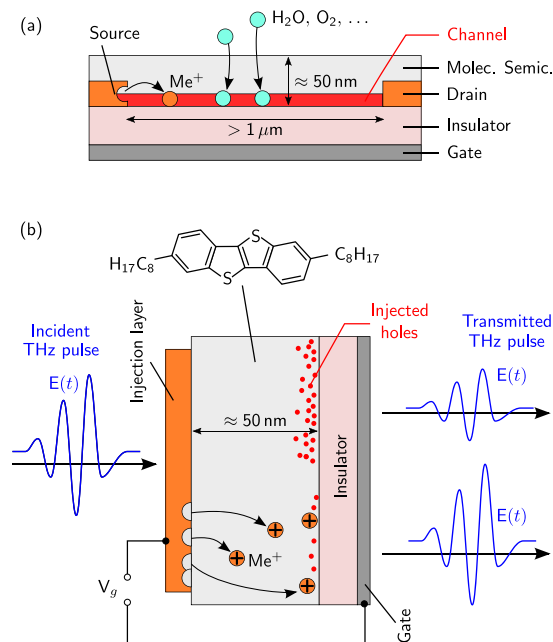


**FIG. 1.** Schematic and device dimensions of a typical organic FET (a). Illustration of the studied devices and of the measurement technique (b). Mobile holes reduce the transmission of the THz pulse by their Drude response. Electromigration of the injection layer material leads to positively charged metal defects within the semiconductor that reduce the density of mobile holes and, thus, enhance THz transmission.

of gold followed by 6 nm of chromium or (ii) 3 nm of  $\text{MoO}_x$  plus 6 nm of chromium. To minimize the thermal stress of  $\text{C}_8\text{-BTBT-C}_8$  during PVD of the injection layers, all injection materials are deposited in steps of 0.5 nm, followed by a deposition pause of 2 min. It is known that contamination by water during and after fabrication reduces the device performance.<sup>2,8</sup> Thus, prior to deposition of all layers, the devices are heated to 60 °C at  $10^{-7}$  mbar for several hours. Finally, the structures are sealed at a pressure of  $10^{-2}$  mbar with a 300 nm thick layer of parylene N for inhibiting indiffusion of oxygen and water after device fabrication.<sup>18,19</sup>

Details of the setup for time-resolved THz spectroscopy are described in the previous work.<sup>20</sup> Few-cycle THz pulses with a bandwidth of about 2.5 THz are time-resolved by electro-optic sampling.<sup>21</sup> All transmission measurements reported here are performed at the temporal peak of the THz pulses (see Fig. 1).

The relative change in the THz transmission signal  $\Delta S/S$  with gate voltage  $V_g$  is shown in Fig. 2. At negative  $V_g$ , holes are injected into the device, and the transmission decreases due to the Drude response of mobile holes. In contrast, a positive gate voltage does not change the transmission signal, as would be expected if mobile electrons were injected. This suggests that if electrons are injected at all, their Drude response can be neglected. In the case of hole injection,  $\Delta S/S$  follows linearly the slope of the applied voltage, but only after a threshold voltage  $V_{th}$  is reached. The threshold voltage increases on

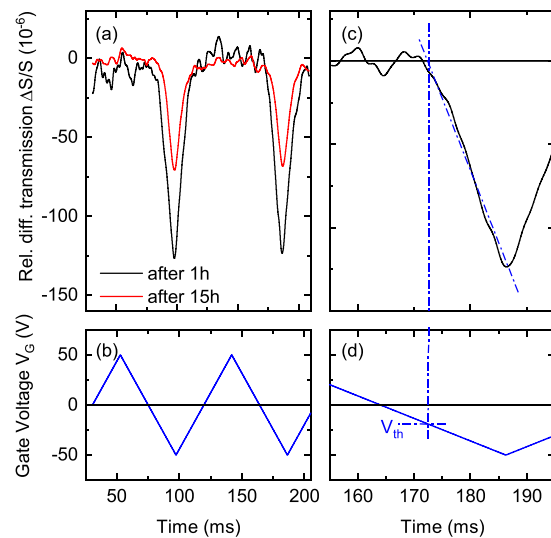


**FIG. 2.** Modulation of the THz transmission through a device with Au/Cr contacts. (a) Change of the relative differential THz transmission  $\Delta S/S$  after 1 h and after 15 h of operation. (b) Applied gate voltage. (c) and (d) Magnifications of (a) and (b), respectively. The blue dashed-dotted lines indicate the procedure for deducing the threshold voltage  $V_{th}$ .

the timescale of several hours. Within the first hour, the threshold voltage is  $V_{th} = 17$  V. After 5 h, the threshold is  $V_{5h} = 26$  V. In the following, we will show that the observed increase in the threshold voltage is caused by ion migration of gold into the  $\text{C}_8\text{-BTBT-C}_8$ . These charged defects lead to the build-up of a polarization field, which must be overcome prior to hole injection, as observed by the increase in the threshold voltage with operation time.

With every modulation cycle, the devices are charged with density  $n_{2D,mod}$ , which can be deduced from the capacitance per unit area  $\bar{C}$  of the structures. A gate voltage of  $V_g = -50$  V and  $\bar{C} = 6.1$  nF/cm<sup>2</sup> leads to  $n_{2D,mod} = 1.9 \times 10^{12}$  cm<sup>-2</sup>. The density of the mobile holes  $n_{2D}$  is deduced from the triangular modulation curves in Fig. 2 by considering the delayed onset due to the injection thresholds  $V_{th}$ . For the curve recorded after 1 h operation, the sheet density of mobile holes drops to  $n_{2D} = 0.7 \times 10^{12}$  cm<sup>-2</sup>, which is less than 40% of  $n_{2D,mod}$ . The difference is attributed to the polarization field due to charged defects. Similar values were reported in Ref. 22.

In order to obtain the sheet conductivity of the charge carriers within the device, electromodulation experiments are performed.<sup>15</sup> All data presented in the following are obtained by applying a square wave voltage, for instance, between +50 V and -50 V. For clarity, we describe this modulation by  $V_g = -50$  V, because negative bias injects holes into the channel region. Switching the gate voltage  $V_g$  changes the density of accumulated holes within the device and, thus, the THz transmission signal  $S$  by  $\Delta S$ . In a good approximation, the sheet conductivity  $\sigma_{2D}$  is related to the relative differential signal as<sup>23</sup>

$$\sigma_{2D} = \frac{-\Delta S}{S} \frac{2\sqrt{\epsilon_b}}{Z_0}, \quad (1)$$

where  $Z_0$  is the impedance of free space and  $\epsilon_b$  is the permittivity of the molecular semiconductor. The sheet conductivity  $\sigma_{2D}$  is extracted from  $\Delta S/S$  according to Eq. (1) using  $\epsilon_b = 2.8$ .<sup>24,25</sup> Figure 3 shows transients of  $\sigma_{2D}$  for two devices, one with an injection layer of  $\text{MoO}_x$  and another with a gold injection layer.

Already at the beginning of the measurements shown in Fig. 3, the sheet conductivity of the device with the gold injection layer is strongly reduced compared to the value measured for the  $\text{MoO}_x$  layer. This observation rules out degradation due to intercalated water and contamination by gases such as oxygen, because the Au/Cr devices as well as the  $\text{MoO}_x$ /Cr devices were fabricated using similar processes. As shown in Fig. 3, the initial conductivity of the gold devices is smaller than the conductivity of the  $\text{MoO}_x$  structures, which may be caused by the ingress of gold during deposition.<sup>14</sup> More interesting is that the conductivity with the gold injection layer rapidly decreases, whereas the decay of the  $\text{MoO}_x$  device is marginal. These differences show that gold migration causes the observed device degradation. The reason for the minor degradation of the  $\text{MoO}_x$  device is not accessible from the data available.

The THz transmission experiments probe the sheet conductivity of the channel  $\sigma_{2D} = e n_{2D} \mu$ , where  $n_{2D}$  is the sheet density of mobile holes and  $\mu$  is their mobility. The answer to the question of whether the observed degradation results from a reduction of  $n_{2D}$  or from a reduction of  $\mu$  cannot be derived from Fig. 4 alone. However, all experiments are performed at a modulation frequency of about 11 Hz. At such low frequencies, the contact resistances only marginally delay the injection and extraction of the holes, and the density of mobile holes is  $n_{2D} = C(V_g - V_{th})/e$ . This yields with Eq. (1) for the mobility

$$\mu = \frac{-\Delta S \frac{2\sqrt{\epsilon_b}}{Z_0}}{C(V_g - V_{th})}. \quad (2)$$

As shown in Fig. 2 the slopes of  $\Delta S/S$  are proportional to  $V_g - V_{th}$ , too. Thus,  $\mu$  is constant during degradation, which supports the notion that charged defects cause a polarization field that hinders the injection of mobile holes. Similar conclusions were drawn in Refs. 3 and 15.

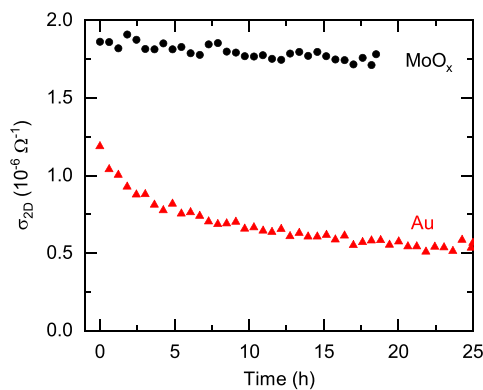


FIG. 3. Change in the sheet conductivity  $\sigma_{2D}$  with time. Data obtained on devices with a gold injection layer and with a  $\text{MoO}_x$  injection layer are shown by red triangles and black circles, respectively.

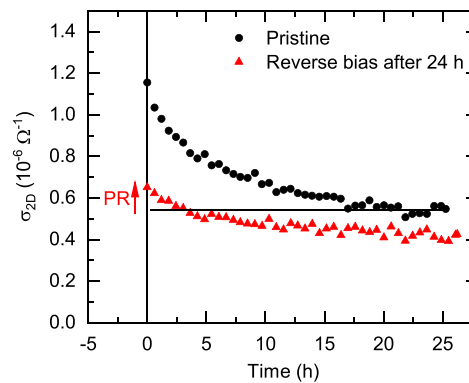


FIG. 4. Decay of the sheet conductivity  $\sigma_{2D}$  with operation time. Dots show the degradation of a pristine sample. Triangles show a repeated measurement on the same structure after a DC reverse bias of  $V_{rev} = +50$  V is applied for 24 h. The red arrow indicates the partial recovery (PR).

Figure 4 shows that the mechanism behind the degradation is the field-induced migration of gold out of the injection layer into the semiconductor. Within 20 h, the conductivity  $\sigma_{2D}$  of a pristine device diminishes by about 50%. The device performance, however, can be partially restored by applying a DC reverse voltage of  $V_{rev} = +50$  V for 24 h. Apparently, first, the field-induced transport of gold leads to the degradation of the device, and the following application of the reverse bias drives a part of the gold back from the channel region toward the injection layer. Because the electrical field within the device is homogeneous, only charged particles are subject to field-induced transport, which encourages usage of the term ion migration.

Investigating the temperature dependence of device degradation provides further insight.<sup>5,26-28</sup> Figure 5 shows that the degradation

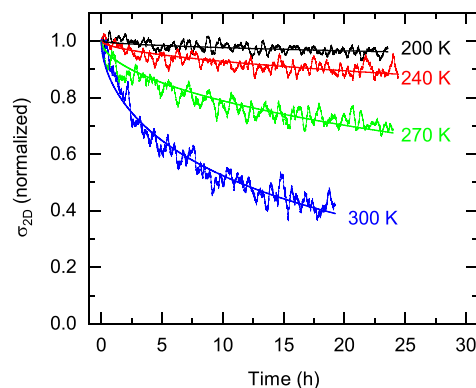


FIG. 5. Decay of the normalized sheet conductivity for different temperatures. Also shown are fits by a stretched exponential according to Eq. (3).

decelerates with decreasing temperature. At  $T = 200$  K, a degradation is barely visible within the first 24 h. For quantitative access, the experimental data are normalized and fitted by a stretched exponential<sup>2,3,29</sup>

$$\sigma_{2D}(t) = \sigma_0 \exp\left(-\left(\frac{t}{\tau}\right)^\beta\right), \quad (3)$$

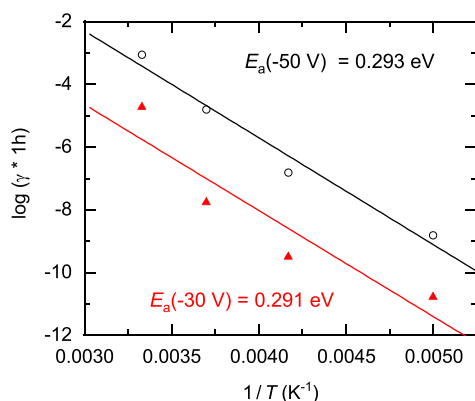
with time constant  $\tau$  and stretching factor  $\beta$ . Fitting the curve for  $T = 300$  K provides  $\beta = 0.575$ . Determining  $\tau$  along with  $\beta$  is impossible at lower temperatures, because the dynamics become too small. Although the dependence of  $\beta$  on temperature often provides valuable insight into the process of trap formation,<sup>30</sup> we use  $\beta = 0.575$  for  $T \leq 270$  K, too. The determined time constants range from  $\tau = 21$  h to  $\tau = 6700$  h for  $T = 300$  K and 200 K, respectively.

Figure 6 shows Arrhenius plots of the degradation rate  $\gamma = 1/\tau$  obtained at gate voltages  $V_g$  of  $-30$  V and  $-50$  V. For all temperatures, the rates obtained at  $V_g = -30$  V are about one order of magnitude smaller than those determined for  $V_g = -50$  V. Two conclusions can be drawn from this disproportionality: (i) the electric field within the devices is the driving force behind the degradation; (ii) the reactants involved in the degradation process are already abundant before the field-induced degradation begins. Otherwise, the field strength would have only a marginal effect on degradation, because the intake of contaminants would govern the degradation dynamics. This excludes, for instance, the indiffusion of water or oxygen, as can be expected for the studied devices, because they were sealed with parylene. This is also supported by the marginal degradation of the  $\text{MoO}_x$  device.

Because the observed decays of  $\sigma_{2D}(t)$  depend on temperature, the physical processes behind the time constants can be understood to be thermally activated,<sup>31</sup>

$$\tau = \tau_0 \exp\left(\frac{E_\tau}{k_B T}\right), \quad (4)$$

where  $E_\tau$  is the activation energy associated with  $\tau$ . Fitting the data of Fig. 4 provides for both gate voltages  $V_g$  nearly identical values of  $E_\tau(-30 \text{ V}) = 0.291 \pm 0.082$  and  $E_\tau(-50 \text{ V}) = 0.293 \pm 0.035$  eV.



**FIG. 6.** Dependence of the decay rate  $\gamma = 1/\tau$  on inverse temperature  $1/T$ . The datasets recorded at gate voltages of  $-30$  V and  $-50$  V are shown by triangles and circles, respectively. The solid lines show fits to the experimental data using the indicated activation energies.

From this result, we draw the following picture for migration of gold within the field: on their way toward the channel region, the gold ions are frequently trapped. The gold ions do not overcome the traps' barriers with the help of the driving field; otherwise, the activation energy  $E_\tau$  would depend on the field strength. Similar activation energies between 0.3 and 0.67 eV were reported for various other organic semiconductors, when gold electrodes were used.<sup>2,26,28,29</sup>

The geometrical dimensions of the semiconductor's lattice cells suggest a transport mechanism for gold that considers trapping and release of the gold ions on their way along the electric field. The unit cell's lattice constants of  $\text{C}_8\text{-BTBT-C}_8$  perpendicular to the field are  $a = 5.927$  and  $b = 7.880$  Å.<sup>32</sup> For a guest atom within the lattice, the available volume is further reduced by the second  $\text{C}_8\text{-BTBT-C}_8$  molecule within the unit cell. Good estimates for the gold's atomic and ionic diameters are  $d^0 \approx 4$  and  $d^+ \approx 3$  Å, respectively.<sup>33</sup> Although these values were deduced for distinctly different binding environments, it is obvious that the presence of gold leads to a severe deformation of the lattice. The transfer of gold between unit cells requires the target cell to provide the needed space. This lattice deformation requires a thermal activation with which we associate the observed value of  $E_\tau \approx 0.29$  eV. An extreme case of how gold changes the geometrical properties of the host material was reported by Grodd *et al.*<sup>12</sup> The authors observed with x-ray diffraction that indiffusion of Au into poly(3-hexylthiophene) leads to the formation of Au nanocrystallites within the host semiconductor. Such colloids are also known for enhancing oxidation in the presence of water and oxygen, for instance, observed on polysilanes.<sup>34</sup>

In conclusion, we reported on THz experiments that map the degradation of molecular field-effect devices due to ion migration of gold during device operation. The charged gold defects reduce the density of mobile holes and their sheet conductivity. Additionally, a polarization field is built up, which increases the threshold voltages with the operation time of the devices. The degradation of the devices strongly depends on the field strength between the injection layer and the gate contact. The deduced activation energies for migration of gold indicate that thermal excitation of lattice deformations of the semiconductor facilitates ion migration. Altogether, the results show that field-induced transport of metals from device contacts is a technological challenge on the way toward reliable FETs of molecular semiconductors.

This research was funded by the Deutsche Forschungsgemeinschaft (DFG, German Research Foundation), Contract No. KE 516/11-1.

#### AUTHOR DECLARATIONS

##### Conflict of Interest

The authors have no conflicts to disclose.

##### DATA AVAILABILITY

The data that support the findings of this study are available from the corresponding author upon reasonable request.

#### REFERENCES

- <sup>1</sup>H. Siringhaus, *Adv. Mater.* **21**, 3859 (2009).
- <sup>2</sup>S. G. J. Mathijssen, M. Cölle, H. Gomes, E. C. P. Smits, B. de Boer, I. McCulloch, P. Bobbert, and D. M. de Leeuw, *Adv. Mater.* **19**, 2785 (2007).
- <sup>3</sup>P. P. Cielecki, T. Leissner, M. Ahmadpour, M. Madsen, H.-G. Rubahn, J. Fiutowski, and J. Kjelstrup-Hansen, *Org. Electron.* **82**, 105717 (2020).

- <sup>4</sup>J. Tardy and M. Erouel, *Microelectron. Reliab.* **53**, 274 (2013).
- <sup>5</sup>R. A. Street, *Phys. Rev. B* **77**, 165311 (2008).
- <sup>6</sup>S. D. Wang, T. Minari, T. Miyadera, Y. Aoyagi, and K. Tsukagoshi, *Appl. Phys. Lett.* **92**, 063305 (2008).
- <sup>7</sup>C. Goldmann, D. J. Gundlach, and B. Batlogg, *Appl. Phys. Lett.* **88**, 063501 (2006).
- <sup>8</sup>H. L. Gomes, P. Stallinga, M. Cölle, D. M. de Leeuw, and F. Biscarini, *Appl. Phys. Lett.* **88**, 082101 (2006).
- <sup>9</sup>A. Tamayo, T. Salzillo, and M. Mas-Torrent, *Adv. Mater. Interface* **9**, 2101679 (2022).
- <sup>10</sup>A. Benor, A. Hoppe, V. Wagner, and D. Knipp, *Org. Electron.* **8**, 749 (2007).
- <sup>11</sup>T. Hallam, C. M. Duffy, T. Minakata, M. Ando, and H. Sirringhaus, *Nanotechnology* **20**, 025203 (2009).
- <sup>12</sup>L. S. Grodd, E. Mikayelyan, T. Dane, U. Pietsch, and S. Grigorian, *Nanoscale* **12**, 2434 (2020).
- <sup>13</sup>A. C. Dürr, F. Schreiber, M. Kelsch, H. D. Carstanjen, and H. Dosch, *Adv. Mater.* **14**, 961 (2002).
- <sup>14</sup>J. H. Cho, D. H. Kim, Y. Jang, W. H. Lee, K. Ihm, J.-H. Han, S. Chung, and K. Cho, *Appl. Phys. Lett.* **89**, 132101 (2006).
- <sup>15</sup>T. R. Arend, A. Wimmer, G. Schweicher, B. Chattopadhyay, Y. H. Geerts, and R. Kersting, *J. Phys. Chem. Lett.* **8**, 5444 (2017).
- <sup>16</sup>J. B. Fortin and T.-M. Lu, *Chemical Vapor Deposition Polymerization: The Growth and Properties of Parylene Thin Films* (Kluwer Academic Publishers, Boston/Dordrecht/New York/London, 2004).
- <sup>17</sup>P. Xie, T. Liu, J. Sun, and J. Yang, *Adv. Func. Mater.* **32**, 2200843 (2022).
- <sup>18</sup>G. W. Hyung, J. Park, J. H. Kim, J. R. Koo, and Y. K. Kim, *Solid-State Electron.* **54**, 439 (2010).
- <sup>19</sup>S. Nair, M. Kathiresan, T. Mukundan, and V. Natarajan, *Microelectron. Eng.* **163**, 36 (2016).
- <sup>20</sup>S. G. Engelbrecht, T. R. Arend, T. Zhu, M. J. Kappers, and R. Kersting, *Appl. Phys. Lett.* **106**, 092107 (2015).
- <sup>21</sup>Q. Wu and X.-C. Zhang, *Appl. Phys. Lett.* **67**, 3523 (1995).
- <sup>22</sup>W. Choi, T. Miyakai, T. Sakurai, A. Saeki, M. Yokoyama, and S. Seki, *Appl. Phys. Lett.* **105**, 033302 (2014).
- <sup>23</sup>S. G. Engelbrecht, M. Prinz, T. R. Arend, and R. Kersting, *Appl. Phys. Lett.* **105**, 012101 (2014).
- <sup>24</sup>C. Grigoriadis, C. Niebel, C. Ruzie, Y. H. Geerts, and G. Floudas, *J. Phys. Chem. B* **118**, 1443 (2014).
- <sup>25</sup>W. Choi, Y. Tsutsui, T. Sakurai, and S. Seki, *Appl. Phys. Lett.* **110**, 153303 (2017).
- <sup>26</sup>D. V. Lang, X. Chi, T. Siegrist, A. M. Sergent, and A. P. Ramirez, *Phys. Rev. Lett.* **93**, 076601 (2004).
- <sup>27</sup>T. Miyadera, S. D. Wang, T. Minari, K. Tsukagoshi, and Y. Aoyagi, *Appl. Phys. Lett.* **93**, 033304 (2008).
- <sup>28</sup>H. Lee, B. Moon, S. Y. Son, T. Park, B. Kang, and K. Cho, *ACS Appl. Mater. Interface* **13**, 16722 (2021).
- <sup>29</sup>H. L. Gomes, P. Stallinga, F. Dinelli, M. Murgia, F. Biscarini, D. M. de Leeuw, T. Muck, J. Geurts, L. W. Molenkamp, and V. Wagner, *Appl. Phys. Lett.* **84**, 3184 (2004).
- <sup>30</sup>S. C. Deane, R. B. Wehrspohn, and M. J. Powell, *Phys. Rev. B* **58**, 12625 (1998).
- <sup>31</sup>L. E. Benatar, D. Redfield, and R. H. Bube, *J. Appl. Phys.* **73**, 8659 (1993).
- <sup>32</sup>H. Kobayashi, N. Kobayashi, S. Hosoi, N. Koshitani, D. Murakami, R. Shirasawa, Y. Kudo, D. Hobara, Y. Tokita, and M. Itabashi, *J. Chem. Phys.* **139**, 014707 (2013).
- <sup>33</sup>*CRC Handbook of Chemistry and Physics*, edited by W. M. Haynes, D. R. Lide, and T. J. Bruno (CRC Press, 2014).
- <sup>34</sup>N. Nagayama, T. Maeda, Y. Sakurai, and M. Yokoyama, *Mol. Cryst. Liq. Cryst.* **316**, 411 (1998).

## 4.4 THz Spectroscopy of Band Transport in DBTTT Thin-Films

As introduced in Section 2.2, the mobility of a semiconductor is the relevant magnitude when comparing conductivity performances. The temperature dependence of the mobility gives information on dominant scattering mechanisms present within the OSC devices and thus on relevant charge transport phenomena [128]. The mobility extraction from transistor curves can lead to severe misinterpretation, due to the strong dependence on multiple different properties as for example device geometry, data selection, capacitance determination and contact resistance [129]. Thus, it is difficult to access the fundamental charge transport phenomena.

Here, temperature dependent and frequency resolved THz electromodulation spectroscopy measurements are combined to obtain unprecedented insight into the intrinsic charge transport mechanisms of molecular semiconductor thin-films. In thin-films of dibenzothiopheno[6,5-b:6',5'-f]thieno[3,2-b]thiophene (DBTTT), a  $T^{1/2}$  power law dependence of the mobility is observed. This gives rise to the assumption that carrier scattering at ionized impurities ( $T^{3/2}$ ) as well as phonon scattering ( $T^{-3/2}$ ) can be excluded as the main limiting factors. Furthermore, the experimental data from the frequency dependent measurements can only be put together with theoretical calculations by assuming a vastly decreased density of mobile holes. Apparently, merely a part of the injected charge carriers fulfills the Ioffe-Regel criterion and contributes to band transport. The majority of holes is either trapped or performs hopping transport. Thus, the estimated mobility values do not only depend on the injected charge carrier density, they rather depend on the fraction of mobile charges. These findings highlight that the mobility value is not a good figure of merit in comparing organic thin-film devices. Even if the density of injected carriers is known, a correct determination of the mobility is delicate.

P. Riederer, F. Devaux, G. Schweicher, Y. H. Geerts and R. Kersting: Molecular semiconductors and the Ioffe–Regel criterion: A terahertz study on band transport in DBTTT. *Appl. Phys. Lett.* **123**, 032103 (2023); doi: 10.1063/5.0153710; licensed under a Creative Commons Attribution (CC BY) license.

Author contribution: F.D. synthesized the DBTTT. P.R. fabricated the samples. P.R. measured the data. P.R. evaluated the measured data. R.K. supervised the study. P.R. and R.K. drafted the manuscript. G.S. and Y.H.G. reviewed the manuscript. All authors contributed with writing the final version of the manuscript.

Reprinted under the terms of the Creative Commons Attribution License (CC BY 4.0, <http://creativecommons.org/licenses/by/4.0/>), which permits unrestricted use and redistribution provided that the original author and source are credited.

# Molecular semiconductors and the Ioffe–Regel criterion: A terahertz study on band transport in DBTTT

Cite as: Appl. Phys. Lett. **123**, 032103 (2023); doi: [10.1063/5.0153710](https://doi.org/10.1063/5.0153710)

Submitted: 11 April 2023 · Accepted: 30 June 2023 ·

Published Online: 20 July 2023



P. Riederer,<sup>1</sup> F. Devaux,<sup>2</sup> C. Schweicher,<sup>2</sup> Y. H. Geerts,<sup>2</sup> and R. Kersting<sup>1,a)</sup>

## AFFILIATIONS

<sup>1</sup>Photonics and Optoelectronics Group, Faculty of Physics and Center for NanoScience (CeNS), Ludwig-Maximilians-Universität, Königinstr. 10, 80539 München, Germany

<sup>2</sup>Laboratoire de chimie des polymères, Faculté des Sciences, Université Libre de Bruxelles, ULB Boulevard du Triomphe, Brussels 1050, Belgium

<sup>a)</sup>Author to whom correspondence should be addressed: [roland.kersting@lmu.de](mailto:roland.kersting@lmu.de)

## ABSTRACT

Terahertz electromodulation spectroscopy provides insight into the physics of charge carrier transport in molecular semiconductors. The work focuses on thin-film devices of dibenzothiopheno[6,5-b:6',5'-f]thieno[3,2-b]thiophene. Frequency-resolved data show a Drude-like response of the hole gas in the accumulation region. The temperature dependence of the mobilities follows a  $T^{1/2}$  power law. This indicates that the thermal mean free path of the charge carriers is restricted by disorder. Only a fraction of approximately 5% of the injected carriers fulfills the Ioffe–Regel criterion and participates in band transport.

© 2023 Author(s). All article content, except where otherwise noted, is licensed under a Creative Commons Attribution (CC BY) license (<http://creativecommons.org/licenses/by/4.0/>). <https://doi.org/10.1063/5.0153710>

Several factors limit the charge carrier transport in the accumulation region of organic field-effect devices. These can be intrinsic material properties, such as small orbital overlap between semiconductor molecules or phonon scattering, and extrinsic factors, such as impurities or the dielectric roughness at the interface to the gate insulator. Studies on field-effect transistors (FETs) have shown that the interface roughness due to static disorder strongly reduces mobility.<sup>1–3</sup> Furthermore, random dipole fields within the channel region scatter charge carriers.<sup>4,5</sup> Structural disorder within the first monolayers may also limit transport.<sup>6,7</sup>

Temperature-resolved measurements of the mobility  $\mu$  help to identify the dominant scattering mechanisms by their characteristic temperature dependencies, for instance,  $\mu \sim T^{3/2}$  for scattering at ions and  $\mu \sim T^{-3/2}$  for phonon scattering. Terahertz electromodulation spectroscopy facilitates temperature-resolved studies of charge transport in organic semiconductors.<sup>8</sup> The technique provides access to band transport, but is insensitive to slow transport processes, such as hopping. In this work, we present a terahertz (THz) study on field-effect devices made of dibenzothiopheno[6,5-b:6',5'-f]thieno[3,2-b]thiophene (DBTTT).<sup>9</sup> Hole mobilities of up to  $\mu = 3 \text{ cm}^2/\text{Vs}$  are found. Frequency-resolved data indicate that the band transport of the carriers is limited by disorder in the accumulation region. This is

consistent with the temperature dependence of the mobility, which follows  $\mu \sim T^{1/2}$ . The results show that most charge carriers do not participate in band transport. Their mean free paths do not satisfy the Ioffe–Regel criterion.

Figure 1(a) illustrates the conceptual outline of THz electromodulation spectroscopy. Few-cycle THz pulses are transmitted through field-effect devices that comprise an injection layer, a semiconductor thin film, an insulator, and a gate contact. With the application of a gate voltage  $V_g$ , charge carriers are injected into the device and accumulate at the interface between the semiconductor and the insulator. In the case of DBTTT, only holes can be injected. They respond to the AC field of the THz pulses and cause absorption and dispersion of the transmitted radiation. Switching the applied voltage  $V_g$  yields a differential transmission signal  $\Delta S$ , which provides the charge carriers' sheet conductance  $\sigma_{2D}$  and mobility  $\mu$ .<sup>8</sup>

Field-effect structures, as illustrated in Fig. 1(b), are fabricated on 0.5 mm-thick sapphire dies and on 125  $\mu\text{m}$ -thick foils of polyethylene naphthalate (PEN). Devices on PEN are advantageous, because its small index of refraction supports the transmission of THz radiation. Temperature-resolved experiments require good heat conduction and are performed on devices with sapphire substrates.

24 July 2023 07:43:39

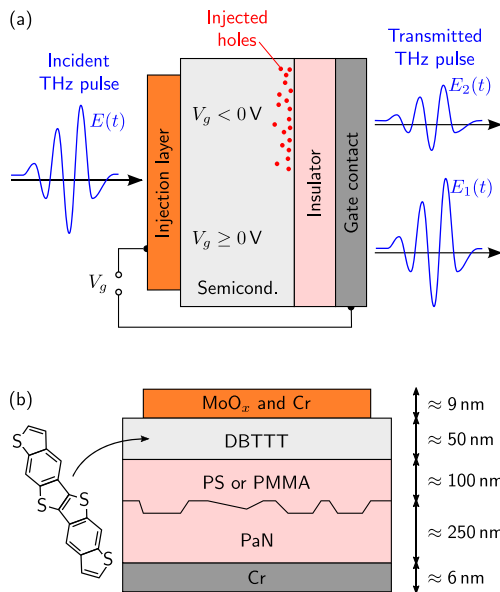


**FIG. 1.** Illustration of the method of THz electro-modulation spectroscopy (a). Schematic device architecture (b).

The devices' injection contacts consist of  $\text{MoO}_x$  and Cr, and the gate contacts are made of Cr. Typical thicknesses of the layers are between 6 and 9 nm, which permits the sufficient transmission of THz radiation. The insulator parylene N (PaN) is deposited by chemical vapor deposition. Pinhole-free films are obtained for thicknesses exceeding 250 nm. These films, however, have an RMS roughness of approximately 5 nm, which leads to an inhomogeneous growth of DBTTT when deposited on top (supplementary material, Figs. S1 and S3). Therefore, the PaN is planarized by spin coating of polystyrene (PS) or poly(methyl methacrylate) (PMMA). The PS and PMMA have average molecular weights of 10 and 950 kDa, respectively. A 1.5 wt. % solution in toluene for the PS film and a 2 wt. % solution in dichlorobenzene for the PMMA are used. The solutions are spin coated at 3000 rpm onto the PaN and then dried at 140 °C for 2 h. The thickness of the planarization layers is approximately 50 nm. Planarization with PS and with PMMA reduces the RMS roughness of the gate insulator to 1.2 nm. The chromium gate contact, the injection layer, and the DBTTT are deposited by physical vapor deposition at  $p \approx 5 \times 10^{-7}$  mbar, with deposition rates of approximately 0.1 Å/s. All DBTTT films are polycrystalline and have a thickness of approximately 50 nm. The devices have active areas of 28 mm<sup>2</sup> and unit capacitances of  $\bar{C} \approx 7.2$  nF/cm<sup>2</sup>.

Terahertz electromodulation experiments are performed with few-cycle THz pulses that have a bandwidth of 2.6 THz. The details of the experimental setup can be found in Ref. 8. Figure 2 shows the relative differential transmission  $\Delta S/S$  of THz radiation during the modulation of the applied voltage  $V_g$ . The data are recorded at the temporal peak of the THz pulse (see Fig. 3). Figure 2 shows that at  $V_g < 0$ , holes

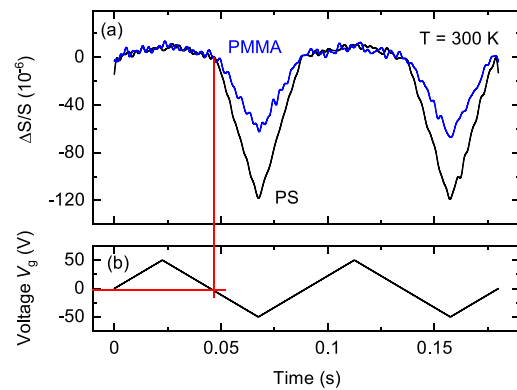


**FIG. 2.** Dependence of the relative differential THz signal  $\Delta S/S$  on the modulation voltage  $V_g$  recorded at  $T = 300$  K. Data obtained on structures with a PMMA interlayer and a PS interlayer are shown in (a) by blue and black lines, respectively. Applied modulation voltage  $V_g$  between bottom and top contact (b). The red lines indicate that the threshold voltage  $V_{th}$  is marginal.

are injected into the DBTTT and accumulate at the interface to the insulator. Their response to the THz field reduces the transmission signal by  $\Delta S$ . An injection of mobile electrons at  $V_g > 0$  is not observed.

The sheet conductance of the injected charge carriers can be obtained from the data in Fig. 2 using an equivalent of Tinkham's formula:<sup>10,11</sup>

$$\sigma_{2D} = e \mu n_{2D} = -\frac{\Delta S}{S} \cdot \frac{2\sqrt{\epsilon_b}}{Z_0}, \quad (1)$$

where  $\epsilon_b$  is the relative permittivity of the layer,  $Z_0$  is the impedance of free space,  $e$  is the elementary charge, and  $n_{2D}$  is the modulated two-dimensional charge carrier density. The sheet density of injected holes  $n_{2D,inj}$  is calculated from  $V_g$  and  $\bar{C}$ . For example, a gate voltage of  $V_g = -50$  V leads to  $n_{2D,inj} \approx 2.2 \times 10^{12}$  cm<sup>-2</sup>. Assuming that all injected holes are mobile, their mobility is given by  $\mu_{inj} = \sigma_{2D}/(e n_{2D,inj})$ , which provides  $\mu_{inj} = 3.0$  cm<sup>2</sup>/V s for devices planarized

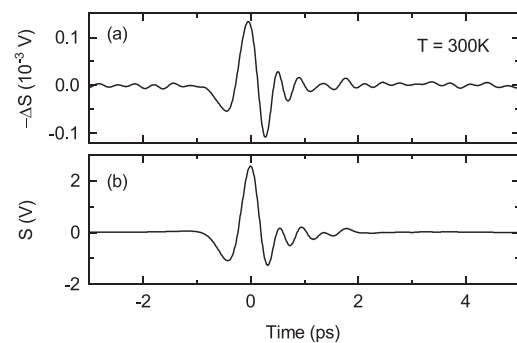


**FIG. 3.** Time-resolved THz transmission through DBTTT on PS. (a) Differential signal  $\Delta S$  due to the injection of holes. (b) Transmitted THz signal  $S$ .

with PS and  $\mu_{inj} = 1.5 \text{ cm}^2/\text{V s}$  for the ones planarized with PMMA. Similar values have been reported for DBTTT FETs.<sup>9</sup>

Although the PS layer and the PMMA layer have similar surface roughness, the measured mobilities differ by a factor of 2. This observation agrees with previous works,<sup>4,5,12</sup> wherein it is attributed to the different dielectric properties of PS and PMMA, which have relative permittivities of  $\epsilon = 2.6$  and  $\epsilon = 3.0$ , respectively. An increased permittivity reduces the mobility,<sup>4,5</sup> presumably because random dipoles within the insulator broaden the semiconductors' density of states at the interface. A recent study concludes that the polarity of the insulator reduces the mobility.<sup>12</sup> The mobilities for PS and PMMA surfaces reported in Ref. 12 show nearly the same ratio as the values obtained from the data in Fig. 2.

Despite the agreement with the above works, one fundamental question has not been addressed: Are all of the injected charge carriers mobile and contribute to band transport? If only a part of the injected carriers were mobile ( $n_{2D,mob} < n_{2D,inj}$ ), the mobility of these carriers increases according to  $\mu_{mob} = \sigma_{2D}/(e n_{2D,mob})$ . Insight is gained by analyzing the frequency dependence of the carriers' AC conductivity, for which we assume band transport, because typical hopping conductivities are too small to be observed in our THz experiments. Various transport models have been applied for interpreting the THz response of charge carriers in organic semiconductors, among which are the fundamental Drude model,<sup>13,14</sup> the Drude–Smith model,<sup>15,16</sup> the localization-modified Drude model,<sup>17–19</sup> and the Drude–Anderson model.<sup>20–22</sup> A brief discussion of the applicability of these models is given in the supplementary material. Only the classical Drude model fulfills the requirements and provides a reasonable agreement with the experimental data, as shown by Fig. S9 of the supplementary material. Thus, we use this model as the most reasonable approach for describing charge transport.

For a Drude response with momentum relaxation time  $\tau$ , the sheet conductivity is as follows:

$$\sigma_{2D}(\omega) = \frac{n_{2D} e^2 \tau}{m_h^*} \cdot \frac{1 + i \omega \tau}{1 + \omega^2 \tau^2}. \quad (2)$$

Terahertz spectroscopy can resolve this frequency dependence by recording transmission changes in the time domain, followed by Fourier transformation.<sup>23</sup> Figure 3 shows time-resolved transmission data recorded at room temperature. The differential signal  $\Delta S$  is obtained by square-wave modulation with  $V_g = \pm 50 \text{ V}$  at frequencies of approximately 10 Hz. Compared to the transmitted signal  $S$ , the transmission change  $\Delta S$  is minute, which illustrates the weak interaction between THz radiation and the mobile holes.

Fourier transforms of the experimental data of  $\Delta S/S$  are shown in Fig. 4 by the symbols. The solid lines in Fig. 4 are fits to the experimental data and consider a Drude response, as described in Eq. (2). The same parameter sets of Drude scattering time  $\tau$  and sheet density  $n_{2D}$  are used for both the real part and the imaginary part of  $\Delta S/S$ . For the hole's effective mass,  $m_h^* = m_e$  is used.<sup>24</sup> A description of the analysis of  $\Delta S/S$  can be found in the supplementary material or in Ref. 8. The carrier mobilities are deduced from the fit parameter  $\tau$  using  $\mu = e \tau / m_h^*$ .

A reasonable agreement between experimental data and calculations can only be achieved if a strongly reduced density of mobile carriers is assumed (compared to Fig. S8 of the supplementary material). The solid lines in Fig. 4 show calculations for  $n_{2D,mob} = 0.05 \cdot n_{2D,inj}$ .

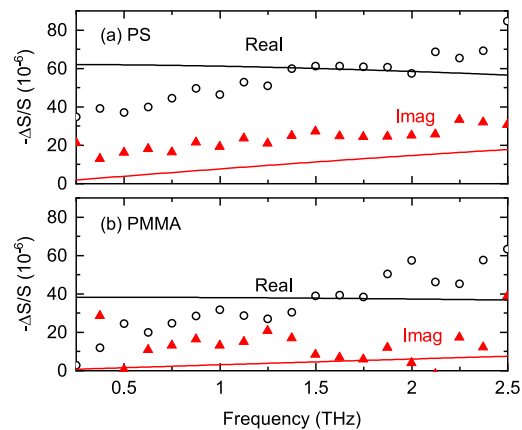
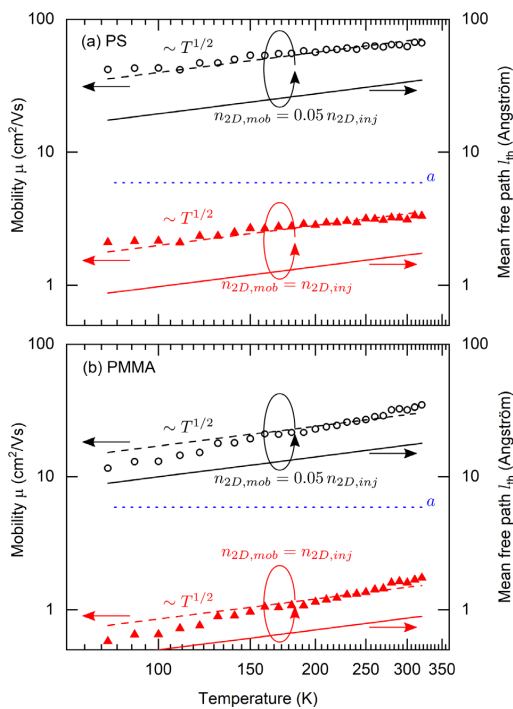


FIG. 4. Frequency dependence of the relative differential transmission  $\Delta S/S$  for DBTTT on PS (a) and for DBTTT on PMMA (b) recorded at  $T = 300 \text{ K}$ . The real and imaginary parts of  $\Delta S/S$  are depicted by black circles and by red triangles, respectively. Fits to the experimental data are shown by black lines and red lines for the real and imaginary parts, respectively.

Under this assumption, Drude mobilities for this fraction of charge carriers of  $\mu = 35$  and  $\mu = 23 \text{ cm}^2/\text{V s}$  are deduced for the devices planarized with PS and PMMA, respectively. For these extrapolations, the same fraction of 5% is assumed for PS and PMMA. The value of 5% has large error margins, and more precise values are unreasonable. However, the findings indicate that charge transport mainly results from a small fraction of the injected charge carriers, whereas most carriers have no significant contribution to transport. They may be trapped or perform hopping transport, both of which are not accessible in THz experiments. A recent work considers the Boltzmann transport equation in conjunction with the most dominating scattering process and concludes that even mobile carriers may be immobilized by strong scattering.<sup>25</sup> The authors discuss a transport reduction factor, which may be related to our observation that only a small fraction of the charge carriers participates in transport.

Temperature-resolved measurements support the framework that only a fraction of charge carriers participates in band transport. The experimental data in Fig. 5 are obtained by recording  $\Delta S/S$  at the temporal peak of the THz pulse and by modulating the device with a square wave of  $V_g = \pm 50 \text{ V}$ . The observed temperature dependencies result from the THz response of the injected holes and not from the temperature dependence of the injection process: The slopes of the transmission changes in Fig. 2 are linear, even at low temperatures. This indicates that the transfer across the injection interface is faster than the modulation and does not cause the temperature dependencies in Fig. 5. Measurements in the dependence of the modulation frequency confirm this.

The mobilities shown in Fig. 5 are deduced for two cases: (i) by assuming that all injected carriers contribute to the THz signal (red triangles) and (ii) by considering that only a fraction  $n_{2D,mob} \approx 0.05 \cdot n_{2D,inj}$  of the injected carriers is mobile (black circles). The dashed red and black lines are fits that follow the power law  $\mu \sim T^{1/2}$ . Both the



**FIG. 5.** Temperature dependence of the mobilities in DBTTT deposited on PS (a) and PMMA (b). Mobilities are obtained from  $\Delta S/S$  by assuming either  $n_{2D,mob} = n_{2D,inj}$  or  $n_{2D,mob} = 0.05 \cdot n_{2D,inj}$  and are displayed by red triangles and black circles, respectively. The dashed lines follow  $\mu \sim T^{1/2}$  and serve as visual guides. The solid lines show the temperature dependence of the thermal mean free path  $\ell_{th}$  for the above densities. The blue dotted line indicates the size of the unit cell  $a$ .

mobilities obtained on the PS structures and on those of PMMA structures follow this dependence. This behavior clearly distinguishes from the dependence of  $T^{-1/2}$  or  $T^{-3/2}$ , which is expected for dynamic localization and phonon scattering, respectively.<sup>26</sup>

The observed  $T^{1/2}$  power law of the mobilities can be explained by a reduced mean free path of the charge carriers due to disorder. According to the Ioffe–Regel criterion, extended Bloch waves can only exist if the carriers’ thermal mean free path  $\ell_{th}$  exceeds the size of the unit cell  $a$ .<sup>27,28</sup> In an accumulation layer with areas of different degrees of disorder, only regions with  $\ell_{th} > a$  support band transport. Only here, charge carriers can exhibit a Drude response. In regions where  $\ell_{th}$  does not fulfill the Ioffe–Regel criterion, charge carrier transport is limited to hopping. Thus, THz experiments access only those regions where charge carriers have sufficient mean free path. However, even in these high-mobility regions, diagonal disorder increases the width of the density of states,<sup>4</sup> which in turn partially limits the carrier’s mean free path.

Disorder is unintentionally introduced during the deposition of the molecular semiconductor or may result from the interface

roughness of the insulator<sup>3,29</sup> or from its dielectric disorder.<sup>4</sup> Independent of the origin of disorder, it limits the thermal mean free path  $\ell_{th} = v_{th}\tau$ , which can be expressed by the mobility as

$$\ell_{th} = \frac{\mu}{e} \sqrt{2k_B T m_h^*}, \quad (3)$$

when assuming a two-dimensional carrier gas at the interface to the insulator. The experimental mobility data and the calculations of the mean free paths in Fig. 5 follow the same temperature dependence  $T^{1/2}$ . This indicates that properties of the mean free path control the observed mobility.

The calculations of the mean free path  $\ell_{th}$  in Fig. 5 are based on the room-temperature mobilities of the devices and on the extrapolation of the temperature dependence according to Eq. (3). Two cases are considered: (i) that all injected charge carriers are mobile (red solid lines) and (ii) that  $n_{2D,mob} = 0.05 \cdot n_{2D,inj}$  (black solid lines). Furthermore, the dotted blue lines indicate the lattice constant  $a = 5.91 \text{ \AA}$  of DBTTT.<sup>30</sup> For both of the investigated structures,  $\ell_{th} < a$  when considering for the mobile carrier density  $n_{2D,mob} = n_{2D,inj}$ . This, however, would not fulfill the Ioffe–Regel criterion, and a THz signature of the charge carriers would not be observable, which contradicts the experimental results, such as in Figs. 2–4. One option to resolve this contradiction is to assume a spatially inhomogeneous semiconductor, comprised of regions where  $\ell_{th} > a$  as well as of regions with  $\ell_{th} < a$ . Thus, only a part of the injected carriers exhibit band transport and contribute to the THz signal, for which classical Drude transport can be assumed. The others perform hopping transport and are not detected in the THz experiments. The calculations of Fig. 5 show that  $\ell_{th}$  exceeds the lattice constant when assuming that only 5% of the charge carriers contribute to the mobility. Only these 5% fulfill the Ioffe–Regel criterion and participate in band transport. The density of interface defects, which localize charge carriers, can spread over a wide range, and even for single crystals, values between  $0.7 \times 10^{10}$  and  $2 \times 10^{12} \text{ cm}^{-2}$  have been reported.<sup>31,32</sup> Thus, the observation that only 5% of the charge carriers participate in band transport is plausible.

Altogether, the result that only a fraction of the injected charge carriers participates in band transport is derived from the following observations: (i) the spectral response of the charge carriers (Fig. 4). The agreement between the experimental data and calculation requires that  $n_{2D,mob} < n_{2D,inj}$ . (ii) The temperature dependence of the mobilities follows a  $T^{1/2}$  power law (Fig. 5). This shows that the dominating scattering process is not phonon scattering, for which  $\mu \sim T^{-3/2}$  is expected. Also, the dynamic localization can be excluded, for which temperature dependencies between  $\mu \sim T^{-3/2}$  and  $\mu \sim T^{-1/2}$  are expected.<sup>26</sup> This leaves disorder scattering as the most potential process that limits the mobility. Disorder scattering may arise because of structural disorder of the semiconductor<sup>1–3</sup> and because of local fields within the insulator.<sup>4,5</sup> In areas where potential fluctuations occur on the scale of few unit cells, disorder leads to localization and reduces the fraction of mobile carriers that perform band transport. (iii) The result is that the mean free paths do not exceed the size of the unit cell when assuming that all carriers contribute to band transport (Fig. 5). In this case, the Ioffe–Regel criterion would not be fulfilled and band transport would be impossible. Overall agreement with the experimental data can be achieved under

the assumption that only a fraction of the injected carriers participates in band transport.

The result that disorder excludes most of the injected carriers from band transport underpins the technological importance of improving the interfacial properties between insulator and semiconductor. High-mobility devices of molecular thin films may require surface engineering of the interface, such as by the functionalization and planarizing of the insulating layer,<sup>33,34</sup> the use of self-assembled monolayers,<sup>35,36</sup> or the fabrication of semiconductor heterostructures.<sup>37–39</sup>

In summary, we investigated charge transport in DBTTT field-effect devices utilizing THz electromodulation spectroscopy. Mobilities of 3.0 and 1.5 cm<sup>2</sup>/V s are found for DBTTT deposited on PS and PMMA, respectively, assuming that all injected charge carriers contribute to band transport. However, frequency-resolved data and temperature-resolved data indicate that only a fraction of the injected charge carriers participates in band transport. The vast majority is either trapped or performs hopping transport. Their mean free paths are smaller than the semiconductor's unit cell, which violates the Ioffe–Regel criterion and excludes them from band transport. Mobility estimates for the fraction of carriers that fulfill the Ioffe–Regel criterion lead to values above 20 cm<sup>2</sup>/V s.

See the supplementary material for details on the device architecture, thin-film topographies, data analysis, and other transport models.

This research was funded by the Deutsche Forschungsgemeinschaft (DFG, German Research Foundation) (Contract No. KE 516/11-1). G.S. thanks the Belgian National Fund for Scientific Research (FNRS) for financial support through research project COHERENCE2 no. F.4536.23. G.S. is a FNRS Research Associate. G.S. acknowledges the financial support from the Francqui Foundation (Francqui Start-Up Grant). Y.G. is thankful to FNRS for financial support through research projects Pi–Fast (No. T.0072.18) and Pi–Chir (No. T.0094.22).

## AUTHOR DECLARATIONS

### Conflict of Interest

The authors have no conflicts to disclose.

### Author Contributions

**Philipp Riederer:** Data curation (equal); Formal analysis (equal); Validation (equal); Visualization (equal); Writing – original draft (equal); Writing – review & editing (equal). **Félix Devaux:** Resources (lead). **Guillaume Schweicher:** Project administration (equal); Writing – review & editing (supporting). **Yves H. Geerts:** Conceptualization (equal); Project administration (equal); Supervision (equal); Writing – review & editing (supporting). **Roland Kersting:** Conceptualization (equal); Formal analysis (equal); Project administration (equal); Supervision (equal); Writing – original draft (equal); Writing – review & editing (equal).

### DATA AVAILABILITY

The data that support the findings of this study are available from the corresponding author upon reasonable request.

## REFERENCES

- 1S. Steudel, S. D. Vusser, S. D. Jonge, D. Janssen, S. Verlaak, J. Genoe, and P. Heremans, "Influence of the dielectric roughness on the performance of pentacene transistors," *Appl. Phys. Lett.* **85**, 4400 (2004).
- 2G. Lin, Q. Wang, L. Peng, M. Wang, H. Lu, G. Zhang, G. Lv, and L. Qiu, "Impact of the lateral length scales of dielectric roughness on pentacene organic field-effect transistors," *J. Phys. D: Appl. Phys.* **48**, 105103 (2015).
- 3M. Geiger, R. Acharya, E. Reutter, T. Ferschke, U. Zschieschang, J. Weis, J. Pflaum, H. Klauk, and R. T. Weitz, "Effect of the degree of the gate-dielectric surface roughness on the performance of bottom-gate organic thin-film transistors," *Adv. Mater. Interfaces* **7**, 1902145 (2020).
- 4J. Veres, S. D. Ogier, S. W. Leeming, D. C. Cupertino, and S. M. Khaffaf, "Low-k insulators as the choice of dielectrics in organic field effect transistors," *Adv. Funct. Mater.* **13**, 199 (2003).
- 5A. F. Stassen, R. W. I. de Boer, N. N. Iosad, and A. F. Morpurgo, "Influence of the gate dielectric on the mobility of rubrene single-crystal field-effect transistors," *Appl. Phys. Lett.* **85**, 3899 (2004).
- 6X. Sun, C. Di, and Y. Liu, "Engineering of the dielectric-semiconductor interface in organic field-effect transistors," *J. Mater. Chem.* **20**, 2599 (2010).
- 7Y. D. Park, J. A. Lim, H. S. Lee, and K. Cho, "Interface engineering in organic transistors," *Mater. Today* **10**, 46 (2007).
- 8P. Riederer and R. Kersting, "Terahertz electromodulation spectroscopy for characterizing electronic transport in organic semiconductor thin films," *J. Infrared Millim. THz Waves* **44**, 1–16 (2023).
- 9J.-I. Park, J. W. Chung, J.-Y. Kim, J. Lee, J. Y. Jung, B. Koo, B.-L. Lee, S. W. Lee, Y. W. Jin, and S. Y. Lee, "Dibenzothiopheno [6,5-b'6',5'-f]thieno [3,2-b]thiophene (dbttt): High-performance small-molecule organic semiconductor for field-effect transistors," *J. Am. Chem. Soc.* **137**, 12175 (2015).
- 10R. E. Glover and M. Tinkham, "Conductivity of superconducting films for photon energies between 0.3 and 40kt," *Phys. Rev.* **108**, 243 (1957).
- 11S. Funk, G. Acuna, M. Handloser, and R. Kersting, "Probing the momentum relaxation time of charge carriers in ultrathin layers with terahertz radiation," *Opt. Express* **17**, 17450 (2009).
- 12T. K. Rockson, S. Baek, H. Jang, S. Oh, G. Choi, H. H. Choi, and H. S. Le, "Macroscopic interfacial property as a determining parameter for reliable prediction of charge mobility in organic transistors," *J. Phys. Chem. C* **122**, 17695 (2018).
- 13M. Fischer, M. Dressel, B. Gompf, A. K. Tripathi, and J. Pflaum, "Infrared spectroscopy on the charge accumulation layer in rubrene single crystals," *Appl. Phys. Lett.* **89**, 182103 (2006).
- 14R. Uchida, H. Yada, M. Makino, Y. Matsui, K. Miwa, T. Uemura, J. Takeya, and H. Okamoto, "Charge modulation infrared spectroscopy of rubrene single-crystal field-effect transistors," *Appl. Phys. Lett.* **102**, 093301 (2013).
- 15N. V. Smith, "Classical generalization of the Drude formula for the optical conductivity," *Phys. Rev. B* **64**, 155106 (2001).
- 16H. Yada, H. Sekine, T. Miyamoto, T. Terashige, R. Uchida, T. Otaki, F. Maruie, N. Kida, T. Uemura, S. Watanabe, T. Okamoto, J. Takeya, and H. Okamoto, "Evaluating intrinsic mobility from transient terahertz conductivity spectra of microcrystal samples of organic molecular semiconductors," *Appl. Phys. Lett.* **115**, 143301 (2019).
- 17K. Lee, A. J. Heeger, and Y. Cao, "Reflectance of polyaniline protonated with camphor sulfonic acid: Disordered metal on the metal-insulator boundary," *Phys. Rev. B* **48**, 14884 (1993).
- 18Z. Q. Li, V. Podzorov, N. Sai, M. C. Martin, M. E. Gershenson, M. D. Ventra, and D. N. Basov, "Light quasiparticles dominate electronic transport in molecular crystal field-effect transistors," *Phys. Rev. Lett.* **99**, 016403 (2007).
- 19M. Yamashita, C. Otani, M. Shimizu, and H. Okuzaki, "Effect of solvent on carrier transport in poly(3,4-ethylenedioxythiophene)/poly(4-styrenesulfonate) studied by terahertz and infrared-ultraviolet spectroscopy," *Appl. Phys. Lett.* **99**, 143307 (2011).
- 20S. Fratini, S. Ciuchi, and D. Mayou, "Phenomenological model for charge dynamics and optical response of disordered systems: Application to organic semiconductors," *Phys. Rev. B* **89**, 235201 (2014).
- 21H. Yada, R. Uchida, H. Sekine, T. Terashige, S. Tao, Y. Matsui, N. Kida, S. Fratini, S. Ciuchi, Y. Okada, T. Uemura, J. Takeya, and H. Okamoto, "Carrier dynamics of rubrene single-crystals revealed by transient broadband terahertz spectroscopy," *Appl. Phys. Lett.* **105**, 143302 (2014).

- <sup>22</sup>Y. Han, T. Miyamoto, T. Otaki, N. Takamura, N. Kida, N. Osakabe, J. Tsurumi, S. Watanabe, T. Okamoto, J. Takeya, and H. Okamoto, "Scattering mechanism of hole carriers in organic molecular semiconductors deduced from analyses of terahertz absorption spectra using Drude-Anderson model," *Appl. Phys. Lett.* **120**, 053302 (2022).
- <sup>23</sup>T. R. Arend, A. Wimmer, G. Schweicher, B. Chattopadhyay, Y. H. Geerts, and R. Kersting, "Band transport and trapping in didodecyl [1]benzothieno [3,2-b] [1]benzothiophene probed by terahertz spectroscopy," *J. Phys. Chem. Lett.* **8**, 5444 (2017).
- <sup>24</sup>M. Ohtomo, T. Suzuki, T. Shimada, and T. Hasegawa, "Band dispersion of quasi-single crystal thin film phase pentacene monolayer studied by angle-resolved photoelectron spectroscopy," *Appl. Phys. Lett.* **95**, 123308 (2009).
- <sup>25</sup>X. Wang, L. F. Register, and A. Dodabalapur, "Redefining the mobility edge in thin-film transistors," *Phys. Rev. Appl.* **11**, 064039 (2019).
- <sup>26</sup>S. Fratini and S. Ciuchi, "Bandlike motion and mobility saturation in organic molecular semiconductors," *Phys. Rev. Lett.* **103**, 266601 (2009).
- <sup>27</sup>N. F. Mott and E. A. Davis, *Electronic Processes in Non-Crystalline Materials* (Clarendon Press, 1979).
- <sup>28</sup>N. F. Mott and M. Kaveh, "Metal-insulator transitions in non-crystalline systems," *Adv. Phys.* **34**, 329 (1985).
- <sup>29</sup>P. Riederer, M. Bouraoui, and R. Kersting, "Impact of surface roughness on conduction in molecular semiconductors," *Appl. Phys. Lett.* **120**, 112103 (2022).
- <sup>30</sup>E.-K. Lee, M. Y. Lee, A. Choi, J.-Y. Kim, O. Y. Kweon, J.-H. Kim, J. Y. Jung, T.-J. Shin, J. H. Oh, J.-I. Park, and S. Y. Lee, "Phenyl derivative of dibenzothiopheno [6,5-b:6',5'-f]-thieno [3,2-b]thiophene (DPh-DBTTT): High thermally durable organic semiconductor for high-performance organic field-effect transistors," *Adv. Electron. Mater.* **3**, 1700142 (2017).
- <sup>31</sup>V. Podzorov, E. Menard, A. Borisov, V. Kiryukhin, J. A. Rogers, and M. E. Gershenson, "Intrinsic charge transport on the surface of organic semiconductors," *Phys. Rev. Lett.* **93**, 86602 (2004).
- <sup>32</sup>C. Goldmann, C. Krellner, K. P. Pernstich, S. Haas, D. J. Gundlach, and B. Batlogg, "Determination of the interface trap density of rubrene single-crystal field-effect transistors and comparison to the bulk trap density," *J. Appl. Phys.* **99**, 034507 (2006).
- <sup>33</sup>T. Yokota, T. Kajitani, R. Shidachi, T. Tokuhara, M. Kaltenbrunner, Y. Shoji, F. Ishiwari, T. Sekitani, T. Fukushima, and T. Someya, "A few-layer molecular film on polymer substrates to enhance the performance of organic devices," *Nat. Nanotechnol.* **13**, 139 (2018).
- <sup>34</sup>M. Sugiyama, S. Jancke, T. Uemura, M. Kondo, Y. Inoue, N. Namba, T. Araki, T. Fukushima, and T. Sekitani, "Mobility enhancement of DNNT and BTBT derivative organic thin-film transistors by triptycene molecule modification," *Org. Electron.* **96**, 106219 (2021).
- <sup>35</sup>R. Acharya, B. Peng, P. K. L. Chan, G. Schmitz, and H. Klauk, "Achieving ultralow turn-on voltages in organic thin-film transistors: Investigating fluoroalkylphosphonic acid self-assembled monolayer hybrid dielectrics," *Appl. Mater. Interfaces* **11**, 27104 (2019).
- <sup>36</sup>M. Geiger, L. Schwarz, U. Zschieschang, D. Manske, J. Pflaum, J. Weis, H. Klauk, and R. T. Weitz, "Quantitative analysis of the density of trap states in semiconductors by electrical transport measurements on low-voltage field-effect transistors," *Phys. Rev. Appl.* **10**, 044023 (2018).
- <sup>37</sup>X. Qian, T. Wang, and D. Yan, "High mobility organic thin-film transistors based on p-p heterojunction buffer layer," *Appl. Phys. Lett.* **103**, 173512 (2013).
- <sup>38</sup>O. D. Jurchescu, M. Popinciuc, B. J. van Wees, and T. T. M. Palstra, "Interface-controlled, high-mobility organic transistors," *Adv. Mater.* **19**, 688 (2007).
- <sup>39</sup>A. Choi, Y.-N. Kwon, J. W. Chung, Y. Yun, J.-I. Park, and Y. U. Lee, "Control of dielectric surface energy by dry surface treatment for high performance organic thin film transistor based on dibenzothiopheno [6,5-b:6',5'-f] thieno [3,2-b] thiophene semiconductor," *AIP Adv.* **10**, 025127 (2020).

## Supplementary Materials

### Molecular semiconductors and the Ioffe-Regel criterion: A terahertz study on band transport in DBTTT

P. Riederer,<sup>1</sup> F. Devaux,<sup>2</sup> G. Schweicher,<sup>2</sup> Y. H. Geerts,<sup>2</sup> and R. Kersting<sup>1, a)</sup>

<sup>1)</sup>*Photonics and Optoelectronics Group, Faculty of Physics and Center for NanoScience (CeNS), Ludwig-Maximilians-Universität, Königinstr. 10, 80539 München, Germany*

<sup>2)</sup>*Laboratoire de chimie des polymères, Faculté des Sciences, Université Libre de Bruxelles, ULB Boulevard du Triomphe, Brussels 1050, Belgium*

(Dated: 29 June 2023)

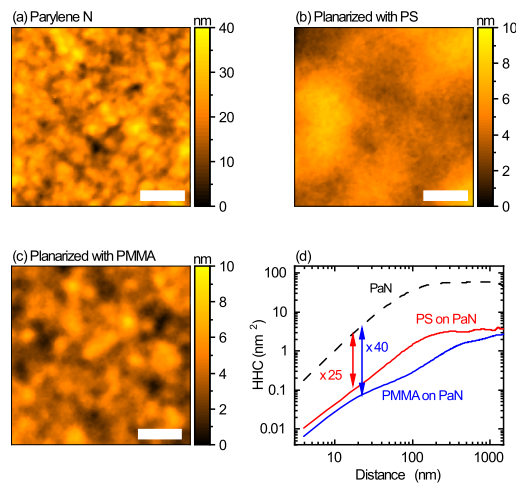
---

<sup>a)</sup>Electronic mail: roland.kersting@lmu.de

## I. THIN-FILM TOPOGRAPHY

Thin films of dibenzothiopheno[6,5-b:6',5'-f]thieno[3,2-b]thiophene (DBTTT) are fabricated by physical vapor deposition on parylene N (PaN), and PaN planarized either with polystyrene (PS) or with poly(methyl methacrylate) (PMMA). The PaN layers have a thickness of approximately 250 nm. Both of the planarization layers have thicknesses of approximately 50 nm.

The surface topographies of these insulators, as well as the surfaces of the DBTTT thin films, are investigated by atomic force microscopy (AFM). The lateral resolution of the AFM is approximately 25 nm. Figure S1 shows results of the AFM characterization of the insulators. The thin films of PaN have an RMS roughness of about 5 nm. Planarization of the PaN film with PS, as well as with PMMA, reduces the RMS roughness to approximately 1.2 nm.



S1. Atomic force micrographs of PaN (a), PaN planarized with PS (b), and PaN planarized with PMMA (c). The scale bar corresponds to 500 nm. Height-height correlations (d).

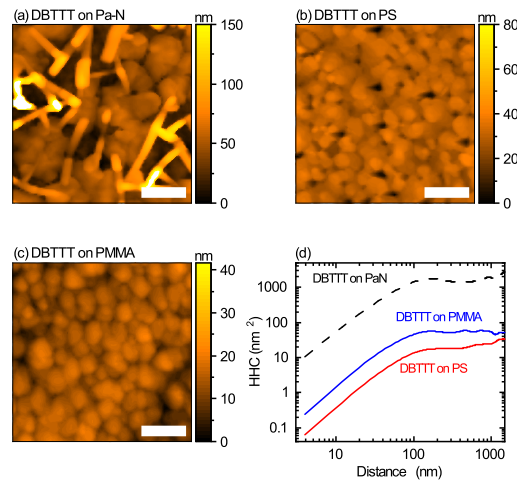
Height-height correlations in x-direction are deduced according to:

$$H_x(x) = \frac{1}{N(M-m)} \sum_{j=1}^N \sum_{i=1}^{M-m} (z_{i+m,j} - z_{i,j})^2 \quad (\text{S2})$$

where  $z_{i,j}$  describes the height at pixel  $p = (i, j)$ , the distance between points in x-direction is  $x = m\Delta x$ , and  $\Delta x$  is the sampling interval. The number of lines and columns of the AFM image are  $N$  and  $M$ , respectively. Often, surface roughness is described by the root mean square (RMS) value. The advantage of the height-height correlation function is that it provides an estimate how much

the height changes with distance. The height-height correlations in Fig. S1 show that planarization leads to a significant reduction of the surface roughness, even on distances comparable to the resolution of the AFM.

Figure S3 shows the impact of the insulator's surface roughness on the growth of DBTTT by physical vapor deposition. All DBTTT films have a nominal thickness of 50 nm. On the relatively rough surface of PaN, DBTTT forms flat crystallites, as well as vertical platelets. In contrast, the deposition on the planarized insulators exclusively leads to DBTTT crystallites oriented parallel to the insulator surface. The inferior quality of DBTTT deposited directly on parylene N is mirrored by the height-height correlations shown in Fig. S3 (d). Such films do not lead to reproducible terahertz (THz) transmission data and we refrain from the discussion of these structures.



S3. Atomic force micrographs of DBTTT deposited on different insulating materials: DBTTT on PaN (a) and on planarization layers of PS (b) and PMMA (c). The scale bar corresponds to a length of 500 nm. The corresponding height-height correlations (d).

## II. DATA ANALYSIS IN THE FREQUENCY DOMAIN

The procedure of data analysis in frequency domain is described in detail in Ref. 1. All layers of the device affect the transmission of THz radiation. For the relative differential transmission  $\Delta S/S$ , however, it suffices to consider a three-layer system. It comprises the insulator (layer 1), the semiconductor's accumulation layer (layer 2), and the remainder of the semiconductor layer

(layer 3), which does not contain charge carriers. The wavevectors in these layers are denoted by  $k_1$ ,  $k_2$ , and  $k_3$ . Only the sheet that describes the accumulation region is modulated by injection of charge carriers.

In all layers, the wave vectors of the THz radiation are given by

$$k = \sqrt{\omega^2 \epsilon_b \epsilon_0 \mu_0 + i \omega \mu_0 \sigma} \quad (\text{S4})$$

where  $\omega$  is the angular frequency,  $\epsilon_b$  is the relative background permittivity of the material, and  $\epsilon_0$  and  $\mu_0$  are the electric and magnetic field constants, respectively. Only the accumulation layer can have a non-zero conductivity  $\sigma$ . The transmission of such a three-layer system is<sup>1</sup>

$$t = \frac{4k_1 k_2 e^{ik_2 d_2}}{(k_1 + k_2)(k_2 + k_3) + (k_1 - k_2)(k_2 - k_3) e^{2ik_2 d_2}} \quad (\text{S5})$$

where  $d_2$  is the thickness of the accumulation layer.

The relative differential transmission results from switching the conductivity  $\sigma$  of layer 2 by electrical modulation.  $t_a$  and  $t_b$  are the transmissions recorded without and with injected carriers, respectively. This leads to the relative differential transmission

$$\frac{\Delta S}{S} = \frac{t_b - t_a}{t_a} \quad (\text{S6})$$

which depends on the sheet conductivity  $\sigma_{2D}(\omega)$  of the accumulation layer, for which a Drude response is assumed.

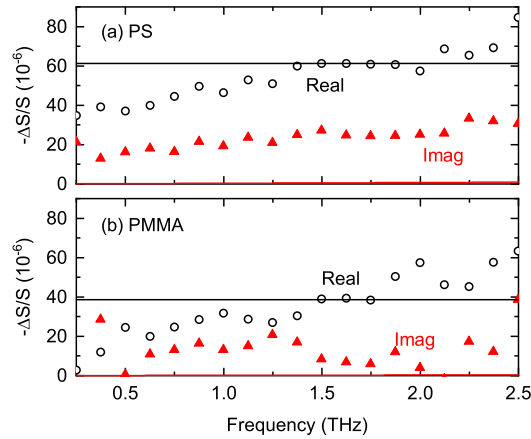
$$\sigma_{2D}(\omega) = \frac{n_{2D, \text{mob}} e^2 \tau}{m_h^*} \cdot \frac{1 + i \omega \tau}{1 + \omega^2 \tau^2} \quad (\text{S7})$$

Here,  $n_{2D}$  is the two-dimensional charge carrier density,  $e$  the elementary charge,  $\tau$  the Drude scattering time and  $m_h^*$  is the effective mass of the holes. The applicability of other models is discussed below in Section III.

The experimental transmission data are analyzed in the frequency domain (Fig. 4 of the manuscript and Fig. S8 of Supplementary Materials). Following Eq. (S7), the analysis considers two independent fit parameters: the sheet density of mobile carriers  $n_{2D, \text{mob}}$  and the Drude scattering time  $\tau$ . For the holes, an effective mass  $m_h^* = m_e$  is assumed. The density of injected holes  $n_{2D, \text{inj}}$  is calculated from the devices' capacitances and the applied gate voltage  $V_g$ .

Figure S8 shows the experimental data and fits for  $n_{2D, \text{mob}} = n_{2D, \text{inj}}$ . The fits roughly reproduce the real parts of the experimental data obtained on PS structures, as well as those measured on PMMA structures. The imaginary parts of the calculated data, however, are close to zero. Satisfactory fits cannot be achieved for  $n_{2D, \text{mob}} = n_{2D, \text{inj}}$  and the assumption that all injected charge

carriers are mobile has to be discarded. Much better fits to the experimental data are possible when assuming that only a fraction of the charge carriers participates in high mobility transport. The results for  $n_{2D,mob} = 0.05 \cdot n_{2D,inj}$  are shown in Fig. 4 of the manuscript. It should be emphasized that with the Drude model, both real and imaginary part of  $-\Delta S/S$  are positive.

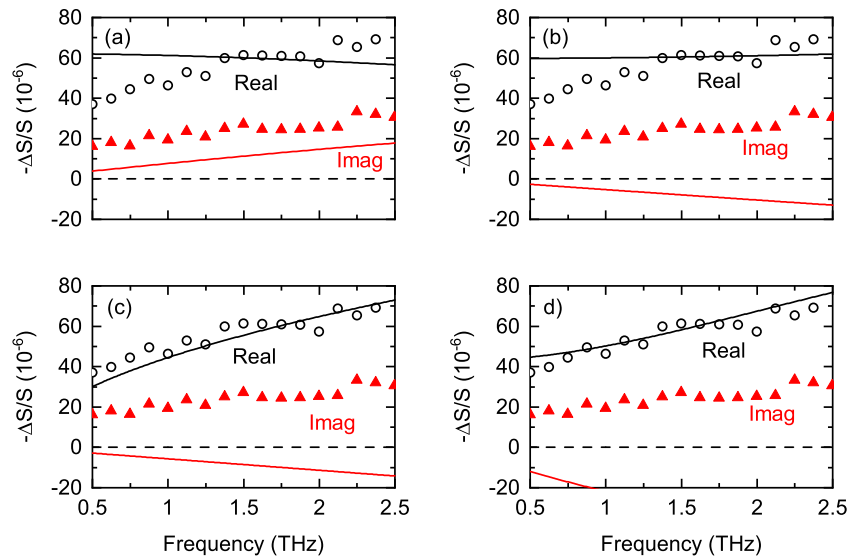


S8. Frequency dependence of the relative differential transmission  $\Delta S/S$  for DBTTT on PS (a) and for DBTTT on PMMA (b) at  $T = 300$  K. The real and imaginary parts of  $\Delta S/S$  are shown by black circles and by red triangles, respectively. Fits to the experimental data are shown by black lines and by red lines for the real and imaginary parts, respectively.

### III. ALTERNATIVE RESPONSE MODELS

Several charge transport models were applied for interpreting the THz response of charge carriers in organic semiconductors, such as the Drude model,<sup>2,3</sup> the Drude-Smith model,<sup>4,5</sup> the localization-modified Drude model,<sup>6,7</sup> and the Drude-Anderson model.<sup>8,9</sup> A brief discussion of the applicability of the models is given in the Sections III A to III C.

Figure S9 shows fits of these models to the experimental data. Only with the Drude model a reasonable fit to the real and to the imaginary part of the experimental data can be achieved. All other models show a reasonable reproduction of the real part of the signal  $-\Delta S/S$ , but fail with reproducing the imaginary part. While the imaginary part of the experimental data is positive, these models yield negative values. Thus, these models are discarded for explaining the experimental results. The experimental data can be discussed best within the framework of the classical Drude model.



S9. Experimental data obtained on DBTTT and fits according to the Drude with reduced carrier density  $n_{mob} < n_{inj}$  (a), the Drude-Smith model (b), the localization modified Drude model (c), and the Drude-Anderson model (d). Symbols depict the experimental data. The real and imaginary parts of the model calculations are shown by the solid black and red lines, respectively.

### A. Drude-Smith model

A generalization of the Drude response for the optical conductivity has been presented by N. V. Smith.<sup>4</sup> The model considers a persistence of carrier velocity after scattering

$$\sigma(\omega) = \frac{ne^2\tau/m}{(1-i\omega\tau)} \left[ 1 + \sum_{m=1}^{\infty} \frac{c_m}{(1-i\omega\tau)^m} \right]. \quad (\text{S10})$$

Usually, only  $c_1 = c$  is used, where  $c$  describes the fraction of momentum that is retained after scattering. Backscattering is described by  $c \in [-1, 0]$ .

The model is based on the assumption that carriers are not localized on dimensions comparable to the size  $a$  of a single unit cell. Only when the elastic mean free path significantly exceeds the unit cell  $\ell_{th} \gg a$ , the carriers can be described by Bloch waves and Drude theory can be applied.<sup>10,11</sup> As Fig. 4 of the manuscript shows, this is not the case in the present work.

One often raised argument that suggests the application of the Drude-Smith model is that efficient backscattering is expected at grain boundaries or dislocations within the crystals. However, the AFM data of Section I indicate grain diameters of about 150 nm. In contrast, the thermal mean free path  $\ell_{th}$  of the charge carriers is of the order of 1 nm. Thus, scattering at grain boundaries can be neglected, because most of the charge carriers do not reach a grain boundary within the Drude scattering time. Similarly, dislocations can affect momentum relaxation only if the elastic mean free path  $\ell_{th}$  exceeds the mean distance between dislocations. However, the observed mean free path barely exceeds the unit cell's size, which excludes scattering at dislocations.

Best fits by the Drude-Smith model were achieved with  $\tau = 4.7$  fs and  $c = -0.8$ . The real part of the signal  $-\Delta S/S$  can be reproduced, but the models lead to negative values of the imaginary part of  $-\Delta S/S$ . Thus, the model should not be considered for the interpretation of the presented data.

### B. Localization modified Drude model

In their seminal work, Mott and Kaveh describe the first order correction of transport by the real part of the conductivity<sup>11</sup>

$$\sigma = \sigma_{Boltzmann} \left\{ 1 - \frac{C}{(k_F \ell_{th})^2} \left( 1 - \frac{\ell_{th}}{L} \right) \right\} \quad (\text{S11})$$

where  $\ell_{th}$  is the elastic mean free path and  $L$  is the inelastic mean free path. Yamashita et al. presented for the real and the imaginary part of the localization modified Drude (LMD) response<sup>7</sup>

$$\sigma_{1,LMD} = \frac{\epsilon_0 \omega_p^2 \Gamma}{\omega^2 + \Gamma^2} \left[ 1 - \frac{C}{(k_F v_F)^2} \Gamma^2 + \frac{C}{(k_F v_F)^2} \Gamma^{1.5} (3\omega)^{0.5} \right] \quad (S12)$$

$$\sigma_{2,LMD} = \frac{\epsilon_0 \omega_p^2 \omega}{\omega^2 + \Gamma^2} \left[ -1 + (1 - \sqrt{6}) \frac{C}{(k_F v_F)^2} \Gamma^2 + \frac{C}{(k_F v_F)^2} \Gamma^{2.5} (3/\omega)^{0.5} \right] \quad (S13)$$

which are Kramers-Kronig consistent.

First of all, it is important to note that the above corrections result from a perturbative treatment.<sup>11</sup> Thus, the first order correction should be small, for instance  $C/(k_F \ell_{th})^2 < 1$  in Eq. (S11). Second, the above equations describe diffusive transport in metals<sup>11</sup> at the Fermi edge given by wavevector  $k_F$  and elastic mean free path  $\ell_{th} = v_F \tau$  as described in Ref. 6. The adaptation of the above equations to semiconductors requires to describe diffusion at the semiconductor's band edge. Using the Einstein-Smoluchowski relation leads to

$$\sigma_{3D} = \sigma_{Boltzmann} \left\{ 1 - \frac{\hbar^2}{(3\tau k_B T)^2} \left( 1 - \frac{\ell_{th}}{L} \right) \right\} \quad (S14)$$

for the real part of the conductivity of a three-dimensional carrier gas and in case of a two-dimensional carrier gas to

$$\sigma_{2D}(\omega) = \sigma_{Boltzmann} \left\{ 1 - \frac{\hbar}{\pi \tau k_B T} \ln \left( \frac{L}{\ell_{th}} \right) \right\} \quad (S15)$$

where  $\ell_{th}$  is the thermal mean free path.

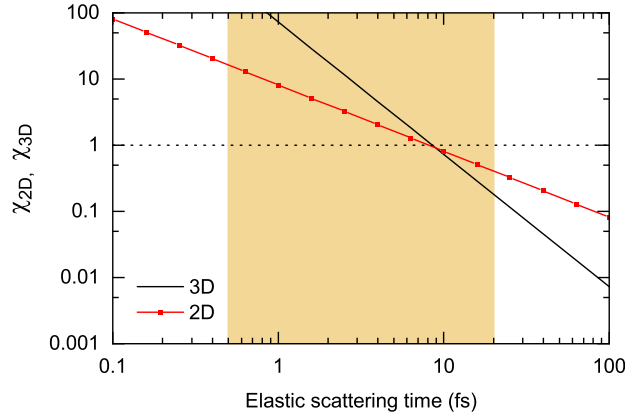
Before applying the above equations to organic semiconductors, it is worth to have a closer look at the first order corrections to the conductivity, for instance, for the three-dimensional case. Lee et al.<sup>6</sup> suggest that  $L$  is the distance, which a charge carrier diffuses during a single oscillation of the light field

$$L = \sqrt{\frac{D}{\omega}} = \sqrt{\frac{\mu k_B T}{e \omega}} \quad (S16)$$

where  $D$  is the diffusion constant and  $\omega$  is the angular frequency of the THz pulse. For a mobility of  $\mu = 3 \text{ cm}^2/\text{Vs}$  and  $\nu = \omega/2\pi = 1 \text{ THz}$  a value of  $L \approx 1.1 \text{ nm}$  is obtained, which of course exceeds the thermal mean free path  $\ell_{th} = \mu/e \cdot \sqrt{2k_B T m^*} \approx 0.2 \text{ nm}$ . Thus,  $\left( 1 - \frac{\ell_{th}}{L} \right) \approx 1$  and the correction to the conductivity is mainly given by  $\chi_{3D} = \hbar^2 / (3\tau k_B T)^2$ . Organic semiconductors that exhibit band transport have mobilities between  $1 \text{ cm}^2/\text{Vs}$  and  $30 \text{ cm}^2/\text{Vs}$ , which corresponds to scattering times between approximately  $0.5 \text{ fs}$  and  $15 \text{ fs}$  when assuming an effective mass of  $m_e$ . Figure S17 shows the dependence of the corrections  $\chi_{2D}$  and  $\chi_{3D}$  on the elastic scattering

time  $\tau$  for a temperature of  $T = 300$  K. The range of scattering times that are typical for molecular semiconductors is illustrated by the shaded area. For most of this range,  $\chi > 1$ . This is not consistent with the proposition of a first order correction obtained by perturbation theory. Thus, the model should not be applied in this range. Only for scattering times that exceed approximately 10 fs reasonable corrections with  $\chi < 1$  appear. This, however, corresponds to mobilities of  $\mu \geq 15 \text{ cm}^2/\text{Vs}$ , which significantly exceeds the mobility of  $\mu \approx 3.0 \text{ cm}^2/\text{Vs}$  observed on samples of DBTTT on PS. A further argument that speaks against the interpretation of our data with the localization-modified Drude response is that this model leads to a negative imaginary part of the signal as pointed out above (see Fig. S9).

The best fit to the data (Fig. S9) gives  $\tau = 3.1$  fs and  $\chi_{3D} = 7.5$ . The latter value shows that the result can no longer be seen as a first order perturbation and the model is not considered for interpreting the experimental data.



S17. Corrections of the localization modified Drude model in dependence on the elastic scattering time  $\tau$  for  $T = 300$  K. The shaded area corresponds to scattering times that are typical for band transport in molecular semiconductors.

### C. Drude-Anderson model

The Drude-Anderson model, as described by Fratini et al.<sup>8,12</sup> considers a Drude relaxation time  $\tau$ , a backscattering time  $\tau_b$  and an inelastic time  $\tau_{in}$  with  $\tau < \tau_b < \tau_{in}$ . The real part of the optical

conductivity is:

$$\sigma_1(\omega) = \frac{ne^2L^2}{\tau_b - \tau} \cdot \frac{\tanh\left(\frac{\hbar\omega}{2k_B T}\right)}{\hbar\omega} \cdot \text{Re} \left[ \frac{1}{1 + \tau/\tau_{in} - i\omega\tau} - \frac{1}{1 + \tau_b/\tau_{in} - i\omega\tau_b} \right] \quad (\text{S18})$$

where  $L^2$  is defined as:

$$L^2 = \frac{2k_B T}{m_h^*} \cdot \tau \cdot (\tau_b - \tau). \quad (\text{S19})$$

The imaginary part can be deduced by Kramers-Kronig relations.

Again, use of a Drude scattering time  $\tau$  requires the applicability of the Bloch model and thus  $\ell_{th} \gg a$  according to the Ioffe-Regel criterion. This is consistent with previous work of Fratini et al.<sup>13</sup>, wherein the authors suggest that charge carriers localize on the scale of several unit cells  $a$  due to molecular vibrations. In the present work, however, the elastic mean free path is smaller than the size of the unit cell  $a$  when considering that all carriers contribute to transport and barely exceeds  $a$  when assuming that only a fraction of 5% participates in transport (see Fig. 4 of the manuscript). This speaks against the application of the Drude-Anderson model in the present work. Additionally, this model leads to a negative imaginary part of  $-\Delta S/S$  (Fig. S17 (d)), which clearly differs from the experimental data. Thus, the Drude-Anderson model should not be used for interpreting the data of the present work. The shown fit uses  $\tau = 2.5$  fs,  $\tau_b = 60$  fs, and  $\tau_{in} = 150$  fs for the real part of the conductivity. The imaginary part of the conductivity is deduced by Kramers-Kronig relations.

## REFERENCES

- <sup>1</sup>P. Riederer and R. Kersting, "Terahertz electromodulation spectroscopy for characterizing electronic transport in organic semiconductor thin films," *J. Infrared Milli. Terahertz Waves* (2022), <https://doi.org/10.1007/s10762-022-00893-z>
- <sup>2</sup>M. Fischer, M. Dressel, B. Gompf, A. K. Tripathi, and J. Pflaum, "Infrared spectroscopy on the charge accumulation layer in rubrene single crystals," *Appl. Phys. Lett.* **89**, 182103 (2006)
- <sup>3</sup>R. Uchida, H. Yada, M. Makino, Y. Matsui, K. Miwa, T. Uemura, J. Takeya, and H. Okamoto, "Charge modulation infrared spectroscopy of rubrene single-crystal field-effect transistors," *Appl. Phys. Lett.* **102**, 093301 (2013)
- <sup>4</sup>N. V. Smith, "Classical generalization of the Drude formula for the optical conductivity," *Phys. Rev. B* **64**, 155106 (2001)

- <sup>5</sup>H. Yada, H. Sekine, T. Miyamoto, T. Terashige, R. Uchida, T. Otaki, F. Maruike, N. Kida, T. Uemura, S. Watanabe, T. Okamoto, J. Takeya, and H. Okamoto, "Evaluating intrinsic mobility from transient terahertz conductivity spectra of microcrystal samples of organic molecular semiconductors," *Appl. Phys. Lett.* **115**, 143301 (2019)
- <sup>6</sup>K. Lee, A. J. Heeger, and Y. Cao, "Reflectance of polyaniline protonated with camphor sulfonic acid: Disordered metal on the metal-insulator boundary," *Phys. Rev. B* **48**, 14884 (1993)
- <sup>7</sup>M. Yamashita, C. Otani, M. Shimizu, and H. Okuzaki, "Effect of solvent on carrier transport in poly(3,4-ethylenedioxythiophene)/poly(4-styrenesulfonate) studied by terahertz and infrared-ultraviolet spectroscopy," *Appl. Phys. Lett.* **99**, 143307 (2011)
- <sup>8</sup>S. Fratini, S. Ciuchi, and D. Mayou, "Phenomenological model for charge dynamics and optical response of disordered systems: Application to organic semiconductors," *Phys. Rev. B* **89**, 235201 (2014)
- <sup>9</sup>Y. Han, T. Miyamoto, T. Otaki, N. Takamura, N. Kida, N. Osakabe, J. Tsurumi, S. Watanabe, T. Okamoto, J. Takeya, and H. Okamoto, "Scattering mechanism of hole carriers in organic molecular semiconductors deduced from analyses of terahertz absorption spectra using Drude-Anderson model," *Appl. Phys. Lett.* **120**, 053302 (2022)
- <sup>10</sup>N. F. Mott and E. A. Davis, *Electronic processes in non-crystalline materials* (Clarendon Press, 1979)
- <sup>11</sup>N. F. Mott and M. Kaveh, "Metal-insulator transitions in non-crystalline systems," *Adv. Phys.* **34**, 329 (1985)
- <sup>12</sup>S. Fratini, D. Mayou, and S. Ciuchi, "The transient localization scenario for charge transport in crystalline organic materials," *Adv. Funct. Mater.* **26**, 2292–2315 (2016)
- <sup>13</sup>S. Fratini and S. Ciuchi, "Bandlike motion and mobility saturation in organic molecular semiconductors," *Phys. Rev. Lett.* **103**, 266601 (2009)

## 5 Summary and Outlook

The aim of this work was to investigate charge transport limiting phenomena in molecular semiconductor thin-films using THz electromodulation spectroscopy.

Although THz spectroscopy is a widely used tool for the investigation of organic semiconductor devices, it exhibits some severe drawbacks. On the one hand, THz spectroscopy is unable to discriminate between differently charged carriers generated upon optical excitation. On the other hand, carrier transport within the organic semiconductor bulk is probed which inherits fundamentally different physics than within an accumulation channel, as it is the case for field-effect devices. Furthermore, a precise knowledge about the charge carrier density generated by optical excitation is difficult. THz electromodulation spectroscopy circumvents these problems and has already been used to study charge transport within crystalline semiconductors. In this work, it was shown that THz electromodulation spectroscopy is a capable tool for the investigation of organic semiconductors. A thorough explanation of the THz electromodulation spectroscopy technique was given, including the requirements for the experimental setup and the investigated devices. Furthermore, the detection limit of about  $1 \text{ cm}^2/\text{Vs}$  has been identified, which shows the applicability of THz electromodulation spectroscopy to most of today's relevant organic semiconductors.

It is well known that the insulator-semiconductor interface has a major influence on the charge transport properties. Nevertheless, the roughness of the gate dielectric cannot be decoupled from the resulting crystal structure. Thus, self-consistent calculations have been performed to evaluate the influence of the insulator surface roughness on the charge distribution within the field-effect device. This has been achieved by merging two-dimensional AFM scans into a three-dimensional model with  $10^5$  nodes. Within this model, the Poisson equation was self-consistently solved by using a sparse matrix formulation and combining the Newton method with the successive over-relaxation algorithm. It has been confirmed, that over 95 % of the charge carriers accumulate in the first two monolayers when an external potential is applied. Within surface puddles, the charge distribution varies strongly as screening of the wells' potentials plays an important role. Surface roughness in the range of one monolayer already leads to a reduction in conductivity of approximately 50 %. Moreover, it was found that charge carriers rarely undergo thermally activated hopping, since two-dimensional percolation pathways arise. Thus, it was shown, that the surface roughness of the insulator has a crucial impact on the charge transport in field-effect devices.

A very undesirable feature of organic field-effect devices is the lack of long-term performance stability, often referred to as bias-stress effect. In this work, THz electromodulation spectroscopy has been used to investigate the influence of gold containing contact layers on the

degradation of organic semiconductor thin-films. It was found that during the application of a bias voltage, the relative differential signal decreases. This effect and its partial reversibility could be attributed to the migration of gold ions into the molecular semiconductor. These dynamics were observed to be thermally activated with an activation energy in the range of the deformation energy of the organic crystal lattice. It was shown that this degradation phenomenon disappears when the gold is replaced by molybdenum oxide. Without these findings, time-consuming frequency-resolved THz electromodulation spectroscopy measurements would not be possible.

Finally, frequency-resolved and temperature-dependent THz electromodulation spectroscopy measurements on dibenzothiopheno[6,5-b:6',5'-f]thieno[3,2-b]thiophene (DBTTT) thin films have been conducted. It was found that not all injected charge carriers contribute to band transport. Otherwise, the thermal mean-free path would be smaller than the semiconductor's unit cell, which contradicts the Ioffe-Regel criterion. The  $T^{1/2}$  temperature dependence of the mobility suggests that intrinsic disorder is the main limiting factor in these DBTTT devices.

Altogether, this work shows on the one hand the power of the THz electromodulation technique and on the other hand that there is still a lot of research potential to tackle open questions in the field of organic semiconductors. Furthermore, the results of this thesis highlight that the mobility value is not an ideal figure of merit to compare organic field-effect devices.

It would be interesting to use THz electromodulation spectroscopy to evaluate the theoretical construct of the transient localization scenario, which has become one of the main theoretical frameworks to explain charge transport in organic materials over the last decades. Temperature-dependent measurements in the frequency domain on different delicately fabricated samples (e.g. BTBT and C8-BTBT-C8) with atomically smooth insulators could help to understand the impact of dynamic disorder. In addition, increased attention could be given to the fabrication of inverse structures using the uppermost monolayers of the deposited semiconductor as an accumulation region. The phenomenon that the first few deposited layers inherit structural disorder, as has also been seen within this work, which has a detrimental effect on the charge transport could be circumvented. To further strengthen the power of THz electromodulation spectroscopy, the resulting local conductivity data could be compared with, for example, gated van-der-Pauw measurements. This comparison allows to extract information on the influence of grain-boundaries on the overall mobility.

We can see that there is still a lot of research potential in the field of organic electronics. The success story of organic materials can still be continued if the focus is shifted from the race for ever higher mobility values to the device, its interfaces and its physics: "the interface is the device".

---

# Appendix

## A.1 Mean Free Path of Atoms inside the PVD

The mean free path  $\Lambda$  can be calculated by using [130]:

$$\Lambda = \frac{1}{n \cdot \sigma} \quad (\text{A.1.1})$$

where  $n$  is the density of particles and  $\sigma$  the collision cross-section. To calculate the mean free path for a chromium atom traveling through the PVD at a pressure of  $p = 10^{-7}$  mbar =  $10^{-5}$  Pa at room temperature  $T = 25^\circ\text{C}$ , the ideal gas equation is needed:

$$p \cdot V = N \cdot k_B \cdot T \quad (\text{A.1.2})$$

with the volume  $V$ , the Boltzmann constant  $k_B$  and  $N$  the number of particles. Then, the particle density  $n$  is determined by:

$$n = \frac{N}{V} = \frac{p}{k_B \cdot T}. \quad (\text{A.1.3})$$

For the given pressure and temperature one gets  $n = 2.44 \times 10^{15} \text{ m}^{-3}$ . The collision cross section  $\sigma$  is calculated via:

$$\sigma = \pi \cdot (r_1 + r_2)^2 \quad (\text{A.1.4})$$

with  $r_1$  and  $r_2$  being the radii of the circular atoms colliding. For the case of only one type of atom  $r_1 = r_2 = r$ . In the case of chromium the atomic radius is  $r_{Cr} = 0.14 \text{ nm}$  [131]. Therefore, a collision cross-section of  $\sigma_{Cr} = 2.46 \times 10^{-19} \text{ m}^2$  is determined. With the given pressure and temperature, the mean free path is  $\Lambda_{Cr} = 1.67 \times 10^3 \text{ m}$ .

## A.2 Bragg Condition and the Thickness of Parylene-N

The paN film thickness during deposition is monitored via the observation of interference color changes.

This phenomenon can be described by constructive interference of light at a plane parallel plate of thickness  $d$  with refractive index  $n$ . The basic principle is depicted in Figure A1.

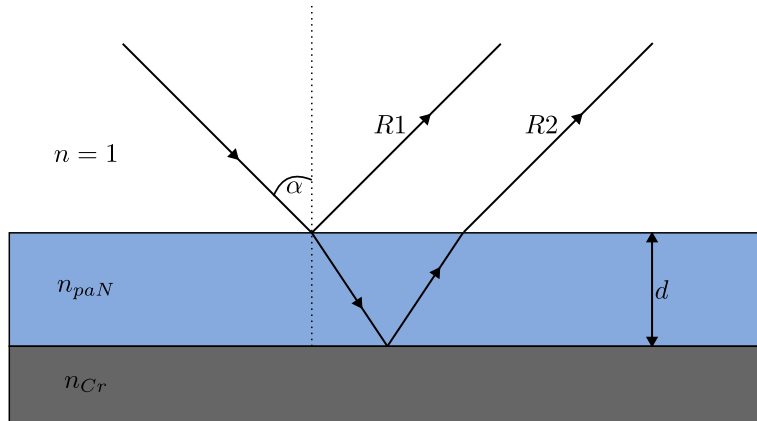


**Fig. A1** Schematic principle for the calculation of the path difference of the first reflected wave  $R1$  and the second reflected wave  $R2$  used for thickness determination during paN deposition.

A fraction of the incident light with wavelength  $\lambda$  is reflected ( $R1$ ) while the rest is refracted. At the second interface, the refracted part is once more reflected and exits the plate parallel ( $R2$ ) to the first reflection. If the path difference between  $R1$  and  $R2$  matches a multiple of the period of the wavelength, constructive interference occurs and can be described by the Bragg condition [109]:

$$2dn \cdot \sin(\alpha) = m \cdot \lambda, \quad m = 1, 2, 3, \dots \quad (\text{A.2.1})$$

where  $\alpha$  is the incident angle of the wave. It is important to note, that Equation A.2.1 only holds true for the case of hard reflection ( $n_2 > n$ ) at the second interface. Otherwise, the  $90^\circ$  phase-shift during reflection at the first interface is not canceled out. In the case of CVD of paN, the paN is usually deposited onto a Cr layer and thus  $n_{Cr} > n_{paN}$  and Equation A.2.1 holds true. [109]

Under the assumption of orthogonal incidence of light ( $\alpha = 0^\circ$ ), with help of the Bragg condition and the refractive index of paN ( $n_{paN} = 1.6$  [96]), colors can be attributed to thicknesses of the deposited layer. Well distinguishable interference colors and the corresponding thicknesses of the paN layer  $d_{paN}$  are given in Table A1.

order $m$	color	wavelength (nm)	$d_{paN}$ (nm)	mean $d_{paN}$ (nm)
1	purple	380-450	118-140	129
1	blue	450-495	140-154	147
1	green	495-570	154-178	166
1	yellow	575-585	180-182	181
1	orange	585-620	182-193	188
1	red	625-740	195-231	213
2	purple	380-450	238-281	260
2	blue	450-495	281-309	295
2	green	495-570	309-356	333
2	yellow	575-585	360-366	363
2	orange	585-620	366-388	377
2	red	625-740	391-462	427

**Table A1** Distinct distinguishable interference colors and corresponding paN thicknesses determined via the Bragg condition (Equ. A.2.1). Wavelengths to the corresponding colors are extracted from Ref. [132].

### A.3 Non-Ideal Thickness-Resistance Curve

An exemplary non-ideal thickness-resistance curve is shown in Figure A2. The resistance decreases slowly to a first saturation knee at approximately  $4000 \text{ k}\Omega$  within a thickness of  $8 \text{ nm}$ . Upon further deposition, the resistance drops a second time until it reaches the desired value of  $\approx 2 \text{ k}\Omega$  at a thickness of  $15 \text{ nm}$ . This double-decrease behavior is explained by a structural change of the molecular semiconductor layer during top contact deposition. The roughness of the MSC layer strongly increased due to excessive heat stress. Cooling the substrate holder to  $\approx 0^\circ$  and applying a start-stop deposition process allowed to maintain the structural properties of the MSC.

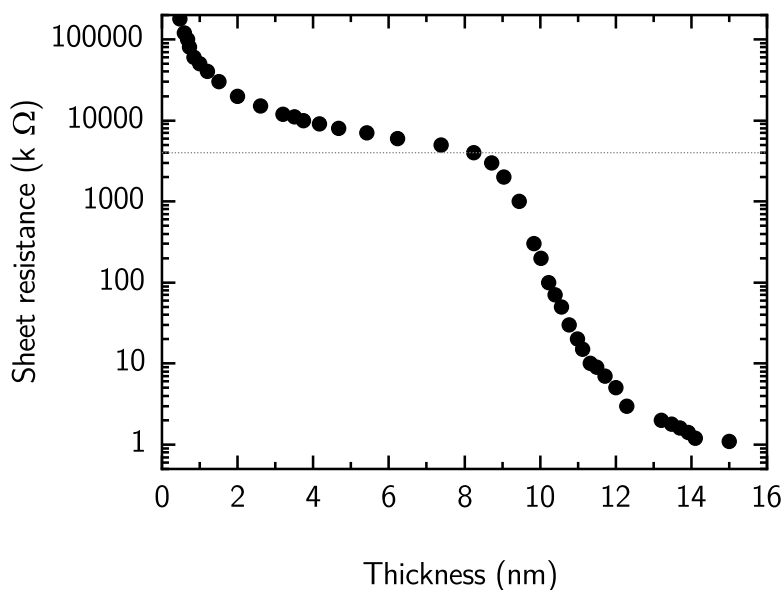


**Fig. A2** Exemplary data of a non-ideal curve of the measured sheet resistance over the deposited Cr thickness during top contact evaporation onto the organic semiconductor C8-BTBT-C8.

## A.4 AFM Edge Response Resolution

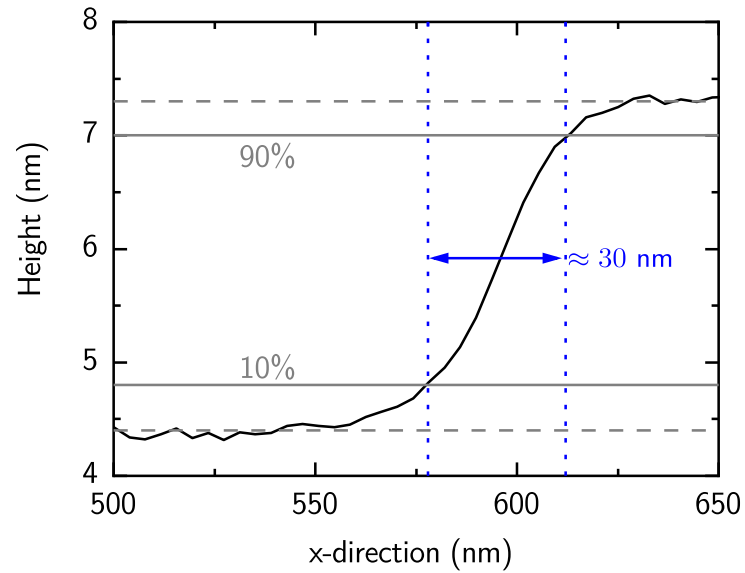


**Fig. A3** Edge response of exemplary AFM image. The distance it takes for the system to follow a sharp edge from 10% to 90% of its height is approximately 30 nm and thus the image resolution.



---

# Bibliography

- [1] H. Kroemer: Nobel Lecture: Quasielectric fields and band offsets: teaching electrons new tricks. *Rev. Mod. Phys.* **73**, 783 (2001).
- [2] C.K. Chiang, C.R. Fincher, Y.W. Park, A.J. Heeger, H. Shirakawa, E.J. Louis, S.C. Gau and A.G. MacDiarmid: Electrical Conductivity in Doped Polyacetylene. *Phys. Rev. Lett.* **39**, 1098 (1977).
- [3] H. Shirakawa, E.J. Louis, A.G. MacDiarmid, C.K. Chiang and A.J. Heeger: Synthesis of electrically conducting organic polymers: halogen derivatives of polyacetylene, (CH). *J. Chem. Soc., Chem. Commun.* **16**, 578 (1977).
- [4] C.K. Chiang, Y.W. Park, A.J. Heeger, H. Shirakawa, E.J. Louis and A.G. MacDiarmid: Conducting polymers: Halogen doped polyacetylene. *J. Chem. Phys.* **69**, 5098 (1978).
- [5] A. Tsumura, H. Koezuka and T. Ando: Macromolecular electronic device: Field-effect transistor with a polythiophene thin film. *Appl. Phys. Lett.* **49**, 1210 (1986).
- [6] S. Himmelberger and A. Salleo: Engineering semiconducting polymers for efficient charge transport. *MRS Commun.* **5**, 383 (2015).
- [7] H. Kobayashi, S. Kanbe, S. Seki, H. Kigchi, M. Kimura, I. Yudasaka, S. Miyashita, T. Shimoda, C.R. Towns, J.H. Burroughes and R.H. Friend: A novel RGB multicolor light-emitting polymer display. *Synth. Met.* **111-112**, 125 (2000).
- [8] B.K. Crone, A. Dodabalapur, R. Sarpeshkar, A. Gelperin, H.E. Katz and Z. Bao: Organic oscillator and adaptive amplifier circuits for chemical vapor sensing. *J. Appl. Phys.* **91**, 10140 (2002).
- [9] P.F. Baude, D.A. Ender, M.A. Haase, T.W. Kelley, D.V. Muyres and S.D. Theiss: Pentacene-based radio-frequency identification circuitry. *Appl. Phys. Lett.* **82**, 3964 (2003).
- [10] E.G. Bittle, J.I. Basham, T.N. Jackson, O.D. Jurchescu and D.J. Gundlach: Mobility overestimation due to gated contacts in organic field-effect transistors. *Nat. Commun.* **7**, 1 (2016).
- [11] H.H. Choi, K. Cho, C.D. Frisbie, H. Sirringhaus and V. Podzorov: Critical assessment of charge mobility extraction in FETs. *Nat. Mater.* **17**, 2 (2018).
- [12] S.G. Engelbrecht, A.J. Reichel and R. Kersting: Charge carrier relaxation and effective masses in silicon probed by terahertz spectroscopy. *J. Appl. Phys.* **112**, 123704 (2012).

- [13] S.G. Engelbrecht, T.R. Arend, T. Zhu, M.J. Kappers and R. Kersting: Terahertz electromodulation spectroscopy of electron transport in GaN. *Appl. Phys. Lett.* **106**, 092107 (2015).
- [14] S.G. Engelbrecht, M. Prinz, T.R. Arend and R. Kersting: Terahertz spectroscopy on hole transport in pentacene thin films. *Appl. Phys. Lett.* **105**, 012101 (2014).
- [15] T.R. Arend, A. Wimmer, G. Schweicher, B. Chattopadhyay, Y.H. Geerts and R. Kersting: Band Transport and Trapping in Didodecyl[1]benzothieno[3,2-b][1]benzothiophene Probed by Terahertz Spectroscopy. *J. Phys. Chem. Lett.* **8**, 5444 (2017).
- [16] X.C. Zhang and J. Xu: *Introduction to THz Wave Photonics*. Springer US (2010).
- [17] M.J.W. Rodwell, M. Urteaga, T. Mathew, D. Scott, D. Mensa, Q. Lee, J. Guthrie, Y. Betser, S.C. Martin, R.P. Smith, S. Jaganathan, S. Krishnan, S.I. Long, R. Pullela, B. Agarwal, U. Bhattacharya, L. Samoska and M. Dahlstrom: Submicron scaling of HBTs. *IEEE Trans. Electron Devices* **48**, 2606 (2001).
- [18] M. Beck, D. Hofstetter, T. Aellen, J. Faist, U. Oesterle, M. Ilegems, E. Gini and H. Melchior: Continuous wave operation of a mid-infrared semiconductor laser at room temperature. *Science* **295**, 301 (2002).
- [19] A. Dobroiu, C. Otani and K. Kawase: Terahertz-wave sources and imaging applications. *Meas. Sci. Technol.* **17**, R161 (2006).
- [20] L. Yu, L. Hao, T. Meiqiong, H. Jiaoqi, L. Wei, D. Jinying, C. Xueping, F. Weiling and Z. Yang: The medical application of terahertz technology in non-invasive detection of cells and tissues: opportunities and challenges. *RSC Adv.* **9**, 9354 (2019).
- [21] J.B. Baxter and G.W. Guglietta: Terahertz Spectroscopy. *Anal. Chem.* **83**, 4342 (2011).
- [22] L. Afsah-Hejri, E. Akbari, A. Toudeshki, T. Homayouni, A. Alizadeh and R. Ehsani: Terahertz spectroscopy and imaging: A review on agricultural applications. *Comput. Electron. Agric.* **177**, 105628 (2020).
- [23] J.F. Federici, B. Schulkin, F. Huang, D. Gary, R. Barat, F. Oliveira and D. Zimdars: THz imaging and sensing for security applications—explosives, weapons and drugs. *Semicond. Sci. Technol.* **20**, 266 (2005).
- [24] Y.S. Lee: *Principles of Terahertz Science and Technology*. Springer Science + Business Media (2009).

- [25] R. Ulbricht, E. Hendry, J. Shan, T.F. Heinz and M. Bonn: Carrier dynamics in semiconductors studied with time-resolved terahertz spectroscopy. *Rev. Mod. Phys.* **83**, 543 (2011).
- [26] F. Blanchard, L. Razzari, H.C. Bandulet, G. Sharma, R. Morandotti, J.C. Kieffer, T. Ozaki, M. Reid, H.F. Tiedje, H.K. Haugen and F.A. Hegmann: Generation of 1.5 microJ single-cycle terahertz pulses by optical rectification from a large aperture ZnTe crystal. *Opt. Express* **15**, 13212 (2007).
- [27] C. Evain, C. Sz waj, E. Roussel, J. Rodriguez, M. Le Parquier, M.A. Tordeux, F. Ribeiro, M. Labat, N. Hubert, J.B. Brubach, P. Roy and S. Bielawski: Stable coherent terahertz synchrotron radiation from controlled relativistic electron bunches. *Nat. Phys.* **15**, 635 (2019).
- [28] J.D. Bagley, C.D. Moss, S.A. Sorenson and J.A. Johnson: Laser-induced plasma generation of terahertz radiation using three incommensurate wavelengths. *J. Phys. B: At. Mol. Opt. Phys.* **51**, 144004 (2018).
- [29] M. Asada and S. Suzuki: Terahertz Emitter Using Resonant-Tunneling Diode and Applications. *Sensors* **21**, 1384 (2021).
- [30] R. Kersting, K. Unterrainer, G. Strasser, H.F. Kauffmann and E. Gornik: Few-Cycle THz Emission from Cold Plasma Oscillations. *Phys. Rev. Lett.* **79**, 3038 (1997).
- [31] A.J. Lee, D.J. Spence and H.M. Pask: Terahertz sources based on stimulated polariton scattering. *Prog. Quantum Electron.* **71**, 100254 (2020).
- [32] K.J. Tielrooij, A. Principi, D.S. Reig, A. Block, S. Varghese, S. Schreyeck, K. Brunner, G. Karczewski, I. Ilyakov, O. Ponomaryov, T.V.A.G. de Oliveira, M. Chen, J.C. Deinert, C.G. Carbonell, S.O. Valenzuela, L.W. Molenkamp, T. Kiessling, G.V. Astakhov and S. Kovalev: Milliwatt terahertz harmonic generation from topological insulator metamaterials. *Light Sci. Appl.* **11**, 1 (2022).
- [33] C. Weiss, R. Wallenstein and R. Beigang: Magnetic-field-enhanced generation of terahertz radiation in semiconductor surfaces. *Appl. Phys. Lett.* **77**, 4160 (2000).
- [34] L.L. Hale, H. Jung, S.D. Gennaro, J. Briscoe, C.T. Harris, T.S. Luk, S.J. Addamane, J.L. Reno, I. Brener and O. Mitrofanov: Terahertz Pulse Generation from GaAs Metasurfaces. *ACS Photonics* **9**, 1136 (2022).
- [35] E.Th. Papaioannou and R. Beigang: THz spintronic emitters: a review on achievements and future challenges. *Nanophotonics* **10**, 1243 (2021).
- [36] A. Dreyhaupt, S. Winnerl, T. Dekorsy and M. Helm: High-intensity terahertz radiation from a microstructured large-area photoconductor. *Appl. Phys. Lett.* **86**, 121114 (2005).

- [37] R.A. Lewis: A review of terahertz detectors. *J. Phys. D: Appl. Phys.* **52**, 433001 (2019).
- [38] J. Price and T. Goble: Signals and noise. In *Telecommunications Engineer's Reference Book*, edited by F. Mazda. Butterworth-Heinemann (1993).
- [39] D. Schroeder: *Astronomical Optics*. Academic Press (2000).
- [40] Q. Wu and X.C. Zhang: Free-space electro-optic sampling of terahertz beams. *Appl. Phys. Lett.* **67**, 3523 (1995).
- [41] F. Peter, S. Winnerl, S. Nitsche, A. Dreyhaupt, H. Schneider and M. Helm: Coherent terahertz detection with a large-area photoconductive antenna. *Appl. Phys. Lett.* **91**, 081109 (2007).
- [42] F. Simoons: THz Bolometer Detectors. In *Physics and Applications of Terahertz Radiation*, edited by M. Perenzoni and J. P. Douglas. Springer (2013).
- [43] P.S. Stefanova, J.M. Hammler, A.K. Klein, A.J. Gallant and C. Balocco: Polymer-based micro-golay cells for THz detection. In *2016 41st International Conference on Infrared, Millimeter, and Terahertz waves (IRMMW-THz)*. IEEE, Copenhagen, Denmark (2016).
- [44] J. Dai, X. Xie and X.C. Zhang: Detection of Broadband Terahertz Waves with a Laser-Induced Plasma in Gases. *Phys. Rev. Lett.* **97**, 103903 (2006).
- [45] Y.J. Lin and M. Jarrahi: Heterodyne terahertz detection through electronic and optoelectronic mixers. *Rep. Prog. Phys.* **83**, 066101 (2020).
- [46] M. Born and E. Wolf: *Principles of optics*. Pergamon Press (1975).
- [47] R.W. Boyd: *Nonlinear Optics*. Elsevier (2020).
- [48] P.C.M. Planken, H.K. Nienhuys, H.J. Bakker and T. Wenckebach: Measurement and calculation of the orientation dependence of terahertz pulse detection in ZnTe. *J. Opt. Soc. Am. B, JOSAB* **18**, 313 (2001).
- [49] J. Shinar: *Organic Light-Emitting Devices*. Springer (2004).
- [50] K. Myny, S. Steudel, P. Vicca, S. Smout, M.J. Beenhakkers, N.A.J.M. van Aerle, F. Furthner, B. van der Putten, A.K. Tripathi, G.H. Gelinck, J. Genoe, W. Dehaene and P. Heremans: Organic RFID Tags. In *Applications of Organic and Printed Electronics: A Technology-Enabled Revolution*, edited by E. Cantatore. Springer US (2013).
- [51] K. Liu, B. Ouyang, X. Guo, Y. Guo and Y. Liu: Advances in flexible organic field-effect transistors and their applications for flexible electronics. *npj Flexible Electron.* **6**, 1 (2022).

- [52] G.E. Stillman, C.M. Wolfe and J.O. Dimmock: Hall coefficient factor for polar mode scattering in n-type GaAs. *J. Phys. Chem. Solids* **31**, 1199 (1970).
- [53] M. Sotoodeh, A.H. Khalid and A.A. Rezazadeh: Empirical low-field mobility model for III–V compounds applicable in device simulation codes. *J. Appl. Phys.* **87**, 2890 (2000).
- [54] S.S. Li and W.R. Thurber: The dopant density and temperature dependence of electron mobility and resistivity in n-type silicon. *Solid-State Electron.* **20**, 609 (1977).
- [55] G. Ottaviani, L. Reggiani, C. Canali, F. Nava and A. Alberigi-Quaranta: Hole drift velocity in silicon. *Phys. Rev. B* **12**, 3318 (1975).
- [56] D.P. Joshi and R.S. Srivastava: Mobility and carrier concentration in polycrystalline silicon. *Solar Cells* **12**, 337 (1984).
- [57] J.Y.W. Seto: The electrical properties of polycrystalline silicon films. *J. Appl. Phys.* **46**, 5247 (1975).
- [58] A.R. Moore: Electron and hole drift mobility in amorphous silicon. *Appl. Phys. Lett.* **31**, 762 (1977).
- [59] T. He, M. Stolte and F. Würthner: Air-stable n-channel organic single crystal field-effect transistors based on microribbons of core-chlorinated naphthalene diimide. *Adv. Mater.* **25**, 6951 (2013).
- [60] Y. Yuan, G. Giri, A.L. Ayzner, A.P. Zoombelt, S.C.B. Mannsfeld, J. Chen, D. Nordlund, M.F. Toney, J. Huang and Z. Bao: Ultra-high mobility transparent organic thin film transistors grown by an off-centre spin-coating method. *Nat. Commun.* **5**, 1 (2014).
- [61] H.P. Latscha, U. Kazmaier and H.A. Klein: *Organische Chemie*. Springer (2008).
- [62] I. Fleming: *Molecular Orbitals and Organic Chemical Reactions*. John Wiley & Sons (2010).
- [63] S. Fratini, M. Nikolka, A. Salleo, G. Schweicher and H. Sirringhaus: Charge transport in high-mobility conjugated polymers and molecular semiconductors. *Nat. Mater.* **19**, 491 (2020).
- [64] R. Gross and A. Marx: *Festkörperphysik*. Oldenbourg Wissenschaftsverlag (2012).
- [65] A. Köhler and H. Bässler: *Electronic Processes in Organic Semiconductors*. Wiley-VCH (2015).
- [66] H. Sirringhaus, T. Sakanoue and J.F. Chang: Charge-transport physics of high-mobility molecular semiconductors. *Phys. Status Solidi B* **249**, 1655 (2012).

- [67] P. Drude: Zur Elektronentheorie der Metalle. *Ann. Phys.* **306**, 566 (1900).
- [68] N.W. Ashcroft and N.D. Mermin: *Solid State Physics*. Harcourt, Inc (1976).
- [69] M. Dressel and M. Scheffler: Verifying the Drude response. *Ann. Phys.* **518**, 535 (2006).
- [70] S.A. Maier: *Plasmonics: Fundamentals and Applications*. Springer US (2007).
- [71] N.V. Smith: Classical generalization of the Drude formula for the optical conductivity. *Phys. Rev. B* **64**, 155106 (2001).
- [72] H. Yada, H. Sekine, T. Miyamoto, T. Terashige, R. Uchida, T. Otaki, F. Maruike, N. Kida, T. Uemura, S. Watanabe, T. Okamoto, J. Takeya and H. Okamoto: Evaluating intrinsic mobility from transient terahertz conductivity spectra of microcrystal samples of organic molecular semiconductors. *Appl. Phys. Lett.* **115**, 143301 (2019).
- [73] K. Ohta, S. Tokonami, K. Takahashi, Y. Tamura, H. Yamada and K. Tominaga: Probing Charge Carrier Dynamics in Porphyrin-Based Organic Semiconductor Thin Films by Time-Resolved THz Spectroscopy. *J. Phys. Chem. B* **121**, 10157 (2017).
- [74] M.J. Sher, J.A. Bartelt, T.M. Burke, A. Salleo, M.D. McGehee and A.M. Lindenberg: Time- and Temperature-Independent Local Carrier Mobility and Effects of Regioregularity in Polymer-Fullerene Organic Semiconductors. *Adv. Electron. Mater.* **2**, 1500351 (2016).
- [75] N.F. Mott and M. Kaveh: Metal-insulator transitions in non-crystalline systems. *Adv. Phys.* **34**, 329 (1985).
- [76] K. Lee, A.J. Heeger and Y. Cao: Reflectance of polyaniline protonated with camphor sulfonic acid: Disordered metal on the metal-insulator boundary. *Phys. Rev. B* **48**, 14884 (1993).
- [77] M. Yamashita, C. Otani, M. Shimizu and H. Okuzaki: Effect of solvent on carrier transport in poly(3,4-ethylenedioxythiophene)/poly(4-styrenesulfonate) studied by terahertz and infrared-ultraviolet spectroscopy. *Appl. Phys. Lett.* **99**, (2011).
- [78] S. Fratini, S. Ciuchi and D. Mayou: Phenomenological model for charge dynamics and optical response of disordered systems: Application to organic semiconductors. *Phys. Rev. B* **89**, 235201 (2014).
- [79] S. Fratini, D. Mayou and S. Ciuchi: The Transient Localization Scenario for Charge Transport in Crystalline Organic Materials. *Adv. Funct. Mater.* **26**, 2292 (2016).
- [80] W. Nolting: *Grundkurs Theoretische Physik 3*. Springer (2013).

- [81] H.J. Butt, K. Graf and M. Kappl: *Physics and Chemistry of Interfaces*. Wiley-VCH (2003).
- [82] S.M. Sze and K.K. Ng: *Physics of Semiconductor Devices*. John Wiley & Sons (2006).
- [83] K. Seeger: *Semiconductor Physics*. Springer (2002).
- [84] J.S. Blakemore: Approximations for Fermi-Dirac integrals, especially the function  $F_{12}(\eta)$  used to describe electron density in a semiconductor. *Solid-State Electron.* **25**, 1067 (1982).
- [85] P. Van Halen and D.L. Pulfrey: Accurate, short series approximations to Fermi-Dirac integrals of order  $-1/2$ ,  $1/2$ ,  $1$ ,  $3/2$ ,  $2$ ,  $5/2$ ,  $3$ , and  $7/2$ . *J. Appl. Phys.* **57**, 5271 (1985).
- [86] W. Hackbusch: *Iterative Solution of Large Sparse Systems of Equations*. Springer (2016).
- [87] P. Deuffhard and A. Hohmann: *Numerische Mathematik 1*. De Gruyter (2018).
- [88] D. Sailer, A. Bornschlegl and R. Kersting: Screening within accumulation layers of molecular semiconductors. *Appl. Phys. Lett.* **117**, 083301 (2020).
- [89] D.M. Mattox: *Handbook of Physical Vapor Deposition (PVD) Processing*. Noyes Publications (1998).
- [90] M.A. Herman, W. Richter and H. Sitter: *Epitaxy*. Springer (2004).
- [91] A.C. Jones and M.L. Hitchman: *Chemical Vapour Deposition: Precursors, Processes and Applications*. The Royal Society of Chemistry (2008).
- [92] J. Jakabovič, J. Kováč, M. Weis, D. Haško, R. Srnánek, P. Valent and R. Resel: Preparation and properties of thin parylene layers as the gate dielectrics for organic field effect transistors. *Microelectron. J.* **40**, 595 (2009).
- [93] T. Marszalek, M. Gazicki-Lipman and J. Ulanski: Parylene C as a versatile dielectric material for organic field-effect transistors. *Beilstein J. Nanotechnol.* **8**, 1532 (2017).
- [94] A.C. Jones and P. O'Brien: *CVD of Compound Semiconductors*. Wiley (1997).
- [95] B.H. Lee and K. Yong: Diffusion barrier properties of metalorganic chemical vapor deposition -WNx compared with other barrier materials. *Journal of Vacuum Science & Technology B: Microelectronics and Nanometer Structures Processing, Measurement, and Phenomena* **22**, 2375 (2004).

- [96] K.S. Lee, T.M. Lu and X.C. Zhang: The measurement of the dielectric and optical properties of nano thin films by THz differential time-domain spectroscopy. *Microelectronics Journal* **34**, 63 (2003).
- [97] C. Pelvillain, P. Cussac, S. Diahham, Z. Valdez-Nava, M.L. Locatelli and T. Lebey: Dielectric and thermal properties of parylene N and D films for power electronic surface insulation. In *2015 IEEE 11th International Conference on the Properties and Applications of Dielectric Materials (ICPADM)*. IEEE, Sydney, NSW, Australia (2015).
- [98] V. Podzorov, V.M. Pudalov and M.E. Gershenson: Field-effect transistors on rubrene single crystals with parylene gate insulator. *Applied Physics Letters* **82**, 1739 (2003).
- [99] W.F. Gorham: A new, General Synthetic Method for the Preparation of Linear Poly-p-xylylenes. *Journal of Polymer Science* **4**, 3027 (1966).
- [100] D.B. Hall, P. Underhill and J.M. Torkelson: Spin Coating of Thin and Ultrathin Polymer Films. *Polymer Engineering and Science* **38**, 2039 (1998).
- [101] R.H. Chen and C.M. Cheng: Spin coating properties of SU-8 thick-layer photoresist. In *Advances in Resist Technology and Processing XVIII*, edited by F. M. Houlihan. International Society for Optics and Photonics, SPIE (2001).
- [102] Y. Wang, T. Hasegawa, H. Matsumoto, T. Mori and T. Michinobu: High-Performance n-Channel Organic Transistors Using High-Molecular-Weight Electron-Deficient Copolymers and Amine-Tailed Self-Assembled Monolayers. *Adv. Mater.* **30**, 1707164 (2018).
- [103] L. Sowjanya Pali, P. Ganesan and A. Garg: Inverted P3HT:PCBM organic solar cells on low carbon steel substrates. *Sol. Energy* **133**, 339 (2016).
- [104] M.D. Tyona: A theoretical study on spin coating technique. *Adv. Mater. Res.* **2**, 195 (2013).
- [105] B. Voigtländer: *Atomic Force Microscopy*. Springer (2019).
- [106] S.W. Smith: *The Scientist & Engineer's Guide to Digital Signal Processing*. California Technical Publishing (1998).
- [107] M. Pelliccione and T.M. Lu: *Evolution of Thin Film Morphology*. Springer (2008).
- [108] P. Klapetek, D. Nečas and C. Anderson. *Gwyddion user guide*. <http://gwyddion.net/download/user-guide/gwyddion-user-guide-en.pdf>. Accessed: 2023-04-01.
- [109] W. Demtröder: *Experimentalphysik 2*. Springer (2013).

- [110] T. Uemura, C. Rolin, T.H. Ke, P. Fesenko, J. Genoe, P. Heremans and J. Takeya: On the Extraction of Charge Carrier Mobility in High-Mobility Organic Transistors. *Adv. Mater.* **28**, 151 (2016).
- [111] M. Waldrip, O.D. Jurchescu, D.J. Gundlach and E.G. Bittle: Contact Resistance in Organic Field-Effect Transistors: Conquering the Barrier. *Adv. Funct. Mater.* **30**, 1904576 (2020).
- [112] T. Meier, H. Bässler and A. Köhler: The Impact of Grain Boundaries on Charge Transport in Polycrystalline Organic Field-Effect Transistors. *Adv. Opt. Mater.* **9**, 2100115 (2021).
- [113] A. Dodabalapur, L. Torsi and H.E. Katz: Organic Transistors: Two-Dimensional Transport and Improved Electrical Characteristics. *Science* **268**, 270 (1995).
- [114] J. Veres, S.D. Ogier, S.W. Leeming, D.C. Cupertino and S.M. Khaffaf: Low-k Insulators as the Choice of Dielectrics in Organic Field-Effect Transistors. *Adv. Funct. Mater.* **13**, 199 (2003).
- [115] A.F. Stassen, R.W.I. de Boer, N.N. Iosad and A.F. Morpurgo: Influence of the gate dielectric on the mobility of rubrene single-crystal field-effect transistors. *Appl. Phys. Lett.* **85**, 3899 (2004).
- [116] J. Veres, S. Ogier, G. Lloyd and D. de Leeuw: Gate Insulators in Organic Field-Effect Transistors. *Chem. Mater.* **16**, 4543 (2004).
- [117] S. Steudel, S. De Vusser, S. De Jonge, D. Janssen, S. Verlaak, J. Genoe and P. Heremans: Influence of the dielectric roughness on the performance of pentacene transistors. *Appl. Phys. Lett.* **85**, 4400 (2004).
- [118] P.A. Bobbert, A. Sharma, S.G.J. Mathijssen, M. Kemerink and D.M. de Leeuw: Operational Stability of Organic Field-Effect Transistors. *Adv. Mater.* **24**, 1146 (2012).
- [119] H.L. Gomes, P. Stallinga, M. Cölle, D.M. de Leeuw and F. Biscarini: Electrical instabilities in organic semiconductors caused by trapped supercooled water. *Appl. Phys. Lett.* **88**, (2006).
- [120] W.L. Kalb, T. Mathis, S. Haas, A.F. Stassen and B. Batlogg: Organic small molecule field-effect transistors with Cytos™ gate dielectric: Eliminating gate bias stress effects. *Appl. Phys. Lett.* **90**, (2007).
- [121] S.G.J. Mathijssen, M. Cölle, H. Gomes, E.C.P. Smits, B. de Boer, I. McCulloch, P.A. Bobbert and D.M. de Leeuw: Dynamics of Threshold Voltage Shifts in Organic and Amorphous Silicon Field-Effect Transistors. *Adv. Mater.* **19**, 2785 (2007).

- [122] P.P. Cielecki, T. Leißner, M. Ahmadpour, M. Madsen, H.G. Rubahn, J. Fiutowski and J. Kjelstrup-Hansen: Photo-induced and electrical degradation of organic field-effect transistors. *Org. Electron.* **82**, 105717 (2020).
- [123] Y. Chen, W. Deng, X. Zhang, M. Wang and J. Jie: Ambient instability of organic field-effect transistors and their improvement strategies. *J. Phys. D: Appl. Phys.* **55**, 053001 (2021).
- [124] C. Liu, Y. Xu and Y.Y. Noh: Contact engineering in organic field-effect transistors. *Mater. Today* **18**, 79 (2015).
- [125] R. Häusermann and B. Batlogg: Gate bias stress in pentacene field-effect-transistors: Charge trapping in the dielectric or semiconductor. *Appl. Phys. Lett.* **99**, 083303 (2011).
- [126] S.G.J. Mathijssen, M.J. Spijkman, A.M. Andringa, P.A. van Hal, I. McCulloch, M. Kemmerink, R.A.J. Janssen and D.M. de Leeuw: Revealing Buried Interfaces to Understand the Origins of Threshold Voltage Shifts in Organic Field-Effect Transistors. *Adv. Mater.* **22**, 5105 (2010).
- [127] K. Suemori, S. Uemura, M. Yoshida, S. Hoshino, N. Takada, T. Kodzasa and T. Kamata: Threshold voltage stability of organic field-effect transistors for various chemical species in the insulator surface. *Appl. Phys. Lett.* **91**, 192112 (2007).
- [128] S. Hunklinger: *Festkörperphysik*. Oldenbourg (2009).
- [129] Y. Xu, Y. Li, S. Li, F. Balestra, G. Ghibaudo, W. Li, Y.F. Lin, H. Sun, J. Wan, X. Wang, Y. Guo, Y. Shi and Y.Y. Noh: Precise Extraction of Charge Carrier Mobility for Organic Transistors. *Adv. Funct. Mater.* **30**, 1904508 (2019).
- [130] W. Demtröder: *Experimentalphysik 1*. Springer Spektrum (2015).
- [131] J.C. Slater: Atomic Radii in Crystals. *The Journal of Chemical Physics* **41**, 3199 (1964).
- [132] G.S.U.D. of Physics and Astronomy. *Spectral Colors*. <http://hyperphysics.phy-astr.gsu.edu/hbase/vision/specol.html>. Accessed: 2023-04-09.

# Acknowledgment

First and foremost, I would like to thank my supervisor Prof. Dr. Roland Kersting for his guidance and his belief, that things will work out. I could not have undertaken this journey without his feedback and the valuable discussions we had.

Secondly, a big thanks to Priv-Doz. Dr. Bert Nickel and his willingness to be the second assessor of this work.

I am grateful to Prof. Dr. Jochen Feldmann and his group for letting me be a part of the Photonics and Optoelectronics chair and for using his facilities.

Additionally, I would like to say thanks to Yves Geerts, Guillaume Schweicher and Felix Devaux for the provision of the molecular semiconductor DBTTT and the fruitful conversations in the course of this work.

Without the help of Stefan Niedermaier, Thalee Barghouti, Philipp Altpeter, Christian Obermayer, Jürgen Aust and Thomas Großhauser, this work would not have been possible. I know it is not always easy to find the time to help, but you always found it.

Furthermore, a big thanks to Christian Eckel and Thomas Weitz from the Georg-August-university of Göttingen for the successful cooperation with polymeric semiconductors, even though the results came to late to be part of this thesis.

Thanks should also go to my former masters and bachelors students Meriem Bouraoui, Paul Tkacz, Moritz Markl, Felix von Falkenhausen and Korbinian Lechermann. Some things would have definitely taken more time without you.

I would be remiss in not mentioning my dear former student colleagues especially Fabian Merbeler and Matthias Golibrzuch. Still, you are one of the first persons I turn to when I question my own path.

Without the support of my family, this work would probably have driven me closer to insanity. Thank you for providing me everything I needed to be capable of such achievements.

My last words belong to Johanna Zartner, my best friend and my love. If times get tough you are my shelter in the rain. Thank you.